Abstract

SLOMSKI, MICHAEL JOSEPH. Thermal Conductivity of Group-III Nitrides and Oxides. (Under the direction of Dr. Tania Paskova and Dr. Albena Ivanisevic).

Group-III nitrides have emerged as one of the most promising wide-bandgap semiconductors for devices used in power and optoelectronic applications. The knowledge of the thermal conductivity in group-III nitrides is important for both managing self-heating in high power applications and for proper operation in high temperature environments. Despite the popularity of the nitrides, the current knowledge of the thermal conductivity is still incomplete due to the complex dependence on the material properties stemming from growth. This work focuses on how properties resulting from growth such as material quality, intentional/unintentional impurity concentration, and alloying elements affect the thermal conductivity in group-III nitrides and oxides.

The thermal conductivity of n-type GaN was measured using the 3ω method and compared to calculations from a modified Callaway model for understanding the contribution of the different scattering mechanisms. Samples were grown by hydride phase vapor epitaxy with Si concentrations varying from 1.6×10^{16} – 7×10^{18} cm^{-3} for the purpose of modulating the electrical conductivity. At room temperature, the thermal conductivity was found to decrease with increasing Si concentration from the maximum value of 245 W/mK for the undoped sample, which was attributed to increased phonon-impurity and phonon-free electron scattering. In the range of 295-400K, the thermal conductivity was found to decrease with increasing temperature. However, increasing Si concentration was found to decrease this temperature dependence and it was suggested to be due to an increase in the free electron contribution to thermal conductivity.

Semi-insulating material was then grown and the impact of increasing Fe concentration on the thermal conductivity was characterized. The thermal conductivity was found to decrease with increased Fe dopant concentration similar to Si, however the effect was found to be less pronounced due to the lack of a contribution from phonon-free electron scattering. The reduction in thermal conductivity at elevated temperatures was described by a simple power law, which decreased from a power of -0.94 for the undoped sample to -0.55 for the sample with the highest Fe concentration.

Next, the effect of alloying elements on thermal conductivity was studied by measuring AlGaN films on GaN substrates with varying alloy compositions and film thicknesses using the differential 3ω method. Small additions of alloying elements were found to cause a pronounced decrease in the thermal conductivity, which was explained by scattering caused by the large mass difference between the Al and Ga atoms. The effect increasing AlGaN film thickness, and therefore reducing the defect density, on thermal conductivity was then studied and was found to logarithmically increase the thermal conductivity up to the predicted bulk value, which was approached at thicknesses of 25μm.

Finally, gallium oxide (β-Ga_2O_3) was examined by aiming to determine the thermal conductivity of undoped, n-type (Sn doped), and semi-insulating (Fe doped) bulk crystals. A novel approach was employed to extract the anisotropic thermal conductivity with the 3ω slope method. The thermal conductivity was found to be highly anisotropic, with the maximum of 29 W/mK in the [010] direction being nearly double that in other crystalline directions. The addition of Sn and Fe dopants showed almost reduction in thermal conductivity from the undoped sample, however dopants were found on average to reduce the temperature dependence of thermal conductivity.

© Copyright 2017 Michael Joseph Slomski

All Rights Reserved

Thermal Conductivity of Group-III Nitrides and Oxides

by
Michael Joseph Slomski

A dissertation submitted to the Graduate Faculty of
North Carolina State University
in partial fulfillment of the
requirements for the degree of
Doctor of Philosophy

Material Science and Engineering

Raleigh, North Carolina

2017

APPROVED BY:

Dr. Tania Paskova Co-Chair of Advisory Committee	Dr. John F. Muth
Dr. Albena Ivanisevic Co-Chair of Advisory Committee	Dr. Jagdish Narayan

Biography

Michael Joseph Slomski was born in Erie, Pennsylvania on October 23, 1989, where he lived for less than a month. Due to a job transfer, parents Brenda and Roger moved Mike to Apex, North Carolina where he would spend his entire childhood up until the graduation of high school. Growing up in the Raleigh area, Mike was very familiar with North Carolina State University and had made plans at a young age to attend the Engineering School. In 2008, Mike started his Bachelors in the Engineering School and quickly decided to complete his degree in Materials Science and Engineering, which he received in 2012. With a desire to continue his education in the more specialized focus of wide bandgap semiconductors, Mike decided to work towards a PhD in the same department under Dr. Tania Paskova. Despite his love for his hometown of Raleigh, Mike has plans to move to Portland, Oregon upon graduation to continue his career as a lithography process engineer.

Acknowledgements

I would like to thank Dr. Tania Paskova, for not only her guidance and mentoring related to the work in this thesis, but also for her personal support and encouragement when I truly needed it. I would also like to thank Dr. John F. Muth, Dr. Albena Ivanisevic, and Dr. Jagdish "Jay" Narayan for their time and effort as mentors and members of my committee. I wish to thank all of those who have collaborated with me during my work, including Dr. Plamen Paskov and Nicholas Blumenschein for their shared knowledge and effort on our publications. I am thankful to all companies that provided samples allowing me to complete my graduate studies: Dr. Jacob Leach and all of Kyma Technologies Inc., Unipress, and Nitride Solutions. Thanks to the MSE staff, especially Edna Deas for keeping everyone on track, and Roger Russell and Toby Tung for their opportunities and support. A special thanks to Joe Matthews for his support, knowledge, and comradery in all things related to the cleanroom.

Most importantly, thank you to my family and Dr. Nora Berg for their continued support and motivation no matter the situation, you are the best and I love you!

Table of Contents

List of Tables vii
List of Figures viii
1. Nitride applications and templates vs. bulk substrates 1
1.1. Nitride applications 1
1.2. Nitride bulk substrates 2
1.3. Nitride growth methods 5
1.3.1. Sublimation growth 6
1.3.2. Hydride phase vapor epitaxy 14
1.3.3. Ammonothermal growth 23
1.3.4. Solution growth at high pressure, high temperature 24
1.3.5. Mixed growth methods 25
1.4. Properties of nitride substrates 27
1.4.1. Defect density 27
1.4.2. Doping and electrical conductivity 29
1.5. Conclusions 32
References 33
2. Thermal conductivity of nitrides 47
2.1. Introduction to thermal conductivity in nitrides 47
2.2. Origin of the thermal conductivity of materials 49
2.3. Overview of thermal conductivity characterization techniques 50
2.3.1. Steady-state techniques 51
2.3.2. Dynamic techniques 52
2.4. The 3ω method 57
2.4.1. Equation for a line source heater on an infinite half-solid 58
2.4.2. Physics of the 3ω method 60
2.4.3. The slope 3ω method 63
2.4.4. The differential 3ω method 68
2.4.5. Sample and device processing for the 3ω method 75
2.4.6. Experimental details for the 3ω method 80
2.5. Thermal conduction theory in nitrides 85

2.5.1. Introduction ... 85
2.5.2. Modified Callaway model ... 85
2.5.3. Phonon scattering processes ... 87
2.5.4. Summary ... 94
References ... 95
3. Thermal conductivity of n-type GaN ... 98
3.1. Introduction ... 98
3.2. Experimental details ... 102
3.2.1. Sample growth and characterization ... 102
3.2.2. 3ω measurement details ... 104
3.3. Results and discussion ... 105
3.3.1. Undoped bulk GaN ... 105
3.3.2. Bulk AlN ... 105
3.3.3. Intentionally doped n-type GaN ... 107
3.4. Conclusions ... 121
References ... 122
4. Thermal conductivity of semi-insulating GaN ... 127
4.1. Introduction ... 127
4.2. Experimental details ... 130
4.2.1. Sample growth ... 130
4.2.2. Sample characterization ... 130
4.2.3. 3ω measurement details ... 132
4.3. Results and discussion ... 134
4.4. Conclusions ... 139
References ... 139
5. Thermal conductivity of ternary III-nitride alloys ... 142
5.1. Introduction ... 142
5.2. Experimental methods ... 145
5.2.1. Sample characteristics ... 145
5.2.2. Crystalline quality ... 146
5.2.3. 3ω measurement details ... 147
5.3. Results and discussion ... 150

5.4. Conclusions 156
References 157
6. Thermal conductivity of other wide bandgap semiconductors: β-Ga_2O_3 159
6.1. Introduction 159
6.2. Experimental details 162
6.2.1. Sample growth and characterization 162
6.2.2. 3ω measurement details 163
6.2.3. Data analysis 167
6.3. Results and discussion 170
6.3.1. Room temperature thermal conductivity 170
6.3.2. Thermal conductivity at elevated temperatures 171
6.3.3. Effect of doping 176
6.4. Conclusions 178
References 179

List of Tables

Table 3.1 *Sample properties of n-type HVPE GaN doped with Si* 104

Table 3.2 *Material parameters for thermal conductivity calculations* 110

Table 5.1 *Sample properties of AlGaN films* 145

Table 6.1 *Orientation of heater/thermometer device and respective heat flow directions for β-Ga_2O_3 samples* 163

Table 6.2 *Room temperature thermal conductivity for different orientations and dopants in β-Ga_2O_3* 170

Table 6.3 *Temperature dependence of thermal conductivity for different orientations and dopants for β-Ga_2O_3* 174

List of Figures

Figure 1.1 *Types of AlN sublimation reactors with various heating systems* 7

Figure 1.2 *Types of HVPE reactors used for growth of nitrides*... 17

Figure 1.3 *Dislocation density as a function of the GaN layer thickness* 28

Figure 1.4 *Temperature dependence of free electron concentration and mobility*............. 31

Figure 2.1 *Schematic of a line heater on the cross section of an infinite half solid* 58

Figure 2.2 *Illustration of the frequency dependence of penetration depth* 66

Figure 2.3 *Film on a substrate for 1D heat flow case in the differential method* 69

Figure 2.4 *Mask used for patterning of heater/thermometers for the 3ω method* 79

Figure 2.5 *Diagram of experimental setup and circuit used in the 3ω method*.................. 81

Figure 2.5 *Resistance versus temperature relation used to extract* α_{TCR} 83

Figure 3.1 *Reported thermal conductivity of GaN versus year of publication* 100

Figure 3.2 *Temperature dependence of thermal conductivity of undoped III-nitrides* 106

Figure 3.3 *Thermal conductivity vs temperature of Si doped n-type GaN*........................ 108

Figure 3.4 *Thermal conductivity of GaN with low and high temperature forms for N-scattering rate* 113

Figure 3.5 *Comparison of the different models for the thermal conductivity for Si doped GaN* 115

Figure 3.6 *Thermal conductivity of bulk GaN as a function of Si concentration with and without FE-scattering* 117

Figure 3.7 *Temperature dependence of the thermal conductivity for all measured Si doped GaN samples* 119

Figure 3.8 *Slope of the temperature dependence of thermal conductivity as a function of Si concentration* ... 120

Figure 4.1 *SIMS profile for impurity concentrations of Fe doped GaN samples* ... 131

Figure 4.2 *Fe concentration vs. Fe flow rates in HVPE growth.* ... 132

Figure 4.3 *$V_{3\omega}$ vs. $\omega/2\pi$ used to determine thermal conductivity of Fe doped GaN* ... 134

Figure 4.4 *Room temperature thermal conductivity vs. Fe concentration.* ... 135

Figure 4.5 *Temperature dependence of thermal conductivity for all Fe doping concentrations with power law fit.* ... 137

Figure 5.1 *Thermal conductivity vs. Al fraction in AlGaN films.* ... 151

Figure 5.2 *Thermal conductivity vs. AlGaN film thickness* ... 154

Figure 6.1 *$V_{3\omega}$ vs. $\omega/2\pi$ (semi-log) for an undoped β-Ga_2O_3.* ... 164

Figure 6.2 *Cross-section view of heater/sensor on β-Ga_2O_3 unit cell* ... 166

Figure 6.3 *Temperature dependence of the thermal conductivity for different orientations β-Ga_2O_3* ... 172

Figure 6.4 *Effect of Sn and Fe doping on the thermal conductivity temperature dependence of β-Ga_2O_3.* ... 177

1. Nitride applications and templates vs. bulk substrates

1.1. Nitride applications

Gallium nitride (GaN) and its close chemical counterparts: aluminum nitride (AlN), indium nitride (InN), and their ternary alloys Al(Ga,In)N forms III-V nitride-based semiconductor family (often referred to as nitrides). The most established applications of III-nitride semiconductors are optoelectronics and electronics, but applications such as spintronics, photovoltaics and sensors are recently under extensive research as well. Detailed summary of their applications and market analysis can be found in various publications[1-3].

From application point of view, optoelectronics is the largest market due to the fact that devices emitting from ultraviolet to red can be fabricated by using the nitride semiconductors. They have a direct band gap and the band gap energy of the Al(Ga,In)N varies in wide range from 6.2 and 0.7eV depending on their alloy composition[4]. The interest in nitrides for electronic application is also very strong, motivated by their unique properties. In particular, GaN is one of the few materials with both a high breakdown voltage and a high saturation velocity[5]. The nitrides are well suited for high temperature applications because of their ide bandgaps and low intrinsic carrier concentrations. The electron mobility in GaN is quite high considering the magnitude of the bandgap and is even higher in selectively doped AlGaN/GaN heterostructures where 2-dimensional electron gases (2DEG) may form, producing high sheet carrier densities. The strong piezoelectric and polarization effects presented in the AlGaN/GaN structures enhance these densities. These properties make the nitrides the best semiconductor system for high-frequency electronic applications. Finally,

GaN possesses a very high breakdown field, allowing the devices to support large voltages for high power operation[6].

1.2. Nitride bulk substrates

Despite this incredible potential of the nitride materials, device performance and the fundamental understanding of the properties is still limited by the material quality[7]. Unfortunately, due to high melting temperatures and very high dissociation pressures, bulk nitrides cannot be grown by using conventional methods used for GaAs or Si, such as the Czochraslski or Bridgman techniques. Bulk GaN and AlN crystals have only recently become commercially available and mostly with limited size. Even so, the price for these materials is still beyond the cost-sensitive customers[8,9].

Most applications of nitrides have relied on heteroepitaxy. A wide variety of materials have been studied for substrates for nitride epitaxy including insulating metal oxides, metals, metal nitrides, and other semiconductors. However, despite the significant success in GaN heteroepitaxy on many different substrates, the mismatch in thermal expansion coefficients and lattice parameters leads to some degradation of the film quality. A thorough discussion of substrates for GaN heteroepitaxy is given in an earlier review by Liu and Edgar.[7] The growth process and device fabrication technology have been described in many reviews such as those by Ambacher,[10] Gibart et al.,[11] Sheu and Chi,[12] Pearton et al.,[13,14] Morkoç et al.,[15,16] Monemar,[17] J. W. Orton and Foxon,[18] Munoz et al.,[19] Steigerwald et al.,[20] Bickermann and Paskova.[21]

The first GaN-based light emitting diodes (LED) were fabricated on sapphire with typical dislocation density higher than 10^9 cm^{-2}. Before that, good luminescence efficiency,

regardless of the semiconductor, was thought to require very low dislocation densities, less than 10^6 (cm^{-2}).[22] Researchers were surprised to measure excellent luminescence efficiency from GaN based LEDs despite dislocation densities four orders of magnitude higher. As devices other than LEDs have been developed using GaN, it has become apparent that the conventional wisdom on the requirements for device fabrication and epitaxial growth still has merit. It became clear, in agreement with the prior knowledge, that high dislocation densities are detrimental to the performance of devices with more sophisticated structures such as laser diodes (LDs), or for devices requiring large areas or operating at greater power densities.[23]

In the case of LDs, it is very well known that the lifetime is largely increased when LDs are fabricated on the lower dislocation region realized by epitaxial lateral overgrowth (ELO) technique, which can produce GaN with dislocation density down to mid-10^6 cm^{-2}. Dislocations can cause deterioration in the operation of quantum-well based LDs mainly by three mechanisms:[24] (i) serving as nonradiative recombination centers for electrons and holes leading to heat generation instead of optical emission; (ii) introducing fast diffusion along the dislocation lines, smearing out quantum wells and p-n junctions; and (iii) disturbing the epitaxial growth, so that atomically flat structures cannot be obtained. The power, lifetime, and reliability of LDs fabricated on bulk GaN with even lower dislocation were improved greatly. Thus, bulk GaN substrates with dislocation density less than 10^5 cm^{-2}, preferable less than 10^3 cm^{-2} are highly desirable for reliable high power LDs.

For short wavelength violet LEDs, dislocations can also noticeably affect performance. This influence may result from longer diffusion length for low In-composition of InGaN alloy. It was predicted that when the diffusion length is longer than 500 nm, the

value similar to those for other conventional LED materials, dislocation densities must be lower than 10^6 cm^{-2}. On the contrast, the diffusion length is as low as 50 nm in blue InGaN/GaN LEDs, which can allow the dislocation densities up to 10^9 cm^{-2} without acting as recombination center.[25] On the other hand, white LEDs based on UV LEDs plus RGB phosphors will be competing against blue LEDs with yellow phosphors in a variety of applications with its advantages. In this case, bulk nitride substrates with low dislocation densities may help to realize high-efficiency white LEDs. It was confirmed that threading dislocations could cause leakage current[26] and aging of high power LEDs.[27] As Tsao et al.[28] pointed out, the small-area chip ($0.25mm^2$) scenario for solid-state lighting commercialization may require 10^6 cm^{-2} or less dislocation density. Hence, development of alternative substrate technology could potentially open a huge market for bulk nitrides.

In case of electronic devices, dislocations also have a deterioration effect on the device performance. It was revealed that screw dislocation lines can act as a channel for the reverse-bias leakage current in Schottky diodes[29,30] by promoting the metal diffusion along the lines.[31] Yamada et al.[32] found that the reverse bias leakage current of p-n junction devices was reduced by more than two orders of magnitude by decreasing the threading dislocation density down to 10^6 cm^{-2} when employing epitaxial lateral overgrowth (ELO) technique in comparison with growing directly on a sapphire substrate. McCarthy et al.[33] compared the performance of GaN heterojunction bipolar transistors (HBTs) fabricated on MOCVD GaN templates and ELO materials. It was identified that the dislocations were the primary source of collector-emitter leakage and it was reduced by four orders of magnitude for devices on ELO materials. It is well known that the key for GaN HEMT with high performance is low

leakage in the buffer layer, which demands highly resistive epilayers with low defect density. Moreover, the traps associated with dislocations in the buffer layer also cause current collapse in AlGaN/GaN FETs.[16] Additionally, studies on device reliability over their lifetime indicate that the dislocations also result in aging degradation of the electronic devices.[34] In summary, the effect on both device performance, lifetime and reliability is significant, which could explain the demand for high-quality, low-defect-density GaN substrates.

Furthermore, it is important to underline that conductive bulk nitride substrates offer a few more advantages in addition to lower dislocation density: (i) conductive GaN substrates allow vertical device geometries, therefore higher current flow and higher yield for device fabrication; (ii) the same cleaving property between substrate and epilayers makes it easy for fabricating laser mirrors for resonance oscillation; (iii) higher thermal conductivity improves heat dissipation for high power devices; (iv) various crystallographic orientations, which allows device alignment with different polarities; Lastly, with respect to the device growth process, bulk nitride substrates eliminate the steps of low temperature nucleation layer growth, temperature ramping, and several micron buffer layer growth, therefore reduce material usage, increase throughput, and reduce cost.

1.3. Nitride growth methods

This section will focus on the various growth methods that have been intensively studied in the last two decades, including hydride phase vapor epitaxy (HVPE), ammonothermal growth, high pressure solution growth (HPSG), and the combination of growth methods. Various techniques were used for bulk crystal growth, template growth, single substrate growth, boule growth, and seeded regrowth.

1.3.1. Sublimation growth

Sublimation is almost exclusively used for growth of AlN. This method is usually carried out in a furnace with a temperature gradient, which provides the driving force for the growth. There are two major types of furnaces: resistively heated furnaces and RF heated furnaces. In order to achieve considerable growth rates, the sublimation growth of AlN requires high temperature (>1800°C, and typically about 2200 ^{o}C). Such a high temperature along with the high reactivity of Al vapor could create severe problem for the stability of the furnace fixture, which could be degraded quickly or even melt. In order to reduce the temperature, various approaches were proposed by the research groups working on this topic, including different reactor configurations with various heating systems (a few examples shown in *Figure 1.1(a-d))*.

AlN sublimation, a kind of physical vapor transport growth, is a relatively simple process. Initially, kinetic studies, performed by Liu[35] and Noveski[36] demonstrated that the growth rate was limited by the mass transport in the gas phase at pressure >200 torr and temperature range of 1700 ~2400 ^{o}C. Reducing pressure was effective in increasing the growth rate since it increased not only the partial pressure of aluminum but also the diffusivity. Yet, the growth was limited by the stability of crucible under high aluminum partial pressure. Nevertheless, later studies revealed that the surface kinetics would take effect at low pressure.[37] At that time, the rate controlling step of growth was the availability of active nitrogen adatoms rather than that of aluminum at crystal surface due to the low sticking coefficient of N_2. Currently, most of the reported growth rates are still below 1 mm/hr, which is limited by the stability of crucible at high temperature and low N_2 pressure.

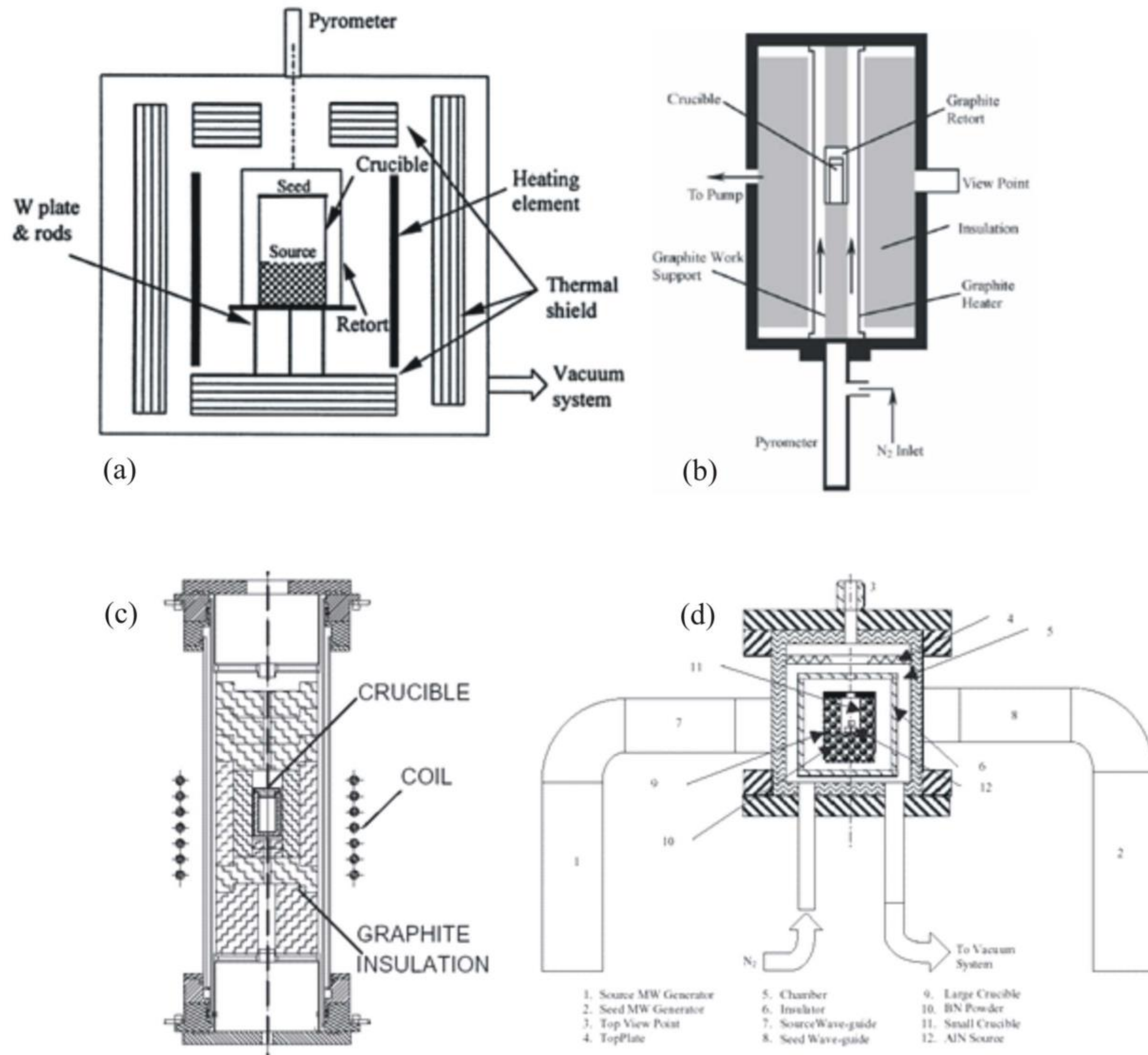

Figure 1.1 *AlN sublimation reactors with various heating systems: (a) resistively heating system using tungsten;*[35] *(b) resistively heating system using graphite;*[37] *(c) induction heating system;*[36] *(d) microwave heating system*[38]

AlN growth was usually conducted in a crucible inside a furnace. The selection of suitable crucible materials has been a major challenge at such high temperature. The properties and stabilities of different materials for crucibles or coating such as W, graphite, BN, SiC, TaC, TaN, NbC, Ta, Ta2C, Re, ZrO2, ZrC, ZrN, HfN, HfC, and so on, under

various sublimation conditions have been reviewed by Liu et al.,[38] Dalmau et al.,[39] Slack et al.,[40] Epelbaum et al.[41] The following major conclusions were drawn: (1) The crystal color, growth habit, and morphology were affected by the choice of crucible materials. The density of extended defects and their distribution in the crystals remained unaffected; (2) Pure W is a quite durable crucible material for AlN sublimation growth at medium temperatures. It also ensures high purity crystal growth. At temperatures above 2300 °C the W crucibles suffer from attack by aluminum vapor, which eventually leads to failure. Nevertheless, the free nucleation in W crucible has very high density and is difficult to control; (3) TaN, TaC and NbC may be the best choices considering the crucible lifetime, material compatibility, and crystal quality; however, the cost is high. In addition, the coated graphite components are not suitable as the coatings tend to spall off; (4) BN caused highly anisotropic growth rates along different crystallographic directions. The crystals produced are highly striated; (5) Other materials may offer inferior performance due to the reaction with aluminum or sublimation at the typical crystal growth temperatures; (6) The thermal expansion also needs to be considered for the case of crystal growth contacting the crucible walls. Materials with similar thermal expansion coefficient to that of AlN are preferred in order to reduce the stress during cooling down.

Other furnace fixtures along with the crucible and source themselves can cause profound contamination in AlN during growth. The unintentional impurity incorporation in bulk AlN crystals is an important issue, as impurities not only can change physical, optical (i.e. UV transparency), and electrical properties, but also can change the growth mechanism and initiate crystal defects. For example, Brenner et al.[42] revealed that boron substitutional

impurities can enhance binding and incorporation of growth species onto steps. In addition to forming crystal defects, impurities can also change the crystal morphology as a consequence of surfactant effects and changes in the Al-N thermodynamics.[43] Oxygen in AlN crystals are difficult to avoid since the commercial AlN sources can contain as high as 1.0 wt%. This oxygen contamination from the source material was found to be the most challenging problem because of oxygen-assisted transport of aluminum at relatively low temperature of 1700-1800 °C. The oxygen impurity can occur as a substitution impurity on nitrogen sites at concentrations up to $1x10^{21}$ cm^{-3}.[44] At even higher concentration, it produces eventually Al_2O_3 inclusions. The oxygen in the source is transported presumably as AlO and Al2O with AlON during heating-up stage.[45] A subsequent growth of dense AlN on such powder layer generated at heating-up stage was possible, but resulted in a very small grain size of 0.1-0.3 mm.[46] To improve the nucleation control, a temperature gradient reversal method was used, i.e. in the beginning of the process the source was kept at lower temperature and the oxygen concentration can be reduced to 10^{19} cm^{-3}.[46,47] Intensive studies of AlN properties revealed that the oxygen impurity has a significant effect on various material properties, such as thermal conductivity, luminescence, optical absorption, UV transparency, etc.[48-52]

The free-nucleation growth of AlN on graphite walls was reported by Tanaka et al.[53] to result in three morphologies at different temperatures: flat plates at 2100 °C; needles with hexagonal cross-section at 2000 °C; and needles with rectangular cross-sections at 1900 °C. The yellow color of crystals was attributed to blue light adsorption by the oxygen impurity. This growth habit of crystal shape dependence on temperature was also observed by Epelbaum et al.[54] and Singh et. al.[55]. Edgar et. al.[56-58] studied the self-nucleation on both W

and BN crucible in resistively heated furnace with W or graphite heating elements. The largest growth rate of 0.4 mm/hr was found in BN crucible, though it resulted in thin platelets. The self-seeding produces crystals of highest perfection, lowest stress, and lowest Si and C impurity content compared to seeded growth on SiC. The crystal quality, (as revealed by Raman scattering spectroscopy - full width at half maximum (FWHM) of the high-frequency peak (E1(LO)+A1(LO)) - and x-ray diffraction – FWHM of the 0002 reflection) was found higher in the freely nucleated crystals than that in material grown by seeded growth.[59] The crystals grown by Raghothamachar et. al.[60] also displayed high quality, with dislocation density of about 10^3 cm^{-2}. It is important to note that usually AlN single crystals grow in random crystallographic orientations and the crystallite size is on the order of mm. Different shapes of AlN single crystals, such as boules, platelets, prisms, needles, and whiskers, have been reported by different researchers. The large diameter (cm size) crystals by self-nucleation were unfortunately polycrystalline, though the growth rate was as high as 1 mm/hr.

In order to increase the crystal size and control the shape of free nucleation, the Crystal IS research team which continues the pioneering work of Slack et. al.,[61] utilized a cone-shaped crucible. Ideally, a single nucleus forms at the tip end of the crucible at high temperature such as about 2250 ^{o}C and evolves into large single crystal grain. The single grains became larger and began to dominate as the boule grows, while the surface area occupied by the polycrystalline region decreases. Typically, however, several nuclei form and compete with each other as the growth proceeds. The growth rate was reported as high as to 0.9 mm/hour,[62] with the largest size recently claimed to be two inches. A corresponding

step flow growth mechanism, which originated from the screw dislocation, was also proposed by the same research group.[63,64] Screw dislocations dominated and no edge dislocations were observed in these large single crystal grains, though the screw dislocation densities were below $5x10^4$ cm^{-2}. The characterization results indicated that the dislocation density was 800-1000 cm^{-2} and FWHM of the 0002 rocking curve was less than 10 arcsec.[65]

Using a substrate as a seed crystal is an attractive alternative since the crystal orientation, crystal polarity, and the initial nucleation can be better controlled. Moreover, the large diameter seed crystals up to the available size of SiC may greatly facilitate scaling to produce large crystals. Single crystalline 6H-SiC (0001) wafers were used due to the relatively small lattice mismatch to AlN (0.9%) and their high temperature stability. The growth of AlN on SiC was first reported by Balkas et al.[66] The results from TEM analyses revealed the absence of line and planar defects; Raman and x-ray diffraction studies also indicated excellent crystalline quality of the grown AlN crystal. However, the crystals contained small (~2x2 mm^2), individual hexagonal sub-grains and cracks upon cooling. Edgar et. al.[58, 67-71] conducted extensive research work on AlN seeded growth on SiC. Typically, the source temperature was above 1800 ^{o}C, the source-substrate temperature gradient was less than 5 ^{o}C/mm, and the ambient pressure varied in the range of 100 - 800 torr. Significant difficulties were encountered when 6H-SiC substrates were used as seed crystals for bulk AlN growth, such as: decomposition of 6H-SiC at high temperatures, isolated random nucleation of AlN and subsequent individual sub-grain growth, cracks in the AlN caused by stress from the mismatch of thermal expansion between AlN and SiC. Direct growth on as-received Si-face SiC resulted in formation of discontinuous hexagonal

subgrains of 1-mm size. Growth of AlN on carbon-polarity substrates was almost completely absent[58]. Such incomplete coalescence was caused by decomposition of the 6H-SiC in the presence of AlN, forming hillocks on the surface. Subsequently, the AlN tends to nucleate on these SiC hillocks. In some areas, sub-grain boundaries were formed as the AlN islands grew and merged together. In other regions, the AlN islands stoped growing laterally, and simply grow vertically (along the [0001] direction) leaving deep, irregular crevasses between AlN islands.[67] Using high temperature MOCVD, grown AlN effectively improved the wetting of SiC and resulted in 2D growth mode during sublimation.[68,69] The AlN epilayer promoted layer-by-layer growth forming a continuous single grain film, however, the crystal always suffered from cool-down cracking. For thick AlN films, the AlN was under biaxial compressive stress at the surface but tensile stress at the AlN/SiC interface. Large tensile stresses at the interface of the AlN/SiC heterostructure, up to 1 GPa, were detected by the frequency shift of the Raman E1(TO) mode. The frequency shift along with stress had an approximate linear distribution along the depth of sample. An AlN crystal thickness greater than 2mm was estimated as necessary to completely eliminate cracking. In order to solve the cracking problem, a deposition of pure AlN was proposed on a thick layer (0.1-0.5 mm) of $(AlN)_x(SiC)_{1-x}$ alloy film on SiC by sublimation from a mixture of AlN-SiC powders at 1800 ^{o}C.[70] The intermediate properties of an (AlN-SiC) alloy layer greatly reduced cracking in the final AlN crystal. In addition, the presence of silicon and carbon in the source material reduced or eliminated the decomposition of the SiC substrate during sublimation crystal growth, enabling longer duration crystal growth. By employing this technique, a high quality colorless AlN single crystals up to 1 cm in diameter were produced. Analysis by x-ray

diffraction indicated that the AlN single crystal was of comparable quality to the original 6H-SiC (0001) substrate.[71] For AlN single crystals seeded on 6H-SiC substrates, the FWHM of x-ray rocking curve for asymmetric peaks had a larger value than that of the symmetric peaks (i.e. the (0002) peak). Such disparity between the FWHM of the symmetric and asymmetric peaks is commonly observed for the group III nitrides and has been attributed to the presence of significantly more dislocations of edge type rather than screw type.[72,73]

The growth of AlN on AlN seed grown by self-nucleation was also attempted. Schlesser et al.[74] grew cm-size single crystals at 2100-2300 °C on AlN seeds grown by vaporization of Al in a nitrogen atmosphere. Seeded growth occurred preferentially in the c-direction. The FWHM of 0002 rocking curve was only 25 arcsec, indicating high quality of crystals grown by seeded homogrowth. Noveski et al.[47,75] developed a process for continuous growth on previously deposited materials. By using the inverted temperature gradient method, part of the grown materials were removed and the re-nucleation of AlN was suppressed on the previously grown materials, which were exposed to air during AlN source replenishment in order to maintain constant source-seed distance. Through a multiple regrowth run, cm size single crystal grains were demonstrated. The same research group continued extensive work using AlN for seeded growth in both c- and m-orientation.[76,77] However, the seed expansion to 2-inch diameter was extremely challenging due to process repeatability issues.

1.3.2. Hydride phase vapor epitaxy

Unlike sublimation, Hydride phase vapor epitaxy (HVPE) growth has been used for the growth of all three nitride compounds: AlN, GaN and InN, as well as for their ternary alloys.

1.3.2.1. HVPE growth of GaN

HVPE is an attractive technique for bulk GaN growth due to its ability to produce thick layers of high quality with high growth rates and relatively low cost. The thick layers produced by HVPE can be used as quasi-bulk substrates after delamination, or to obtain GaN boules which can be sliced into GaN substrates. Nearly all of the GaN substrates on today's market are fabricated by the HVPE technique, owing to its favorable processing conditions. Atmospheric pressure and relatively low processing temperature as compared to other techniques create a cost-effective growth method when paired with its high growth rate above 100µm/hour.[78] The HVPE technique is able to obtain these high growth rates due to its high surface migration rates for the halide species.

The HVPE technique has proven that it is capable of producing n-type, p-type, and semi-insulating material. It is not possible to achieve completely undoped material, as HVPE grown material always exhibits unintentional n-type doping due to background doping by silicon and oxygen introduced form the quartz within the reactor or process gases. Intentional n-type doping is usually achieved with silicon and oxygen, although doping with Ge and Sn has been accomplished. Si doping is usually performed by introducing a flow gas of Silane (SiH_4), disilane (Si_2H_6), or dichlorosilane (SiH_2Cl_2).[79]

HVPE growth optimizations have been reported in numerous publication, including several review papers.[78-81] For successful HVPE GaN growth, the following major conclusions could be summarized: (1) An inert ambient atmosphere is needed and is more effective for GaN growth than hydrogen atmosphere, the latter being widely used for other III-V systems as well. (2) In HVPE-GaN growth, NH_3 should be used as the source of the group V element rather than a nitrogen halide (NCl_3), which is highly explosive. Moreover, the thermal dissociation of NH_3 results in formation of N_2 molecules which are extremely stable and nonreactive at the temperatures used, while the thermal dissociation of $AsCl_3$, in GaAs growth, results in formation of As_2 and As_4 molecules, which typically remain volatile and chemically reactive in the next step of the growth reaction. (3) The development of last-running process for very thick samples is difficult to perform due to massive condensation of reaction species on the reactor walls. The GaN reaction tends to create huge amounts of by-products such as NH_3Cl, $GaCl_3$, and $GaCl_3 \cdot NH_3$.

The kinetics of the process and growth mechanisms occurring at the solid/vapor interface during HVPE growth of GaN were simulated by several models,[82-84] assuming a surface process involving the following steps: (1) adsorption of NH_3 molecules, (2) adsorption of N atoms forming NGaCl, and (4) decomposition of the NGaCl via different desorption mechanisms. Two of them were suggested in analogy with the GaAs model: desorption forming HCl and desorption forming $GaCl_3$. One more $GaCl_2$ desorption mechanism was suggested for the GaN growth based on the experimental results.[84] Statistical treatment of the dynamic equilibrium between the adsorbed and gas-phase species allowed explicit expressions of the growth rates via the different pathways. There are several detailed

kinetics considerations published in the literature.[81] The overall dependence of growth rate upon temperature are generally agreed upon among different researchers, although details are partly in contradiction with each other. Growth rate dependence on the temperature shows two regions, a low and high temperature region with different trends.[80] The low temperature regime shows an increasing growth rate with temperature, while at high temperatures a maximum is reached at around 950°C-1080°C and growth rate decreases with further temperature increase.

Growth in the high temperature region has seen the most experimental studies due to larger practical interest stemming from the faster growth rates and better material quality obtained. Variations in the temperature value that achieve the fastest growth rate have been attributed to differences in reactor design and growth conditions. At optimum temperature, growth rate has been shown to be affected by HCl flow rate and the distance of the substrate from the gas mixing point. Growth rate is shown to increase linearly with increasing HCl flow rate and decrease exponentially with substrate distance from mixing point. High growth rate can however interfere with crystalline quality, as increasing the mixing space can improve the uniformity for the growth rate along the substrate and be helpful to avoid polycrystalline deposition.[85-88] Crystalline quality is also dependent on factors which do not affect the flow rate, including NH_3 flow rate and substrate orientation.[80]

Reactors used for the HVPE growth of GaN are based on the same initial concept and are broken down into vertical and horizontal geometries as shown in *Figure 1.2(a-d)*.[21,80,89,90] Vertical and horizontal reactors of similar designs are used for both GaN and AlN growth. The principle of both types of reactors are similar: reactant gases are introduced at optimum

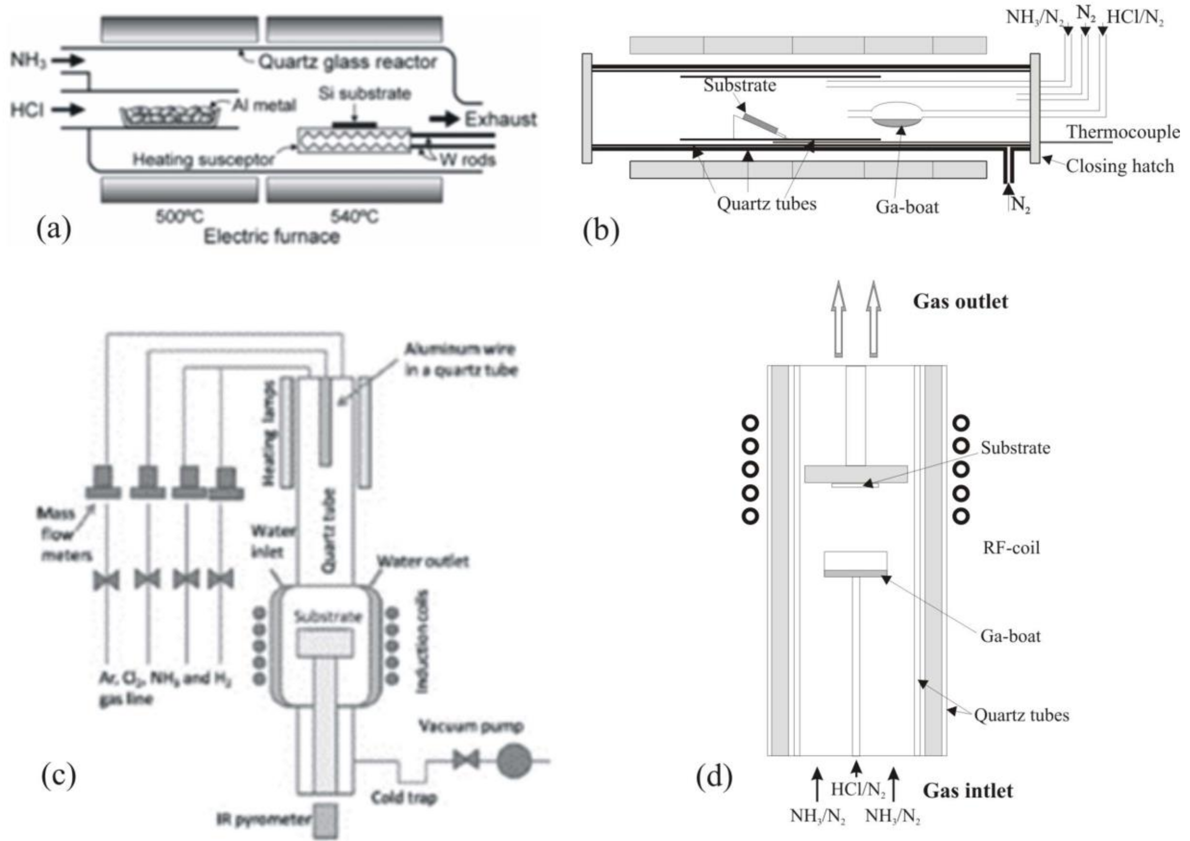

Figure 1.2 *HVPE reactors with different design: (a) Horizontal reactor with two resistive heating temperature zones used for AlN growth at temperatures up to 1410°C;[90] (b) horizontal reactor with 5 resistive heating temperature zones, allowing doping and/or ternary nitride growth;[21] (c) vertical reactor with top-down gas source low with two temperature zones with both resistive and induction heating;[89] (d) vertical reactor with RF heating.[80]*

distances to ensure mixing and optimal gas distribution, temperature is maintained in each zone by the use of resistive heating, and the sample holder is oriented in a certain position or is rotated to obtain uniform growth on the films.

In the horizontal reactor, HCl gas is introduced upstream to react with a liquid Ga pool in order to form GaCl and H_2 at about 850°C. Further downstream, a second zone can be

used for other metallic sources like In or Al, or other dopants, typically maintained at different temperature. Past this point, NH_3 is introduced at a zone in the temperature range of 1000-1060°C, where it mixes with GaCl. The GaCl and NH_3 mixture is reaching the substrate surface holder to form GaN, at temperatures ranging from 950-1150°C. The sample holder can be oriented parallel, inclined, or perpendicular to the gas flow direction depending which gives the most uniform deposition for a given reactor design. Most commonly, gas inlet tubes deliver reactant gases to the mixing point using separated quartz liners, although a coaxial arrangement has been shown to improve uniformity of the layers by achieving better mixing of the reactant gases.[87,91] For growth of compound nitrides, a reactor with two temperature zones – one for the metal container ensuring the reaction of HCl with the metal, often called source zone and one zone where the growth to take place, called growth zone - are sufficient (*Figure 1.2(a)*). For growth of ternary alloys or for doping one more temperature zone is needed for the second metal container. Some advanced reactors contain up to five temperature zones (*Figure 1.2(b)*) for ensuring higher flexibility for growing various nitrides and/or stabilizing the temperature profile at the edges. Typically each temperature zone is controlled independently.

The vertical reactor design offers benefits of improvements in film uniformity by facilitating easier substrate rotation. The substrate is held flat on a susceptor that is perpendicular to the gas flow direction (*Figure 1.2(c)*). One important modification is the implementation of a technique of lowering the substrate holder isothermally into a dump tube, in which there is a counterflow of NH_3 in a N_2 carrier gas.[80] This modification allows for an abrupt interruption of the growth, which enables the change of the gas flows in the

main tube or to slowly cool down the sample by further lowering the holder. The vertical reactor design can be further modified by supplying the process gases through the bottom inlet flange, while the top flange can be lifted for loading and unloading of substrates (*Figure 1.2(d)*). Reasons for the use of the inverted design include retaining the benefits of the vertical design while providing the possibility of raising the substrate holder and also minimization of solid particle contamination on the growing surface.

1.3.2.2. HVPE growth of AlN

The HVPE growth of AlN is similar to that of GaN - the gas mixture produced from HCl passing over the Al metal in the source zone is introduced to growth zone along with NH_3. $AlCl_3$, which is compatible with quartz is dominantly generated over AlCl, could be utilized to grow crystalline AlN at relatively low source temperatures such as 500 ^{o}C. The comprehensive thermodynamic analysis of HVPE growth of AlN was reported by Kumagai et al.[92,93]

The initial efforts on AlN HVPE growth resulted in thin epilayers, whose quality was not comparable to that by other methods such as MOCVD.[94,95] Researchers from TDI have investigated AlN HVPE growth for both thin templates[96-98] and bulk crystals[99,100]. Both SiC and Si have been used as substrates with no buffer layer. The deposition was conducted at temperatures in the range of 1000 - 1100 ^{o}C in a horizontal atmospheric hot-wall reactor, with a growth rate up to 60 μm/hr. The thick films separated from substrates have been used for seeded growth to further improve crystal quality. Typical diameter of the grown AlN boules was about 1 inch with largest one up to 1.75 inch, with resistivity exceeding 10^8 Ωcm. However, the FWHM of (0002) ω-scan was ~700 arcsec, proving the challenge to obtain

high quality crystals. AlN dislocation density reduction with increasing thickness was much less noteworthy than that of GaN, i.e. dislocation density of ~10^8 cm^{-2} still preserved at the surface for 200-μm-thick film.[101] This indicates the weak interaction (coalescence) of AlN grains at low temperature HVPE as expected.

In order to further improve the quality, HVPE at high temperature above 1200°C has been intensively studied recently. Different reactor configurations for high temperature HVPE have been adopted, as shown in *Figure 1.2*. With MOCVD grown AlN buffer layer on sapphire, Gong et al.[102] grew 12.4 μm AlN with a 102 FWHM of 600 arcsec at 1450 °C. Kumagai's group has achieved 85 μm/hr growth rate at growth temperature as high as 1400°C, though the FWHM of the (0002) rocking curve was in the order of 100 arcmin[103]. The result also confirmed that the HVPE AlN was under $AlCl_3$ mass transportation limited process even at high temperature. Later, the group has achieved FWHM of 002 rocking curve of 295 arcsec for 83-μm-thick layer grown at 1450°C under a high growth rate of 57 μm/hour.[104] The results clearly demonstrated that higher growth rates resulted in smaller FWHM of the rocking curves due to enhanced coalescence. However, the cracking is still inevitable for thick AlN layer. Pons's group found that the insertion of a low temperature nucleation layer from 650 to 850°C can improve the crystallinity of the HT AlN layer deposited at 1400 °C, as well as its morphology.[105] With further optimization, the group achieved 350 arcsec for FWHM of the 002 rocking curve.[106] The optimal V/III ratios were also reported under specific growth conditions,[90,107] though the group did not observe strong growth rate dependency on V/III or NH_3, contrast to what Yamane et al. observed.[93]

Recently, Nitride Solutions Inc. has made a significant progress on AlN template growth. The company is producing ~1-4 μm high quality AlN templates on sapphire. The FWHM of 002 and 102 rocking curves are below 250 and 450 arcsec respectively. The UV transparency of 2 μm films are greater than 80% with low level of C and O concentration. In order to further improve the film thickness and quality without cracking, patterned substrates have been used. By adopting grooved patterns on SiC, the critical thickness of AlN was increased significantly and FWHM of 100 rocking curves reached 833 arcsec for 22-μm-thick film[108] and 525 arcsec for 35−μm-thick film[109]. The more than two-order dislocation density reduction by utilizing LEO with proper patterns is significant in AlN HVPE growth.[110] However, the issues encountered in GaN HVPE such as cracking during growth, cool-down cracking, and surface morphology degrading are still expected in HVPE AlN for thick free-standing bulk growth. The so called weak-interface method, widely adopted in GaN HVPE, was employed by Kumagai et al[111,112] to achieve thick AlN, followed by self-separation during cool-down. A 85 μm thick free-standing AlN was separated from sapphire with interfacial voids. The same group also used Si as a substrate and obtained 112 μm free standing AlN by etching away the silicon substrate. However, the Si impurity level in AlN was as high as 10^{19} due to contamination from the substrate used.[91]

1.3.2.3. HVPE growth of AlGaN templates

Growth of low-defect AlGaN used as template (or bulk) substrates is highly desirable for fabrication of advanced AlGaN-based power devices, high frequency transistors, and UV LEDs. While other growth methods have been tried such as solution growth technique,[113] the well-established HVPE technology developed for both AlN and GaN is currently the most

successful in growing AlGaN templates up to 2-mm-thick bulk substrates, as reported in patent application.[114]

The thermodynamic analysis of AlGaN HVPE has been reported by Koukitu et al.,[115] and the effect of H_2 was studied in detail later.[116] It was found that the AlGaN growth was in thermo-equilibrium and the dependency of AlGaN composition was calculated on the growth conditions, which agreed with the experimental results.[117]

In HVPE growth of AlGaN, in-situ formation of $AlCl_3$ and GaCl by passing HCl through metal aluminum and gallium pools, are utilized to provide the III-species. A wide range of $Al_xGa_{1-x}N$ with composition x varying from 0 to 1 have been successfully grown by HVPE. One of the big challenges for AlGaN HVPE is the composition uniformity across the template radius and thickness, as well as the cracking. The uniformity complications can result from: (i) temperature non-uniformity across the wafer due to different driving force for AlN and GaN deposition, since the response of the Gibbs energy on temperature is totally in reverse for AlN and GaN formation; (ii) different diffusivities of $AlCl_3$ and GaCl in the gas phase, leading to different composition across the wafer even in reactor equipped with a premixed $AlCl_3$ and GaCl source; (iii) preferred incorporation of gallium over aluminum on non-c-plane facets during coalescence across the growth thickness.

Different substrates have been used for AlGaN template growth by HVPE. Sapphire is the most commonly used substrate,[116-120] while SiC[121] has also been investigated. In order to reduce cracking, increase growth thickness, and achieve lower defect density, trench and honeycomb patterned sapphire both with AlN buffer layers have also been used and 40 μm $Al_{0.45}Ga_{0.55}N$[122] and 20 μm thick $Al_{0.3}Ga_{0.7}N$ has been demonstrated.[123]

1.3.3. Ammonothermal growth

The ammonothermal growth process is conducted by transporting the mass from high- to low- temperature zones and has been reported to possess several advantages,[80] including: (i) lower dissolution density due to solubilizing in the higher temperature zone, (ii) lower probability of cubic formation, (iii) absence of disastrous effects of the basic solution on the autoclave materials, which results in safety improvements and cost effectiveness. Compared to other techniques, ammonothermal growth is characterized with relatively low growth rate capacity, however, it requires relatively low temperature and reasonable pressure, which allows controllable recrystallization enabling high-quality material.

The ammonothermal technique employs a solvothermal process, which allows solubilization of polycrystalline III-nitride nutrient or feedstock in supercritical ammonia under high pressure by utilizing a solubilizing agent or mineralizer.[78] The type of mineralizer determines the main type of the ammonothermal approach, which in turn determines their advantages and disadvantages. Mineralizers are divided into three groups: (i) basic mineralizers, which introduce NH_2^- ions to the solution, (ii) acidic mineralizers, which introduce NH_4^+ ions, and (iii) neutral mineralizers which introduce neither NH_2^- ions nor NH_4^+ ions. Dissolution of III-nitrides using potassium azide (KN_3) or potassium amide (KNH_2) ammonothermal-basic solutions have been suggested by several groups[124-127] to occur through the formation of soluble intermediate compounds, which subsequently decompose with temperature. Other crystalline mechanisms, which involve forward solubility of nitride species, have been reported[124,128,129] for ammonothermal-acidic solutions, which utilize ammonium halide mineralizers.

The quality of ammonothermally grown GaN material still requires detailed evaluation, as optimization of the growth conditions and producing a systematic series for thorough analysis will take some time. The best results in terms of crystallinity were reported for self-prepared seed and multiple regrowth processes.[130] The first experimental results indicate that the properties of the ammonothermal GaN material are strongly influenced by the quality of the seeds used. With further research, ammonothermal growth is very promising for its ability to be scalable by supporting growth of large crystals and multiple simultaneous seeded growths.

1.3.4. Solution growth at high pressure, high temperature

Solution growth at high pressure and high temperature (HPSG) has been proven as a viable technique for many semiconductors. Despite over two decades of effort with GaN semiconductors, equilibrium solution growth proved to be challenging due to its high melting temperature and high associated equilibrium N_2 pressure (>45kbar).[78] Due to the very low solubility of nitrogen in Ga of only ~1%, the growth rate is very low and crystal sizes have been limited to several millimeter long prisms or 15mm x 20mm lateral-size platelets for about 200h growth time.[131]

HPSG has produced the highest structural quality GaN material with dislocation density lower than 100 cm^{-2}, however the dominating lateral growth mode observed under these conditions favors higher levels of background impurity incorporation. While the dominating impurity, oxygen (~10^{19} cm^{-3}), leads to a high n-type carrier density which is beneficial for many devices, the ability to control the carrier density is important for most applications. HPSG has also been shown capable of producing AlGaN bulk crystals of high

crystalline quality by providing both Ga and Al sources and carefully controlling the nitrogen solubility and temperature.

1.3.5. Mixed growth methods

Another approach that recently attracted significant attention is the so called "seeded growth" method. The approach aims at combining the high growth rate and higher crystalline quality achievable by the homoepitaxial regrowth employing GaN seeds instead of using sapphire to avoid the initial highly defective interface region. Several alternatives of seeded growth have been elaborated recently by researches from Unipress. Namely, seeds produced either by HPSG, HVPE or ammonothermal growth methods have been used for regrowth by HVPE or vice versa.

The first type of seeded growth listed above was reported first due to the early availability of high quality HPSG crystals, although of small form factor. The main challenge of this seeded growth was the expansion of the seed crystal.[132,133] In HVPE growth of GaN, crystal expansion can be controlled through physical-chemical gradients and concentrations, which result in stabilization of crystal planes under the appropriate growth conditions. For in-plane expansion, size expansion will depend on the anisotropy of the growth rates for different crystallographic planes. Growth parameters, such as temperature, pressure, growth rate (source species flux) or the ratio between the nitrogen and the gallium species, can influence the stabilization of one crystal plane over another. Additionally, the geometric configuration of the seed in the system may contribute to the flux of the growth species from additional sources, such as surface migration. As shown in the ELOG growth of GaN, inclined crystalline facets can be formed under certain growth conditions that give

undesirable crystalline morphologies.[134,135] An important part of the growth process development is to identify growth parameters that give a planar (as opposed to prismatic) crystal, and then find the way to extend the growth in directions normal to those edge planes. One issue that has been observed with seed expansion is the variation in impurity content and carrier concentration. The physical and electrical properties of GaN grown by HVPE are very sensitive to the orientation of the crystallization front. This could present a challenge for bulk growth, particularly for undoped and semi-insulating material, where a low background concentration of shallow impurities, such as oxygen, is desired.

With the availability of larger wafers, produced by HVPE, the regrowth by HVPE was optimized and proven successful in maintaining the seed wafers size during the HVPE seeded growth.[136] Even the very early HVPE regrowth on HVPE free-standing crystals showed that the material produced during regrowth possesses significantly improved structural characteristics. In particular, the dislocation density was found to be noticeably reduced. The analysis of the defect density in the regrown HVPE-GaN with different thicknesses has shown that the trend of decreasing the defect density with increasing thickness remains.[137] The high purity of the crystals and the high optical quality have been proven reproducible. In particular, the low temperature photoluminescence (PL) spectra of the regrown GaN films showed comparable narrow (~2 meV) exciton peaks as in the PL spectrum of the seed. However, based on different studies performed by variety of techniques, such as X-ray diffraction, PL, and Raman scattering spectroscopies, it is clear that both the residual strain and curvature (radius of about 10 m in the best case) of the seed was reproduced, which remains the main undesirable characteristics of these materials.[136,137]

The most recent availability of low-dislocation-density wafers grown by ammonothermal method open a new possibility for homoepitaxial seeded growth. The HVPE seeded growth on such seeds has also been proven successful in reproducing the seed characteristics in regard to very low curvature (radius close to 100 m) and low dislocation density (in the angle of $10^4 cm^{-2}$).[138] Moreover, in contrast to the ammonothermal seed characteristics, the HVPE-GaN wafer grown on ammonothermal seed possessed high purity and transparency, which are typical characteristics for the HVPE growth. Thus, the combination of the two methods seems to enable the advantages of both in the regrown material.

1.4. Properties of nitride substrates

The three main characteristics that are particularly important for substrate applications and determine the demand for homoepitaxial growth on bulk nitride substrate over the widely established heteroepitaxial growth on sapphire are the following: low dislocation density, controllable electrical conductivity in wide range and high thermal conductivity. All characteristics are strongly dependent on the growth methods and process strategies.

1.4.1. Defect density

The dislocation density and distribution represent especially important characteristics. Currently the lowest reported values for AlN and GaN substrates are in the range of $10^2 – 10^4$ cm^{-2} for AlN grown by sublimation[139] and for GaN grown by ammonothermal method.[140] Unfortunately, the low dislocation density for both materials are accompanied by relatively high point defect densities.

There are two primary approaches towards decreasing the dislocation density in HVPE-GaN: (i) ELOG-type approach, employing stripe or star patterning and (ii) increasing GaN thickness with the ultimate goal to to grow boules that allow wafer slicing. The ELOG approaches can provide areas of very low defect density, where the lateral growth mode dominates. However, the approach results in nonuniform lateral distribution of dislocation across the wafer surface which requires a very precise alignment of the subsequent technology steps for device structure growth.

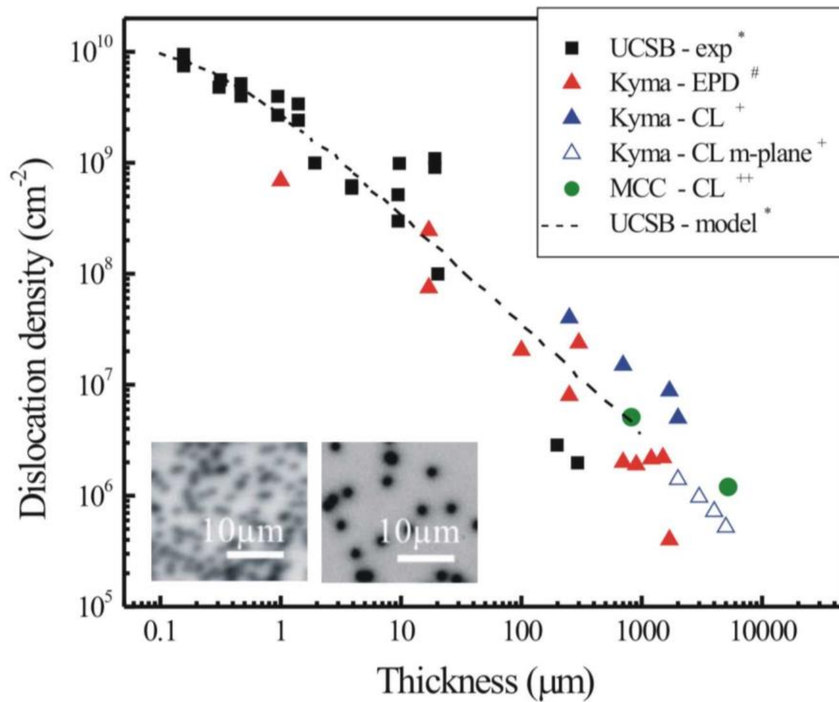

Figure 1.3 *Combined graph of experimental data and theoretical predictions for dislocation density as a function of the GaN layer thickness. *Mathis et al.;[141] #Hanser et al.;[142] +Paskova et al.;[79] ++Fujimori et al.[143] Inset: Representative panchromatic CL images visualizing in-plane dislocation distribution in GaN layer grown by HVPE with thickness of about 150 μm (left) and 700 μm (right).*

The second approach of increasing the layer thickness allows for annihilation of mixed dislocations with opposite Burger's vectors[141] and/or by point defect assisted dislocation climb leads to a substantial decrease of dislocation density along the growth direction. This method has the advantage of uniform lateral dislocation density as shown in the cathodoluminesce (CL) panchromatic images for GaN layers with 30 and 600 mm thickness, shown in the inset of *Figure 1.3*. *Figure 1.3* shows the trend of dislocation density versus GaN layers thickness, summarizing results obtained by different characterization techniques,[79,141-143] namely by transmission electron microscopy (TEM), CL topography,[142,143] atomic force microscopy and different etching procedures.[144,145] The experimental data shows a monotonic decrease of dislocation density with GaN layer thickness over several orders of magnitude, consistent with the theoretical predictions.

1.4.2. Doping and electrical conductivity

All bulk AlN is known to have substantial amount of residual impurities and point defects, which are responsible for coloring of the bulk crystals and for reducing its transparency. Various technological strategies have been explored with the ultimate goal to reduce the background impurity concentration with modest success. Efforts for intentional doping of bulk AlN crystals to systematically alter the electrical properties of the material are rare although doping by Si has been reported.[146,147]

GaN substrates have been demonstrated with n-type and p-type conductivity, as well as semi-insulating. All undoped GaN still retains n-type conductivity due to unavoidable oxygen and silicon residual impurities. The lowest silicon and oxygen concentrations varies for the different growth techniques, growth reactor ambient, sources and growth procedures.

The lowest residual impurity levels have been reported in the range of 10^{15}cm^{-3} for HVPE growth.[21]

Intentional n-type doping has been reported by various impurities, attempting controllable doping in wide range. Currently, the most developed approach for n type doping was reported for O and Si impurities introduced by gaseous or solid sources. Typical gaseous Si dopant precursors for HVPE growth include silane, disilane and dichloresilane. Alternatively, Si doping can be achieved in HVPE by exposing Si to the HCl gas to form $SiCl_x$ which then transports to and reacts with the growing film. HVPE grown bulk GaN doped with Si by using a SiH_4 source was reported to result in material with carrier concentration in the range of $1.3x10^{16}$ – $8.3x10^{18}$ cm^{-3} while maintaining high crystalline and optical quality.[148] Alternative doping with oxygen, using gaseous source of high quality was also reported to achieve carrier concentration up to $8.5x10^{18}$ cm^{-3}. Temperature dependence of Hall carrier concentration and mobility of two such representative samples doped with Si (n=$7.3x10^{16}$ cm^{-3}) and O (n=$2x10^{17}$ cm^{-3}) are shown in *Figure 1.4(a)* and *(b)*, respectively, showing similar trends as the ones for undoped material with the offset related to the higher free carrier concentrations.

P-type doping of GaN bulk material was reported by both HVPE and ammonothermal techniques. Today Mg is the element proven to be the most efficient and controllable in achieving p-type conductivity. Despite that, high hole concentrations are challenging due to the high thermal activation energy of Mg, 150-200 meV,[149] which results in only a few percent of the Mg acceptor ionization at room temperature. Additionally, post-growth annealing is required for removing the hydrogen passivation of the Mg dopant. Other

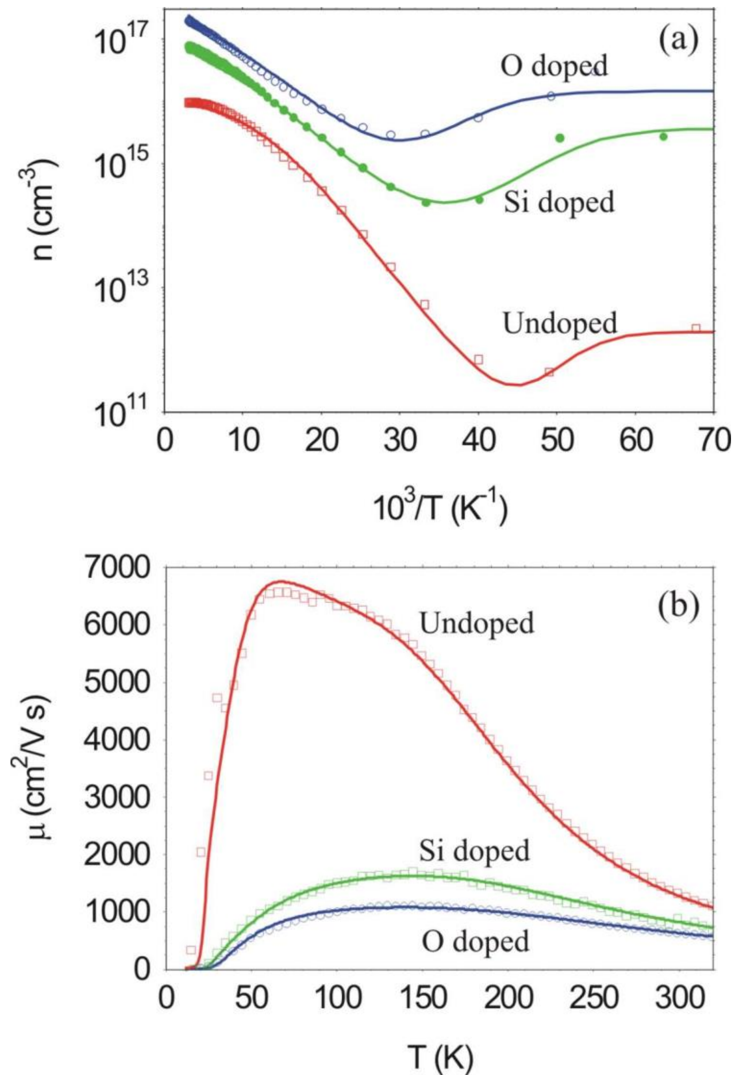

Figure 1.4 *Temperature dependence of (a) free electron concentration and (b) mobility as determined by Hall effect measurements for three representative samples: undoped, Si doped, and O doped. (Courtesy of David Look)*

elements such as Zn and Cd have also been used but with even less activation efficiency due to their larger thermal activation energy and much less activation achievable at room temperature. The doping with Mg in HVPE was done by either using a separate temperature zone and source bath or by mixing the Mg in the Ga source. The HCl gas, reacting with Mg

can for MgCl which is transported to the growth zone.[150] The role of H carrier gas was reported in a controversial way. Although one would expect that it is preferable to use inert carrier gas to avoid Mg-H passivation, the experimental results have shown preferable behavior of the passivation during growth to prevent the incorporation of residual donor impurities.[151] Thus, despite the technological breakthroughs in growing p-type GaN by HVPE, the reports are very limited and the exact governing mechanisms remain unclear.

Semi-insulating GaN bulk substrates are currently only possible by doping with compensating elements and were reported grown by HVPE and ammonothermal growth methods. The ammonothermal approach has used various compensating elements such as Fe, Mg, Zn, and Cd.[130] The most promising approach suggested so far in HVPE growth is doping with Fe using metalorganic source. The material was reported with high resistivity (larger than 10^6 Ωcm). Reports on this topic are relatively limited, and the compensation mechanisms are not fully understood, but the growth of semi insulating GaN with high quality was proven successful.

1.5. Conclusions

The nitride substrate technologies have made a remarkable progress in the last two decades, though their development still lags behind the nitride thin-film device technology. Recent advances in nitride bulk crystal growth led to a significant improvement of material quality, which allowed better understanding of their properties and more correct estimation of their fundamental properties. Yet, growth related defects, doping and thermal conductivity remain not fully elucidated and more research is needed in order to reveal their interplay and to be fully controlled.

References

1 J. Y. Duboz, GaN as Seen by the Industry, Physica Status Solidi (a) 176, 5 (1999).

2 Progress of GaN transistors, Power Electronics Europe 3, (2015).

3 Gallium Nitride - 2003, Technology Status, Applications, and Market Forecasts, Strategies Unlimited (2003).

4 V. Y. Davydov, A. A. Klochikhin, V. V. Emtsev, D. A. Kurdyukov, S. V. Ivanov, V. A. Vekshin, F. Bechstedt, J. Furthmuller, J. Aderhold, J. Graul, A. V. Mudryi, H. Harima, A. Hashimoto, A. Yamamoto, and E. E. Haller, Band Gap of Hexagonal InN and InGaN Alloys, Physica Status Solidi (B) 234, 787 (2002).

5 S. J. Pearton, C. R. Abernathy, M. E. Overberg, G. T. Thaler, A. H. Onstine, B. P. Gila, F. Ren, B. Lou, and J. Kim, New applications advisable for gallium nitride, Materials Today 5, 24 (2002).

6 M. Kuzuhara, and H. Tokuda, Low-Loss and High-Voltage III-Nitride Transistors for Power Switching Applications, Ted 62, 405 (2015).

7 L. Liu, and J. H. Edgar, Substrates for gallium nitride epitaxy, Materials Science & Engineering R 37, 61 (2002).

8 R. Stevenson, GaN substrates offer high performance at a price, Compound Semiconductor Magazine 10, (2004).

9 K. Evans, Native substrates spar with established technology, 10, (2004).

10 O. Ambacher, Growth and applications of Group III-nitrides, Journal of Physics D: Applied Physics 31, 2653 (1998).

11 B. Beaumont, P. Vennegues, and P. Gibart, Epitaxial Lateral Overgrowth of GaN, Physica Status Solidi (B) 227, 1 (2001).

12 J. K. Sheu, and G. C. Chi, The doping process and dopant characteristics of GaN, Journal of Physics: Condensed Matter 14, (2002).

13 S. J. Pearton, J. C. Zolper, R. J. Shul, and F. Ren, GaN: Processing, defects, and devices, Journal of Applied Physics 86, 1 (1999).

14 S. J. Pearton, F. Ren, A. P. Zhang, and K. P. Lee, Fabrication and performance of GaN electronic devices, Materials Science & Engineering R 30, 55 (2000).

15 H. Morkoç, R. Cingolani, and B. Gil, Polarization effects in nitride semiconductor device structures and performance of modulation doped field effect transistors, Solid State Electronics 43, 1909 (1999).

16 H. Morkoc, and L. Liu, GaN-Based MODFET and HBT, 547 (2004).

17 B. Monemar, and G. Pozina, Group III-nitride based hetero and quantum structures, Progress in Quantum Electronics 24, 239 (2000).

18 J. W. Orton, and C. T. Foxon, Group III nitride semiconductor for short wavelength light-emitting devices, Reports on Progress in Physics 61, 1 (1998).

19 E. Muñoz, E. Monroy, J. L. Pau, F. Calle, F. Omnès, and P. Gibart, III nitrides and UV detection, Journal of Physics: Condensed Matter 13, 7115 (2001).

20 D. A. Steigerwald, J. C. Bhat, D. Collins, R. M. Fletcher, M. O. Holcomb, M. J. Ludowise, P. S. Martin, and S. L. Rudaz, Illumination with solid state lighting technology, Jstqe 8, 310 (2002).

21 T. Paskova, and M. Bickermann, Vapor Transport Growth of Wide Bandgap Materials, 621 (2015).

22 S. D. Lester, F. A. Ponce, M. G. Craford, and D. A. Steigerwald, High dislocation densities in high efficiency GaN-based light-emitting diodes, Applied Physics Letters 66, 1249 (1995).

23 S. Nakamura, InGaN-based violet LDs, Semiconductor Science and Technology 14, (1999).

24 S. Porowski, I. Grzegory, S. Krukowski, M. Leszczynski, P. Perlin, and T. Suski, Blue lasers on high pressure grown GaN single crystal substrates, Europhysics News 35, 69 (2004).

25 T. Sugahara, H. Sato, M. Hao, Y. Naoi, S. Kurai, S. Tottori, K. Yamashita, K. Nishino, L. T. Romano, and S. Sakai, Direct Evidence that Dislocations are Non-Radiative Recombination Centers in GaN, Japanese Journal of Applied Physics 37, (1998).

26 X. A. Cao, J. A. Teetsov, F. Shahedipour-Sandvik, and S. D. Arthur, Microstructural origin of

leakage current in GaN/InGaN ligh-emitting diodes, Journal of Crystal Growth 264, 172 (2004).

27 Z. Z. Chen, J. Zhao, Z. X. Qin, X. D. Hu, T. J. Yu, Y. Z. Tong, Z. J. Yang, X. Y. Zhou, G. Q. Yao, B. Zhang, and G. Y. Zhang, Study on the stability of the high-brightness white LED, Physica Status Solidi (B) 241, 2664 (2004).

28 J. Y. Tsao, Solid-state lighting: lamps, chips, and materials for tomorrow, Cd-M 20, 28 (2004).

29 J. W. P. Hsu, and M. J. Manfra, Direct imaging of reverse-bias leakage through pure screw dislocations
in GaN films grown by MBE on GaN templates, Applied Physics Letters 81, 79 (2002).

30 J. W. P. Hsu, M. J. Manfra, D. V. Lang, S. Richter, S. N. G. Chu, A. M. Sergent, R. N. Kleiman, L. N. Pfeiffer, and R. J. Molnar, Inhomogeneous spatial distribution of reverse bias leakage in GaN Schottky diodes, Applied Physics Letters 78, 1685 (2001).

31 C. Hsu, W. Lan, and Y. S. Wu, Effect of thermal annealing of Ni/Au ohmic contact on the leakage current of GaN based light emitting diodes, Applied Physics Letters 83, 2447 (2003).

32 A. Yamada, Y. Kawaguchi, and T. Yokogawa, Reduction of leakage current of p–n junction by using air-bridged lateral epitaxial growth technique, Physica Status Solidi (C)2494 (2003).

33 L. S. McCarthy, I. P. Smorchkova, H. Xing, P. Kozodoy, P. Fini, D. L. Limb, J. S. Pulfrey, M. J. Speck, J. W. Rodwell, S. P. DenBaar, and U. K. Mishra, GaN GHBT: Toward an RF device, IEEE Transactions on Electron Devices 48, 543 (2001).

34 F. Rampazzo, G. Pierobon, D. Pacetta, C. Gaquiere, D. Theron, B. Boudart, G. Meneghesso, and E. Zanoni, Hot carrier aging degradation phenomena in GaN based MESFETs, Microelectronics Reliability 44, 1375 (2004).

35 L. Liu, and J. H. Edgar, Transport effects in the sublimation growth of aluminum nitride, Journal of Crystal Growth 220, 243 (2000).

36 V. Noveski, R. Schlesser, S. Mahajan, S. Beaudoin, and Z. Sitar, Mass transfer in AlN crystal growth at high temperatures, Journal of Crystal Growth 264, 369 (2004).

37 B. Liu, J. H. Edgar, B. Raghothamachar, M. Dudley, J. Y. Lin, H. X. Jiang, A. Sarua, and M. Kuball, Free nucleation of aluminum nitride single crystals in HPBN crucible by sublimation, Materials Science & Engineering B 117, 99 (2005).

38 D. Zhuang, J. H. Edgar, B. Liu, H. E. Huey, H. X. Jiang, J. Y. Lin, M. Kuball, F. Mogal, J. Chaudhuri, and Z. Rek, Bulk AlN crystal growth by direct heating of the source using microwaves, Journal of Crystal Growth 262, 168 (2004).

39 R. Dalmau, B. Raghothamachar, M. Dudley, R. Schlesser, and Z. Sitar, Crucible Selection in AlN Bulk Crystal Growth, MRS Online Proceedings Library 798, (2003).

40 G. A. Slack, J. Whitlock, K. Morgan, and L. J. Schowalter, Properties of Crucible Materials for Bulk Growth of AlN, MRS Online Proceedings Library 798, (2003).

41 B. M. Epelbaum, D. Hofmann, M. Bickermann, and A. Winnacker, Sublimation Growth of Bulk AlN Crystals: Materials Compatibility and Crystal Quality, Materials Science Forum 389-393, 1445 (2002).

42 D. W. Brenner, R. Schlesser, Z. Sitar, R. Dalmau, R. Collazo, and Y. Li, Model for the influence of
boron impurities on the morphology of AlN grown by PVT, Surface Science 560, (2004).

43 B. Liu, D. Zhuang, and J. H. Edgar, AlN Grown by Sublimation, 59 (2002).

44 G. A. Slack, L. J. Schowalter, D. Morelli, and J. A. Freitas, Some effects of oxygen impurities on AlN and GaN, Journal of Crystal Growth 246, 287 (2002).

45 S. Y. Karpov, A. V. Kulik, I. N. Przhevalskii, M. S. Ramm, and Y. N. Makarov, Role of oxygen in AlN sublimation growth, Physica Status Solidi (C)1989 (2003).

46 M. Bickermann, B. M. Epelbaum, and A. Winnacker, PVT growth of bulk AlN crystals with low oxygen contamination, Physica Status Solidi (C)1993 (2003).

47 V. Noveski, R. Schlesser, B. Raghothamachar, M. Dudley, S. Mahajan, S. Beaudoin, and Z. Sitar, Seeded growth of bulk AlN crystals and grain evolution in polycrystalline AlN boules, Journal of Crystal Growth 279, 13 (2005).

48 G. A. Slack, Nonmetallic crystals with high thermal conductivity, Journal of Physics and Chemistry of Solids 34, 321 (1973).

49 J. C. Rojo, L. J. Schowalter, K. Morgan, D. I. Florescu, F. H. Pollak, B. Ragothamachar, and M. Dudley, Single crystal AlN substrate preparation from bulk crystals, Materials Reseach Symposium Proceedings 680, (2001).

50 P. Lu, R. Collazo, R. F. Dalmau, G. Durkaya, N. Dietz, and Z. Sitar, Different optical absorption edges in AlN bulk crystals grown in m- and c-orientations, Applied Physics Letters 93, 131922 (2008).

51 Q. Yan, A. Janotti, Van de Walle, Chris G, and M. Scheffler, Origins of optical absorption and emission lines in AlN, Applied Physics Letters 105, 111104 (2014).

52 M. Bickermann, B. M. Epelbaum, O. Filip, P. Heimann, S. Nagata, and A. Winnacker, UV transparent single-crystalline bulk AlN substrates, Physica Status Solidi (C) 7, 21 (2010).

53 M. Tanaka, S. Nakahata, K. Sogabe, H. Nakata, and M. Tobioka, Morphology and X-Ray Diffraction Peak Widths of Aluminum Nitride Single Crystals Prepared by the Sublimation Method, Japanese Journal of Applied Physics 36, (1997).

54 B. M. Epelbaum, C. Seitz, A. Magerl, M. Bickermann, and A. Winnacker, Natural growth habit of bulk AlN crystals, Journal of Crystal Growth 265, 577 (2004).

55 N. B. Singh, A. Berghmans, H. Zhang, T. Wait, R. C. Clarke, J. Zingaro, and J. C. Golombeck, Physical vapor transport growth of large AlN crystals, Journal of Crystal Growth 250, 107 (2003).

56 J. H. Edgar, L. H. Robins, S. E. Coatney, L. Liu, K. Ignatiev, and Z. Rek, A comparison of aluminum
nitride freely nucleated and seeded on 6H-SiC, Materials Science Forum 338-342, 1599 (2000).

57 J. H. Edgar, B. Liu, L. Liu, D. Zhuang, J. Chaudhuri, M. Kuball, and S. Rajasingam, Bulk AlN crystal growth: self-seeding and seeding on 6H-SiC substrates, Journal of Crystal Growth 246, 187 (2002).

58 Y. Shi, Z. Y. Xie, B. Liu, L. H. Liu, J. H. Edgar, and M. Kuball, Influence of buffer layer and 6H-SiC substrate polarity on the nucleation of AlN grown by the sublimation sandwich technique, Journal of Crystal Growth 233, 177 (2001).

59 M. Kuball, J. M. Hayes, Y. Shi, and J. H. Edgar, Phonon lifetimes in bulk AlN and their temperature dependence, Applied Physics Letters 77, 1958 (2000).

60 B. Raghothamachar, W. M. Vetter, M. Dudley, R. Dalmau, R. Schlesser, Z. Sitar, E. Michaels, and J. W. Kolis, Synchrotron white beam topography characterization of physical vapor transport grown AlN and ammonothermal GaN, Journal of Crystal Growth 246, 271 (2002).

61 G. A. Slack, and T. F. McNelly, Ain single crystals, Journal of Crystal Growth 42, 560 (1977).

62 J. C. Rojo, G. A. Slack, K. Morgan, L. J. Schowalter, and M. Dudley, Growth of Self-Seeded Aluminum Nitride by Sublimation-Recondensation and Substrate Preparation, MRS Online Proceedings Library 639, (2000).

63 L. J. Schowalter, J. C. Rojo, N. Yakolev, Y. Shusterman, K. Dovidenko, R. Wang, I. Bhat, and G. A. Slack, Preparation and Characterization of Single-Crystal Aluminum Nitride Substrates, 1999 Materials Research Society Fall Meeting, Boston, MA (US), 11/28/1999--12/03/1999 (Jul 1, 2000).

64 N. L. Yakovlev, J. C. Rojo, and L. J. Schowalter, Morphology of facets on vapor-grown AIN crystals, Surface Science 493, 519 (2001).

65 B. Raghothamachar, M. Dudley, J. C. Rojo, K. Morgan, and L. J. Schowalter, X-ray characterization of bulk AIN single crystals grown by the sublimation technique, Journal of Crystal Growth 250, 244 (2003).

66 C. M. Balkaş, Z. Sitar, T. Zheleva, L. Bergman, R. Nemanich, and R. F. Davis, Sublimation growth and characterization of bulk aluminum nitride single crystals, Journal of Crystal Growth 179, 363 (1997).

67 B. Liu, Y. Shi, L. Liu, J. H. Edgar, and D. N. Braski, Surface Morphology and Composition Characterization at the Initial Stages of AlN Crystal Growth, MRS Online Proceedings Library 639, (2000).

68 L. Liu, D. Zhuang, B. Liu, Y. Shi, J. H. Edgar, S. Rajasingam, and M. Kuball, Characterization of Aluminum Nitride Crystals Grown by Sublimation, Physica Status Solidi (a) 188, 769 (2001).

69 L. Liu, B. Liu, Y. Shi, and J. H. Edgar, Growth Mode and Defects in Aluminum Nitride Sublimed on (0001) 6H-SiC Substrates, MRS Internet Journal of Nitride Semiconductor Research 6, 7 (2001).

70 Y. Shi, B. Liu, L. Liu, J. H. Edgar, H. M. Meyer III, E. A. Payzant, L. R. Walker, N. D. Evans, J. G. Swadener, J. Chaudhuri, and J. Chaudhuri, Initial Nucleation Study and New Technique for Sublimation Growth of AlN on SiC Substrate, Physica Status Solidi (a) 188, 757 (2001).

71 Y. Shi, B. Liu, L. Liu, J. H. Edgar, E. A. Payzant, J. M. Hayes, and M. Kuball, New Technique for Sublimation Growth of AlN Single Crystals, MRS Internet Journal of Nitride Semiconductor Research 6, 5 (2001).

72 B. Heying, X. H. Wu, S. Keller, Y. Li, D. Kapolnek, B. P. Keller, S. P. DenBaars, and J. S. Speck, Role of threading dislocation structure on the x-ray diffraction peak widths in epitaxial GaN films, Applied Physics Letters 68, 643 (1996).

73 T. Metzger, R. Höpler, E. Born, S. Christiansen, M. Albrecht, H. P. Strunk, O. Ambacher, M. Stutzmann, R. Stömmer, M. Schuster, and H. Göbel, Coherent X-Ray Scattering Phenomenon in Highly Disordered Epitaxial AlN Films, Physica Status Solidi (a) 162, 529 (1997).

74 R. Schlesser, R. Dalmau, and Z. Sitar, Seeded growth of AlN bulk single crystals by sublimation, Journal of Crystal Growth 241, 416 (2002).

75 V. Noveski, R. Schlesser, J. Freitas, S. Mahajan, S. Beaudoin, and Z. Sitar, Vapor phase transport of AlN in an RF heated reactor: Low and high temperature studies, MRS Online Proceedings Library 798, (2003).

76 D. Zhuang, Z. G. Herro, R. Schlesser, and Z. Sitar, Seeded growth of AlN single crystals by physical vapor transport, Journal of Crystal Growth 287, 372 (2006).

77 P. Lu, R. Collazo, R. F. Dalmau, G. Durkaya, N. Dietz, B. Raghothamachar, M. Dudley, and Z. Sitar, Seeded growth of AlN bulk crystals in m- and c-orientation, Journal of Crystal Growth 312, 58 (2009).

78 T. Paskova, and K. R. Evans, GaN Substrates-Progress, Status, and Prospects, IEEE Journal of Selected Topics in Quantum Engineering 15, 1041 (2009).

79 T. Paskova, D. A. Hanser, and K. R. Evans, GaN Substrates for III-Nitride Devices, Proceedings of the IEEE 98, 1324 (2010).

80 B. Feigelson, and T. Paskova, Growth of Bulk GaN Crystals, (2011), p. 232.

81 T. Paskova, and B. Monemar, HVPE-GaN Quasi-Substrates for Nitride Device Structures, 79 (2002).

82 E. Aujol, J. Napierala, A. Trassoudaine, E. Gil-Lafon, and R. Cadoret, Hydrogen and nitrogen ambient effects on epitaxial growth of GaN by hydride vapour phase epitaxy, Journal of Crystal Growth 230, 372 (2001).

83 R. Cadoret, Growth mechanisms of (00.1)GaN substrates in the hydride vapour-phase method: surface diffusion, spiral growth, H2 and GaCl3 mechanisms, Journal of Crystal Growth 205, 123 (1999).

84 A. Trassoudaine, E. Aujol, R. Cadoret, T. Paskova, and B. Monemar, A new mechanism in the growth process of GaN by HVPE, MRS Online Proceedings Library 639, (2000).

85 T. Paskova, E. B. Svedberg, A. Henry, I. G. Ivanov, R. Yakimova, and B. Monemar, Thick GaN layers grown on a-plane sapphire substrates by hydride vapour phase epitaxy, Physica Scripta 1999, 67 (1999).

86 A. Shintani, and S. Minagawa, Kinetics of the epitaxial growth of GaN using Ga, HCl and NH3, Journal of Crystal Growth 22, 1 (1974).

87 W. Seifert, R. Franzheld, E. Butter, H. Sobotta, and V. Riede, On the origin of free carriers in high-conducting n-GaN, Crystal Research and Technology 18, 383 (1983).

88 S. S. Liu, and D. A. Stevenson, Growth Kinetics and Catalytic Effects in the Vapor Phase Epitaxy of Gallium Nitride, Journal of the Electrochemical Society 125, 1161 (1978).

89 N. Coudurier, R. Boichot, V. Fellmann, A. Claudel, E. Blanquet, A. Crisci, S. Coindeau, D. Pique, and M. Pons, Effects of the V/III ratio on the quality of aluminum nitride grown on (0001) sapphire by high temperature hydride vapor phase epitaxy, Physica Status Solidi. C, Current Topics in Solid State Physics 10, 362 (2013).

90 Y. Kumagai, T. Nagashima, H. Murakami, K. Takada, and A. Koukitu, Characterization of a freestanding AlN substrate prepared by hydride vapor phase epitaxy, Physica Status Solidi (C) 5, 1512 (2008).

91 S. A. Safvi, N. R. Perkins, M. N. Horton, R. Matyi, and T. F. Kuech, Effect of reactor geometry and growth parameters on the uniformity and material properties of GaN sapphire grown by hydride vapor-phase epitaxy, Journal of Crystal Growth 182, 233 (1997).

92 Y. Kumagai, T. Yamane, T. Miyaji, H. Murakami, Y. Kangawa, and A. Koukitu, Hydride vapor phase epitaxy of AlN: thermodynamic analysis of aluminum source and its application to growth, Physica Status Solidi (C) 0, 2498 (2003).

93 T. Yamane, H. Murakami, Y. Kangawa, Y. Kumagai, and A. Koukitu, Growth of thick AlN layer on sapphire (0001) substrate using hydride vapor phase epitaxy, Physica Status Solidi (C) 2, 2062 (2005).

94 W. M. Yim, E. J. Stofko, P. J. Zanzucchi, J. I. Pankove, M. Ettenberg, and S. L. Gilbert, Epitaxially grown AlN and its optical band gap, Journal of Applied Physics 44, 292 (1973).

95 A. V. Dobrynin, G. A. Naida, and V. A. Novoselov, Acoustoelectric parameters of aluminium nitride epitaxial layers, Physica Status Solidi (a) 104, (1987).

96 Y. Melnik, D. Tsvetkov, A. Pechnikov, I. Nikitina, N. Kuznetsov, and V. Dmitriev, Characterization of AlN/SiC Epitaxial Wafers Fabricated by Hydride Vapour Phase Epitaxy, Physica Status Solidi (a) 188, 463 (2001).

97 O. Y. Ledyaev, A. E. Cherenkov, A. E. Nikolaev, I. P. Nikitina, N. I. Kuznetsov, M. S. Dunaevski, A. N. Titkov, and V. A. Dmitriev, Properties of AlN Layers Grown on SiC Substrates in Wide Temperature Range by HVPE, Physica Status Solidi (C) 0, 474 (2003).

98 A. S. Usikov, D. Kim, A. I. Pechnikov, Y. V. Ruban, M. A. Mastro, Y. Melnik, V. A. Soukhoveev, Y. V. Shapovalova, O. V. Kovalenkov, G. H. Gainer, S. Mahajan, and V. A. Dmitriev, Material quality improvement for homoepitaxial GaN and AlN layers grown on sapphire-based templates, Physica Status Solidi (C) 0, 2580 (2003).

99 A. Nikolaev, I. Nikitina, A. Zubrilov, M. Mynbaeva, Y. Melnik, and V. Dmitriev, AlN wafers fabricated by hydride vapor phase epitaxy, Material Research Society Internet Journal on Nitride Research (1999).

100 Y. Melnik, V. Soukhoveev, V. Ivantsov, V. Sizov, A. Pechnikov, K. Tsvetkov, O. Kovalenkov, V. Dmitriev, A. Nikolaev, N. Kuznetsov, E. Silveira, and J. Freitas, AlN substrates: fabrication via vapor phase growth and characterization, Physica Status Solidi (a) 200, 22 (2003).

101 M. Albrecht, I. P. Nikitina, A. E. Nikolaev, Y. V. Melnik, V. A. Dmitriev, and H. P. Strunk, Dislocation Reduction in AlN and GaN Bulk Crystals Grown by HVPE, Physica Status Solidi (a) 176, 453 (1999).

102 X. Gong, K. Xu, J. Huang, T. Liu, G. Ren, J. Wang, and J. Zhang, Evolution of the surface morphology of AlN epitaxial film by HVPE, Journal of Crystal Growth 409, 100 (2015).

103 T. Nagashima, M. Harada, H. Yanagi, Y. Kumagai, A. Koukitu, and K. Takada, High-speed epitaxial growth of AlN above 1200 ∘ C by hydride vapor phase epitaxy, Journal of Crystal Growth 300, 42 (2007).

104 T. Nagashima, M. Harada, H. Yanagi, H. Fukuyama, Y. Kumagai, A. Koukitu, and K. Takada, Improvement of AlN crystalline quality with high epitaxial growth rates by hydride vapor phase epitaxy, Journal of Crystal Growth 305, 355 (2007).

105 M. Balaji, A. Claudel, V. Fellmann, I. Gélard, E. Blanquet, R. Boichot, A. Pierret, B. Attal-Trétout, A. Crisci, S. Coindeau, H. Roussel, D. Pique, K. Baskar, and M. Pons, Effects of AlN nucleation layers on the growth of AlN films using high temperature hydride vapor phase epitaxy, Journal of Alloys and Compounds 526, 103 (2012).

106 M. Pons, R. Boichot, N. Coudurier, A. Claudel, E. Blanquet, S. Lay, F. Mercier, and D. Pique, High temperature chemical vapor deposition of aluminum nitride, growth and evaluation, Surface and Coatings Technology 230, 111 (2013).

107 A. Claudel, V. Fellmann, I. Gélard, N. Coudurier, D. Sauvage, M. Balaji, E. Blanquet, R. Boichot, G. Beutier, S. Coindeau, A. Pierret, B. Attal-Trétout, S. Luca, A. Crisci, K. Baskar, and M. Pons, Influence of the V/III ratio in the gas phase on thin epitaxial AlN layers grown on (0001) sapphire by high temperature hydride vapor phase epitaxy, Thin Solid Films 573, 140 (2014).

108 K. Okumura, T. Nomura, H. Miyake, K. Hiramatsu, and O. Eryuu, HVPE growth of AlN on trench- patterned 6H-SiC substrates, Physica Status Solidi (C) 8, 467 (2011).

109 K. Fujita, K. Okuura, H. Miyake, K. Hiramatsu, and H. Hirayama, HVPE growth of thick AlN on trench-patterned substrate, Physica Status Solidi (C) 8, 1483 (2011).

110 D. Kamber, Y. Wu, E. Letts, S. DenBaars, J. Speck, S. Nakamura, and S. Newman, Lateral epitaxial overgrowth of aluminum nitride on patterned silicon carbide substrates by hydride vapor phase epitaxy, Applied Physics Letters 90, 122116 (2007).

111 Y. Kumagai, J. Tajima, M. Ishizuki, T. Nagashima, H. Murakami, K. Takada, and A. Koukitu, Self-Separation of a Thick AlN Layer from a Sapphire Substrate via Interfacial Voids Formed by the Decomposition of Sapphire, Applied Physics Express 1, 45003 (2008).

112 Y. Kumagai, Y. Enatsu, M. Ishizuki, Y. Kubota, J. Tajima, T. Nagashima, H. Murakami, K. Takada, and A. Koukitu, Investigation of void formation beneath thin AlN layers by decomposition of sapphire substrates for self-separation of thick AlN layers grown by HVPE, Journal of Crystal Growth 312, 2530 (2010).

113 P. Geiser, J. Jun, S. M. Kazakov, P. Wägli, J. Karpinski, B. Batlogg, and L. Klemm, AlxGa1−xN bulk single crystals, Applied Physics Letters 86, 081908 (2005).

114 M. Michimasa, T. Keisuke, S. Issei, M. Naho, and N. Hideaki, U.S. Patent No. US2011114016A1 (May 19, 2011).

115 A. Koukitu, J. Kikuchi, Y. Kangawa, and Y. Kumagai, Thermodynamic analysis of AlGaN HVPE growth, Journal of Crystal Growth 281, 47 (2005).

116 H. Murakami, J. Kikuchi, Y. Kumagai, and A. Koukitu, Thermodynamic study on the role of hydrogen during hydride vapor phase epitaxy of Alx Ga1−xN, Physica Status Solidi (C) 3, 1457 (2006).

117 A. Koukitu, F. Satoh, T. Yamane, H. Murkami, and Y. Kumagai, HVPE growth of $Al_xGa_{1-x}N$ ternary alloy using $AlCl_3$ and GaCl, Journal of Crystal Growth 305, 335 (2007).

118 H. S. Ahn, S. W. Kim, K. H. Kim, M. Yang, J. Y. Yi, H. J. Lee, H. K. Cho, C. R. Cho, T. Narita, Y. Honda, M. Yamaguchi, and N. Sawaki, Growth of thick AlGaN by mixed-source hydride vapor phase epitaxy, Applied Surface Science 243, 178 (2005).

119 K. S. Jang, K. H. Kim, S. L. Hwang, H. S. Jeon, H. S. Ahn, M. Yang, W. J. Choi, S. W. Kim, Y. Honda, M. Yamaguchi, N. Sawaki, J. Yoo, S. M. Lee, and M. Koike, Characterization of AlGaN, Te-doped GaN and Mg-doped GaN grown by hydride vapor phase epitaxy, Physica Status Solidi (C) 4, 133 (2007).

120 V. Soukhoveev, O. Kovalenkov, L. Shapovalova, V. Ivantsov, A. Usikov, V. Dmitriev, V. Davydov, and A. Smirnov, AlGaN epitaxial layers grown by HVPE on sapphire substrates, Physica Status Solidi (C) 3, 1483 (2006).

121 A. Usikov, V. Soukhoveev, L. Shapovalova, A. Syrkin, O. Kovalenkov, A. Volkova, V. Sizov, V. Ivantsov, and V. Dmitriev, New results on HVPE growth of AlN, GaN, InN and their alloys, Physica Status Solidi (C) 5, 1825 (2008).

122 S. Hagedorn, E. Richter, U. Zeimer, and M. Weyers, HVPE growth of thick Al0.45Ga0.55N layers on trench patterned sapphire substrates, Physica Status Solidi. C, 10, 355 (2013).

123 E. Richter, S. Fleischmann, D. Goran, S. Hagedorn, W. John, A. Mogilatenko, D. Prasai, U. Zeimer, M. Weyers, and G. Tränkle, Hydride Vapor-Phase Epitaxy of c-Plane AlGaN Layers on Patterned Sapphire Substrates, Journal of Elec Materi 43, 814 (2014).

124 D. R. Ketchum, and J. W. Kolis, Crystal growth of gallium nitride in supercritical ammonia, Journal of Crystal Growth 222, 431 (2001).

125 R. Dwiliński, R. Doradziński, J. Garczyński, L. Sierzputowski, J. M. Baranowski, and M. Kamińska, AMMONO method of GaN and AlN production, Diamond & Related Materials 7, 1348 (1998).

126 B. Wang, and M. J. Callahan, Transport growth of GaN crystals by the ammonothermal technique using various nutrients, Journal of Crystal Growth 291, 455 (2006).

127 T. Hashimoto, K. Fujito, F. Wu, B. A. Haskell, P. T. Fini, J. S. Speck, and S. Nakamura, Structural Characterization of Thick GaN Films Grown on Free-Standing GaN Seeds by the Ammonothermal Method Using Basic Ammonia, Japanese Journal of Applied Physics 44, (2005).

128 T. Fukuda, and D. Ehrentraut, Prospects for the ammonothermal growth of large GaN crystal, Journal of Crystal Growth 305, 304 (2007).

129 M. P. D'Evelyn, H. C. Hong, D. -. Park, H. Lu, E. Kaminsky, R. R. Melkote, P. Perlin, M. Lesczynski, S. Porowski, and R. J. Molnar, Bulk GaN crystal growth by the high-pressure ammonothermal method, Journal of Crystal Growth 300, 11 (2007).

130 R. Dwiliński, R. Doradziński, J. Garczyński, L. P. Sierzputowski, A. Puchalski, Y. Kanbara, K. Yagi, H. Minakuchi, and H. Hayashi, Excellent crystallinity of truly bulk ammonothermal GaN, Journal of Crystal Growth 310, 3911 (2008).

131 M. Bockowski, Bulk growth of gallium nitride: challenges and difficulties, Crystal Research and Technology 42, 1162 (2007).

132 B. Łucznik, B. Pastuszka, I. Grzegory, M. Boćkowski, G. Kamler, E. Litwin-Staszewska, and S. Porowski, Deposition of thick GaN layers by HVPE on the pressure grown GaN substrates, Journal of Crystal Growth 281, 38 (2005).

133 I. Grzegory, B. Lucznik, M. Bockowski, B. Pastuszka, M. Krysko, G. Kamler, G. Nowak, and S. Porowski, Growth of Bulk GaN by HVPE on Pressure Grown Seeds, Proceedings of SPIE 6121, 612107 (Feb 9, 2006).

134 R. F. Davis, A. M. Roskowski, E. A. Preble, J. S. Speck, B. Heying, J. A. Freitas, E. R. Glaser, and W. E. Carlos, Gallium nitride materials - progress, status, and potential roadblocks, Jproc 90, 993 (2002).

135 K. Motoki, T. Okahisa, S. Nakahata, N. Matsumoto, H. Kimura, H. Kasai, K. Takemoto, K. Uematsu, M. Ueno, Y. Kumagai, A. Koukitu, and H. Seki, Growth and characterization of freestanding GaN substrates, Journal of Crystal Growth 237, 912 (2002).

136 B. Lucznik, B. Pasturszka, G. Kamler, I. Grzegory, and S. Porowski, Growth of Bulk GaN Crystals by HVPE on Single Crystalline GaN Seeds, 61 (2009).

137 T. Paskova, Institute of Pure and Applied Physics Conference Series 19 (2000).

138 T. Sochacki, Z. Bryan, M. Amilusik, R. Collazo, B. Lucznik, J. L. Weyher, G. Nowak, B. Sadovyi, G. Kamler, R. Kucharski, M. Zajac, R. Doradzinski, R. Dwilinski, I.

Grzegory, M. Bockowski, and Z. Sitar, Preparation of Free-Standing GaN Substrates from Thick GaN Layers Crystallized by Hydride Vapor Phase Epitaxy on Ammonothermally Grown GaN Seeds, Applied Physics Express 6, (2013).

139 Hexatech Inc. AlN Technology Overview, (2011).

140 T. Sochacki, M. Amilusik, M. Fijalkowski, M. Iwinska, B. Lucznik, J. L. Weyher, G. Kamler, R. Kucharski, I. Grzegory, and M. Bockowski, Examination of defects and the seed's critical thickness in HVPE-GaN growth on ammonothermal GaN seed, Physica Status Solidi (B) 252, 1172 (2015).

141 S. K. Mathis, A. E. Romanov, L. F. Chen, G. E. Beltz, W. Pompe, and J. S. Speck, Modeling of Threading Dislocation Reduction in Growing GaN Layers, Physica Status Solidi (a) 179, 125 (2000).

142 D. Hanser, L. Liu, E. A. Preble, D. Thomas, and M. Williams, Growth and Fabrication of 2 inch Free-standing GaN Substrates via the Boule Growth Method, MRS Online Proceedings Library 798, (2003).

143 T. Fujimori, HVPE and Ammonothermal GaN Substrates for High Performance Devices, Plenary Talk at International Workshop on Nitride Semiconductors (October 2008).

144 T. Hino, S. Tomiya, T. Miyajima, K. Yanashima, S. Hashimoto, and M. Ikeda, Characterization of threading dislocations in GaN epitaxial layers, Applied Physics Letters 76, 3421 (2000).

145 J. L. Weyher, L. Macht, G. Kamler, J. Borysiuk, and I. Grzegory, Characterization of GaN single crystals by defect-selective etching, Physica Status Solidi (C)821 (2003).

146 Y. Taniyasu, M. Kasu, and T. Makimoto, Electrical conduction properties of n -type Si - doped AlN with high electron mobility (> 100 cm 2 V − 1 s − 1), Applied Physics Letters 85, 4672 (2004).

147 T. Schulz, K. Irmscher, M. Albrecht, C. Hartmann, J. Wollweber, and R. Fornari, n-type conductivity in sublimation-grown AlN bulk crystals, Physica Status Solidi (RRL) – Rapid Research Letters 1, 147 (2007).

148 M. Slomski, P. P. Paskov, J. H. Leach, J. F. Muth, and T. Paskova, Thermal conductivity of bulk GaN grown by HVPE: Effect of Si doping, Physica Status Solidi (B)1600713 (2017).

149 W. Götz, R. S. Kern, C. H. Chen, H. Liu, D. A. Steigerwald, and R. M. Fletcher, Hall-effect characterization of III–V nitride semiconductors for high efficiency light emitting diodes, Materials Science & Engineering B 59, 211 (1999).

150 A. Usikov, O. Kovalenkov, V. Ivantsov, V. Sukhoveev, V. Dmitriev, N. Shmidt, D. Poloskin, V. Petrov, and V. Ratnikov, P-type GaN epitaxial layers and AlGaN/GaN heterostructures with high hole concentration and mobility grown by HVPE, MRS Online Proceedings Library 831, 453 (2004).

151 J. Neugebauer, and Van de Walle, Chris G, Hydrogen in GaN: Novel Aspects of a Common Impurity, Physical Review Letters 75, 4452 (1995).

2. Thermal conductivity of nitrides

2.1. Introduction to thermal conductivity in nitrides

Since the introduction of wide-bandgap semiconductors the potential applications and commercially available products have seen large increases. One of the most properties of wide-bandgap semiconductors is their ability to permit devices that can operate at higher temperatures and voltages than those made by conventional semiconductor materials. Technologies such as variable speed drives in industrial motors, efficient inverters for converting green energy, more efficient battery recharging for electric vehicles, and lighting via LEDs are possible thanks to wide-bandgap semiconductors.[1] Due to the large power draw of these devices, Joule self-heating becomes an issue that needs to be dealt with to prevent failures and maintain optimal operation. One of the most important qualities of GaN is its relatively large thermal conductivity paired with its large breakdown field, which allows it to quickly transfer heat caused by high current flow. Despite the importance of accurate knowledge of the thermal conductivity of GaN, challenges in characterization and applications with nitrides has led to a scarcity of publications.

III-V materials and other high-k dielectrics present unique challenges to the characterization of thermal properties due to factors such as inhomogeneity, anisotropy, and thickness dependent variation. Many results on thermal conductivity of the nitrides have been widely scattered due to different processing techniques leading to microstructural variations that affect the thermal properties. Accurate reporting of the thermal properties of the nitrides

should include the samples thickness, dislocation density, dopant concentration, inhomogeneity present, and anisotropy of the samples.

The challenges in characterizing thermal conductivity are present in all materials. Measurement of thermal conductivity is much more difficult than that of electrical conductivity due to the inability to isolate heat flow at boundaries, as it is difficult to create a lossless thermal boundary. The transfer of heat between the sample and surrounding medium makes it difficult to establish boundary conditions, however heat transfer can be reduced by performing measurements in vacuum and the use of thermal insulation. Heat transfer problems can be lessened to some extent by measuring the thermal diffusivity instead of the thermal conductivity, however they cannot be completely alleviated.

The material property of thermal conductivity is very sensitive to sample specifics, such as local inhomogeneity, dislocations, and impurities which has led to differing values of thermal conductivity for the same material (with different characteristics), when reported by different groups. While this presents challenges for establishing the true quantitative values of thermal conductivity, it also demonstrates that the value of thermal conductivity can be used as a tool to qualitatively justify the structural properties of materials. The absence of reporting details on the material properties that affect the thermal conductivity in publications has led to wildly varying values in GaN with similar dislocation density, which is the parameter most often cited for justifying changes in the reported thermal conductivity. Accurate reporting would require not only the threading dislocation density, but also the point defect density, other impurity concentrations (both intentional and unintentional), and sample geometry which can affect the magnitude of the measured value depending on the

measurement technique used. The material characteristics are not the only cause of discrepancies in reported values, another factor is the extent to which experimenters satisfy the heat flow boundary conditions.[2]

2.2. Origin of the thermal conductivity of materials

It is well known that heat flows from hotter areas to colder areas, either by conduction, convection or radiation. In conduction, heat is passed through the body of a material itself. Convection involves heat being transferred by the motion of portions of a heated body. For radiation, heat is transferred spatially by electromagnetic radiation. In solid materials such as semiconductors, which are the focus of this work, the primary form of heat transfer is via conduction through the lattice. Due to lack of material diffusion, convection plays a negligible role in heat transfer and often radiation is very small compared to conduction. When discussing heat flow via conduction in solids, we typically describe the materials ability to transfer heat by its thermal conductivity.

Carslaw and Jaeger[3] describe the basis of thermal conductivity by the following hypothesis: An infinite cylinder of a solid is bounded by two parallel planes that extend to infinity. The two parallel planes are kept at constant temperatures T_0 and T_1, where $T_1 > T_0$. After a given amount of time, equilibrium is achieved and a temperature gradient is formed inside the solid. For a cross-section of the cylinder, the area A of a surface is a circle and the center points of each circle are separated by a distance d. The quantity of heat Q that flows through the surface A over t seconds once equilibrium is reached is

$$Q = \frac{K(T_1 - T_0)At}{d} \tag{2.1}$$

where K is a material constant called thermal conductivity. Equation (2.) can be rearranged to give the units for thermal conductivity

$$K = \frac{Qd}{(T_1 - T_0)At} \tag{2.2}$$

The standard unit for heat Q is the Joule, and the rate of heat transfer Q/t can be expressed in Watts. Using units of meters for length and Kelvin for temperature, the unit of thermal conductivity is Watts per meter Kelvin (W/mK).

This definition is a simplified exercise for defining thermal conductivity, and only applies to homogenous and isotropic solids. It is, however, useful in describing how the thermal conductivity of a material is characterized. In the following section, the different types of thermal conductivity characterization techniques are described. The characterization techniques are typically split into steady-state and transient categories. Steady-state characterization techniques are explained well by the previous example for defining thermal conductivity. In a steady-state technique, a solid with precise known dimensions is subjected to a given quantity of heat, and the temperature change at a known distance is measured. By doing this, a temperature change induced by a given flux of heat is measured over a length giving the thermal conductivity in W/mK. The following section gives more details on the steady state techniques as well as the alternative transient techniques.

2.3. Overview of thermal conductivity characterization techniques

Steady state techniques involve direct measurement of the thermal conductivity of the sample, while many dynamic techniques often involve extracting the thermal conductivity from the measured thermal diffusivity. While dynamic measurements allow for relatively

quick measurements in comparison to steady state techniques, accurate knowledge of both the sample specific heat and density is necessary in order to extract thermal conductivity from thermal diffusivity. Both steady-state and dynamic measurements can be used for measurements of nitrides, however each technique has specific advantages and disadvantages. Among other reasons why each type of technique would be used compared to another, steady-state is commonly used for lower temperature measurements and for larger bulk samples, while dynamic techniques are typically employed at room temperature and above.

2.3.1. Steady-state techniques

Steady-state techniques are the only type of technique where the thermal conductivity is gathered directly by measuring the heat flux needed to maintain a fixed thermal gradient in the sample. Static methods are broken down into absolute and comparative methods, where absolute involves the direct measurement of heat passing through the sample and comparative involves relating the heat flow through the sample to a standard comparison sample. Measurements are only taken once a thermal equilibrium is established, which makes steady-state techniques time consuming but relatively more accurate (+/- 5-10%). Once equilibrium is reached across a sample with well-defined dimensions, the temperature is measured at two or more points along a specified length. For the measurement of lateral conductivity, a long, uniform rectangular cross-section must be prepared of either a free-standing bulk substrate or a thin film on a substrate with low thermal conductivity. The sample is subjecting to a heater generating heat at a constant rate at one end, while the other end is thermally grounded. Careful consideration in this type of measurement is needed to

minimize the heat loss through the heater wires, measurement probes, the substrate, and to radiation and convection of the air. Due to most bulk nitride substrates and films having lengths much longer than their thicknesses, and not always having precise uniform dimensions, heat loss by radiation and convection becomes an important issue. Therefore, steady-state techniques may have uncertainties too large for accurate thermal characterization of nitrides.

2.3.2. Dynamic techniques

Dynamic techniques often involve the measurement of thermal diffusivity, which then can be related to thermal conductivity by

$$K = DC_P\rho \qquad (2.3)$$

where D is the thermal diffusivity and C_P is the specific heat per unit mass. The determination of the thermal diffusivity instead of directly measuring the thermal conductivity does not introduce much error as it is relatively simple to determine both the specific heat and the density of the sample with good accuracy.

Advantages of Dynamic Techniques. Measurements of films and substrates have most often relied on dynamic techniques due to the following advantages:

a. *Speed of data collection*. Measurements can be performed more quickly using dynamic techniques relative to steady-state techniques since the latter require time to establish thermal equilibrium across the entire sample. For example, at the speed at which equilibrium is established for an AC method, Mion[4] calculated the transient times for the 3omega method and found

$$\tau = \frac{1}{2\omega} \tag{2.4}$$

Where 2ω is the angular frequency of the thermal waves. For typical drive frequencies used in the technique varying from 10-10,000Hz, the time to reach equilibrium varies from 50-0.05ms, respectively.

b. *Radiation and convection losses.* Dynamic techniques are not as susceptible to radiation and convection losses from the large surface area of substrates and films. Cahill demonstrated that one dynamic technique, the 3ω method, is relatively insensitive to heat loss from blackbody radiation due to the relatively thin samples required for the technique.[5] When the temperature difference used to determine thermal conductivity is held constant and the characteristic length of the experimental geometry is reduced by a factor of f, the heat loss due to blackbody radiation is reduced by a factor of f^2.

c. *Small heat-affected region.* Dynamic techniques also have a smaller heat-affected region which is useful for samples with small thicknesses. Not only do smaller heat-affected regions allow measurements of thin samples, they also allow the possibility of measuring any inhomogeneity of the thermal properties of the sample by performing measurements in multiple areas on the surface.

d. *Negligible effects of DC voltage artifacts.* AC measurements are not as susceptible to impacts of 1/f noise and other low-frequency drifts such as junctions of dissimilar metals in the measurement circuitry.[6]

The dynamic thermal characterization techniques can further be broken down into time and frequency domain methods.[7] While both techniques measure the thermal diffusivity, time domain methods extract it from the time required for a heat pulse to propagate through a section of the sample and therefore are also called pulsed methods. Frequency domain techniques measure diffusivity from the propagation constants of the thermal waves in the sample and surrounding areas and are also called thermal wave methods. Since both types of dynamic methods measure the thermal diffusivity of the samples, a knowledge of heat capacity is required to obtain the thermal conductivity.

2.3.2.1. Time domain methods

Time domain techniques, as the name suggests, rely on monitoring the temperature changes of heat applied to the surface over time. Heat is applied by either Joule heating or by laser or optical pulses depending on the technique.

Time domain thermoreflectance. The most commonly used time domain technique is a type of optical pump and probe method known as time domain thermo-reflectance (TDTR). The TDTR technique uses a high power laser for heating the sample and a lower power laser for its measurement. Sampele preparation for this measurement involves deposition of a metal film on the surface. A laser pulse of ~10ns creates temperature-induced changes to the reflectivity which is detected by the lower power laser. The laser pulse creates localized heating which induces thermal stress, leading to an acoustic strain pulse. The effects of the acoustic strain pulse can then be detected by monitoring the change in reflectivity via the low power laser. TDTR has been proven useful for characterization of the thermal properties of films while being non-contact and providing high spatial and temporal (MHz) resolution.

Drawbacks of the technique are related to the high signal to noise ratio, the repeatability of the results, and the complexity and cost of the TDTR setup.[8]

Laser flash technique. In 1863, Angstrom developed the Angstrom thermal wave technique by heating one end of a metal rod periodically and measuring amplitude and phase shift of the heat wave. In a modified technique, the fluctuations in temperature as a function of time are measured by two thermistors along the rod and compared in order to extract thermal diffusivity.[9] A more modern approach is known as the laser flash technique which relies on a short pulse from a laser to heat the front face of the sample. The higher the thermal diffusivity of the sample, the faster the thermal energy wave passes through the sample and is detected by a thermometer on the back side of the sample.

2.3.2.2. Frequency domain methods

Frequency domain methods typically rely on heat generated by Joule heating, which is easily quantifiable compared to optical or external heating. Differing from the time domain techniques, samples are subjected to an AC signal and data on the thermal properties is extracted with respect to frequency.

Pyroelectric method. Pyroelectric crystals are used in the pyroelectric method to measure the diffusivity of thin films and bulk samples. The technique involves attaching a pyroelectric sensor to the sample with good thermal contact using a very thin conducting electrode on each side of the crystal. Similar to the Angstrom technique, a burst of incident radiation is used to heat one side of the sample. The thermal energy diffuses through the crystal and into the pyroelectric sensor, which produces a voltage drop between the two electrodes. The voltage across a load resistor with respect to time is monitored by an

oscilloscope and the thermal diffusivity is extracted from the shape of the voltage vs. time curve.[2]

Photoacoustic technique. The photoacoustic effect involves periodically varying radiation introduced to the sample which causes changes in the temperature of the sample. Typically, a chopped light source is used to irradiate the sample, where the light is converted to periodic heat flow. The periodic heat flow then travels to the surface of the sample and is spread into the surrounding ambient air. Changes in acoustic air pressure at the surface of the sample when confined in a small volume can be measured with a microphone. The thermal diffusivity can be extracted from the phase shift produced between the chopped light and the measured sound signal.[10]

Mirage technique. The mirage technique relies on the mirage effect, which is manifested by a generation of thermal waves in an opaque solid created by an incident laser. In the technique, a heating beam is focused on a spot on the sample surface, and a second probe laser is focused at a specified distance and height from the heated spot parallel to the surface of the sample. As the sample is heated, a periodic gradient of the air temperature profile is created, causing a change to the refractive index of the air that deflects the parallel probe laser. The probe laser is deflected both normal and transverse to the surface via a position detector and the phase and amplitude are monitored by a vector lock-in amplifier. For determination of the diffusivity, the transverse optical probe beam deflection angle is measured while the probe beam is scanned laterally across the sample at a constant height. Thermal diffusivity of many semiconductors and metals have been demonstrated by Kuo using this method.[11]

3ω method. The 3ω technique is a frequency domain dynamic method that relies on Joule heating from a thin metal wire deposited onto the surface of the sample. In this technique, a low frequency signal is passed through the metal wire which is used as both the heater and the thermometer for the measurements. The signal at frequency ω generates Joule heating at a resistance of 2ω, which in turn generates a voltage at 3ω that is used to extract data on the thermal conductivity. Differing from most other dynamic techniques, the thermal conductivity is directly measured instead of the diffusivity. Advantages of this technique include low heat loss due to radiation and convection, relatively inexpensive and simple set-up, quick measurement time, and the ability to measure both thin films and bulk structures at a variety of depths in the sample.

A key disadvantage of this technique is related to the difficulty of measuring conductive samples, as an extra processing step is needed for the addition of an insulating layer to be deposited onto the surface of the sample. The 3ω technique has been used extensively for measurements on GaN, and the setup used in this work was previously used by Mion for his measurements on bulk Fe-doped GaN.[4] Due to the advantages for the samples used in this work and the availability of the instrument, the 3ω method was used for thermal characterization of all samples in this work. The following section will describe the basics of the technique, the experimental procedure, and the device design and optimization for the high thermal conductivity bulk samples used in this work.

2.4. The 3ω method

Like all other thermal conductivity characterization methods, a heat source and a thermometer are necessary for the measurements. In the case of the 3ω technique, a thin

metal line performs both tasks. To understand how the thermal conductivity is extracted from the data measured by the thermometer, it is necessary to understand both how heat is evolved from a line source heater on a semi-infinite medium and how the temperature fluctuations are detected.

2.4.1. Equation for a line source heater on an infinite half-solid

From a heat distribution point of view, the 3ω technique is similar to the hot-wire technique as it involves radial heat flow from a line source heat element, while the main difference is related to the frequency dependence of temperature oscillations that are taken into account instead of the time domain response. The radial heat flow from the line source heater is illustrated in *Figure 2.1*, where the oscillations are at a distance $r = (x^2 + y^2)^{1/2}$ from

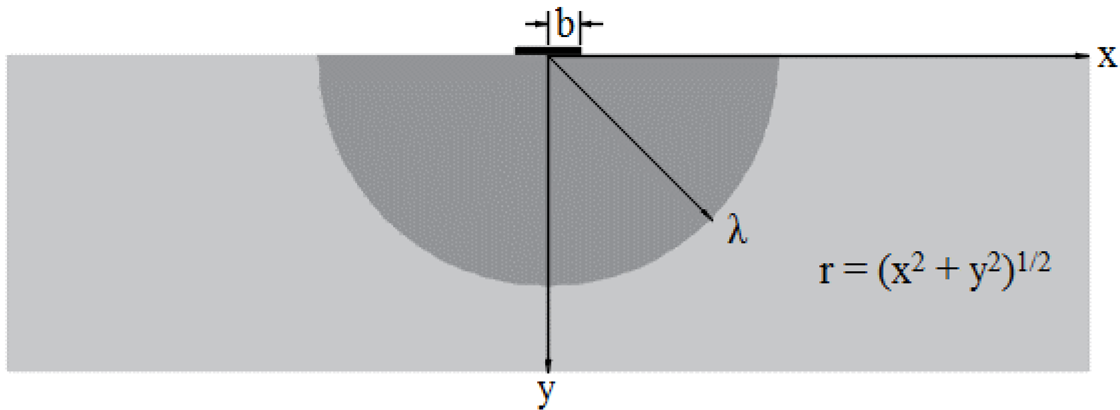

Figure 2.1 *Schematic illustration of a line heater with half width b on the cross section of an infinite half solid to demonstrate radial heat flow at depth λ.*

the center of the heater. In the case of an infinitely narrow line heat source on an infinite half-solid, the line half-width b = 0 and the sample thickness y = ∞. The solution for the temperature oscillations ΔT(r) was found by Carslaw and Jaeger[3] to be

$$\Delta T(r) = \frac{P}{\pi l}\frac{1}{k_{th}}K_0\left(\frac{r}{\lambda}\right) \tag{2.5}$$

where k is the thermal conductivity, P is the power generated at frequency 2ω in the line source, l is the length of the line, K_0 is the zeroth order modified Bessel function, and λ is thermal penetration depth. The thermal penetration depth is related to the angular frequency ω of the current in the line, the half-volumes density ρ and the specific heat C_P by

$$\lambda = \left(\frac{k_{th}}{2\omega\rho C_P}\right)^{1/2} \tag{2.6}$$

The factor of 2 in the denominator is due to the current at ω heating the line at 2ω due to Joule heating caused by the non-zero temperature coefficient of resistivity α_T. Mathematically, the factor of 2 is generated due to the current being squared in the equation for time-dependent power. Imposing the limit that the position must be much less than the penetration depth such that $\left|\frac{r}{\lambda}\right| \ll 1$, Equation **Error! Reference source not found.**) is a pproximated as:[12]

$$\Delta T = \frac{P}{\pi lk}\left(\frac{1}{2}\ln\frac{D}{r^2} - 0.2256 - \frac{1}{2}\ln\omega - \frac{i\pi}{4}\right) \geq 0 \tag{2.7}$$

It can be seen that Equation **Error! Reference source not found.**) is separated the t emperature oscillations into a real and an imaginary part.

2.4.2. Physics of the 3ω method

The thin metal line deposited onto the surface of the sample used in the 3omega method has a resistance R_0 defined by its intrinsic resistivity and dimensions. When an AC current

$$I(t) = I_0 \cos \omega t \tag{2.8}$$

is passed across the line with an angular frequency ω, the finite resistance of the metal line has the effect of generating heat due to resistive heating. Due to the Joule effect, this heat takes the form of thermal waves which propagate at frequency of 2ω, creating temperature fluctuations given by

$$\Delta T = \Delta T_0 \cos(2\omega t + \theta) \tag{2.9}$$

where θ is the phase. The metal line has a finite temperature coefficient of resistance, α_{TCR}, so its resistance changes with temperature given by

$$R = R_0(1 + \alpha_{TCR} \Delta T) \tag{2.10}$$

Physically, the electron current in the metal line encounters resistance from the ions of the lattice by transferring energy in the form of elastic collisions. Collisions of the electrons with the lattice has the effect of transferring kinetic energy into thermal energy in the form of phonons. The phonons move as thermal waves throughout the lattice until they reach a boundary. In the case of the infinite half volume, no heat is lost at the boundary of the surface which would normally be air or vacuum. All phonons will move into the direction of the sample where they will encounter the boundary with the sample or any layers in between the sample and metal line. It is assumed that the thermal boundary resistance is zero

in this analysis. As can be seen in Equation **Error! Reference source not found.**), thermal w aves travel further into samples with higher thermal conductivity. With the heat traveling further into the sample for higher thermal conductivity samples, the magnitude of the temperature fluctuations ΔT at the metal line are smaller. The physical information on the thermal conductivity of the sample is contained in these temperature fluctuations, however it is not possible to measure them directly. Fortunately, due to the metal line being both a heater and a thermometer, the magnitude of the thermal fluctuations can be measured indirectly by measuring the voltage drop across the line.

Given that the thermal waves in Equation **Error! Reference source not found.**) are t ime-dependent due to Joule heating, the resistance in Equation **Error! Reference source not found.**) becomes time-dependent in the form

$$R(t) = R_0(1 + \alpha_{TCR}\Delta T_0\cos(2\omega t + \theta)) \tag{2.1}$$

By Ohm's law, the voltage across the line is simply

$$V(t) = I(t)R(t) \tag{2.2}$$

Therefore, combining Equations **Error! Reference source not found.**) and **Error! Re ference source not found.**) and applying a cosine product identity gives

$$V(t) = I_0R_0\cos(\omega t) + \frac{1}{2}\alpha_{TCR}I_0R_0\Delta T_0\cos(\omega t + \theta) + \frac{1}{2}\alpha_{TCR}I_0R_0\Delta T_0\cos(3\omega t + \theta) \tag{2.3}$$

As discussed previously, the key to the measurement is finding the value of the temperature fluctuations in order to determine thermal conductivity. From Equation (2.3), the first term is simply the DC offset at the drive frequency ω, which gives no information about ΔT_0. The

second term contains ΔT_0, however it cannot be extracted due to the term being dependent on the same frequency as the first term. The last term is the one of interest and the origin of the name of the 3ω technique. Through the use of a lock-in amplifier, the magnitude of the last term in Equation (2.3) can be extracted and the temperature fluctuations can be solved for. The last term can be expressed as the voltage at three times the drive frequency ω, or the third harmonic voltage

$$V_{3\omega} = \frac{1}{2} \mathrm{V}_{1\omega} \alpha_{TCR} \Delta T_0 \cos(\omega t + \theta) \tag{2.4}$$

where $V_{1\omega}$ is the voltage across the line at the principal drive frequency. Equation (2.4) is complex and contains a component of the temperature oscillations that are in-phase and out of phase with the drive frequency. In his pioneering paper on the 3ω method,[12] Cahill determined that the thermal conductivity could be determined by either the in-phase or out of phase component, however he found the in-phase oscillations to give a more reliable result. Separating the real part gives the magnitude of the temperature oscillations in-phase with the drive frequency and Equation **Error! Reference source not found.**) becomes

$$\Delta T_{in} = \frac{P}{2\pi lk} \left(\ln \frac{D}{r^2} - 0.2256 - \ln(\omega) \right) \tag{2.5}$$

Equation (2.5) relates the thermal conductivity of the material lying underneath a metal/heater sensor to the real component of the temperature oscillations. Upon examination, Equation (2.5) can be placed into a linear form such that ΔT_{in} is linearly dependent on ln(ω) by

$$\Delta T_{in} = -\frac{P}{2\pi lk} \ln \omega + C \tag{2.6}$$

where C is a constant that independent of ω. Equation (2.6) is the basis of the slope method, whose nomenclature stems from the fact that the thermal conductivity is contained in the slope of the linear equation.

2.4.3. The slope 3ω method

The slope method is an extension of the 3omega technique that allows for a simplified determination of the thermal conductivity when a set of boundary conditions are met based on the sample properties, sample geometry, heater/thermometer geometry, and the frequency of the input signal. This section begins the procedure for conducting the slope method measurement and ends with a discussion of the boundary conditions that must be met for error-free thermal conductivity determination.

2.4.3.1. Measurement procedure

In the slope method, the third harmonic voltage is plotted against the angular frequency of the first harmonic signal and the slope of the trend is taken. Assuming boundary conditions are met, the function of $V_{3\omega}$ vs $\ln(\omega)$ provides a linear trend from which the thermal conductivity can be extracted. A typical slope method measurement entails the following steps:

Pre-evaluation of boundary conditions. Boundary conditions relating to the penetration depth of the waves are examined, namely the frequency range used needs to be compatible with samples and metal heater/thermometer dimensions.

Equipment setup. Matching the resistance of the reference resistor with the resistance of the metal heater thermometer. The resistance of the heater R_h and the reference are recorded from this and used in the slope method calculation.

Input parameters. The first harmonic voltage $V_{1\omega}$ is set from the RMS input voltage V_{RMS} and recorded along with the input power into the heater $P_h = V_{1\omega}*I_{1\omega}$ for input in the equation.

Data collection. $V_{3\omega}$ is measured as a function of frequency and plotted over a range from 50Hz – 10,000Hz.

Slope method calculation. The thermal conductivity is extracted from the slope of $V_{3\omega}$ vs. ln(ω), $V_{1\omega}$, R_h, α_{TCR}, P, and heater length l using the slope method equation. An arbitrary value for the temperature coefficient of resistivity α_T of the metal used for the heater is used for the first measurement until multiple measurements are performed at different temperatures to determine the true value, as discussed in the next section. In the determination of thermal conductivity, $V_{3\omega}$ is related to the normalized fluctuations in the sample by

$$\Delta T_{in} = \frac{2V_{3\omega}}{V_{1\omega}\alpha_{TCR}} \tag{2.7}$$

Then the slope of ΔT_{in} vs. ln(ω) is taken and the thermal conductivity is determined by

$$K = -\frac{P}{2\pi l}\left(\frac{d(\Delta T)}{d(\ln(\omega))}\right)^{-1} \tag{2.8}$$

2.4.3.2. Penetration depth and corresponding boundary conditions

While the procedure for calculating the thermal conductivity with the slope method is straightforward, the measured value can be highly erroneous if the boundary conditions are not precisely met. The penetration depth in Equation **Error! Reference source not found.**) i s an important parameter as it determines the depth at which the waves penetrate and therefore the depth at which the thermal conductivity of the sample is sourced from. The

depth of the thermal waves impose boundary conditions on the slope method that must be obeyed in order to get a linear response of the normalized thermal oscillations (and therefore 3ω) with respect to the logarithm of angular frequency. Due to all parameters in the penetration depth calculation being fixed other than angular frequency, the angular frequency determines the depth at which the thermal waves penetrate in the sample. After quick analysis, one can see the thermal waves are ultimately limited by the thickness of the sample, and therefore the range of measurable frequencies is limited.

For a hypothetical undoped GaN sample with thermal conductivity k = 250 W/mK, C_P = 490 J/kgK and a density of 6150 kg/m^3, the penetration depth would be 363μm to 26μm for frequencies of 50 to 10,000Hz, respectively. For this hypothetical sample, it can be seen that a thickness over 363μm would be required in the low frequency regime. However this is the best-case scenario, and the boundary conditions impose tighter restrictions than this maximum limit due to thermal reflections of interfaces, as discussed below. The penetration depth provides insight into the challenges of measuring high thermal conductivity samples and/or very thin films. As the thermal conductivity of the sample becomes large, such as in high quality undoped GaN, AlN, and diamond the thermal waves are able to penetrate further at all frequencies and it becomes difficult to find a linear region using the slope method. The boundary conditions related to the penetration depth, sample dimensions, and heater dimensions are discussed in the following section.

The boundary conditions of the slope method are dependent on the sample thickness, the gold heater width, and the penetration depth of the thermal waves. The slope method is rendered invalid and will have a non-linear $V_{3\omega}$ vs. ln(ω) response if all boundary conditions

are not met. The following assumptions for the slope method are limit the boundary conditions:[13]

Infinite thickness. The simplified slope method works assuming the sample is infinite and homogenous to thermal waves. As previously discussed, the finite sample thickness imposes a boundary to the thermal waves, so d > λ. Borca-Tasciuc concluded in his work that the penetration depth must be five times smaller than the thickness of the substrate for the error to be less than 1%.[13] For a sample with fixed width, this imposes a low frequency limit on the measurement. For the example posed in *Figure 2.2*, if the sample

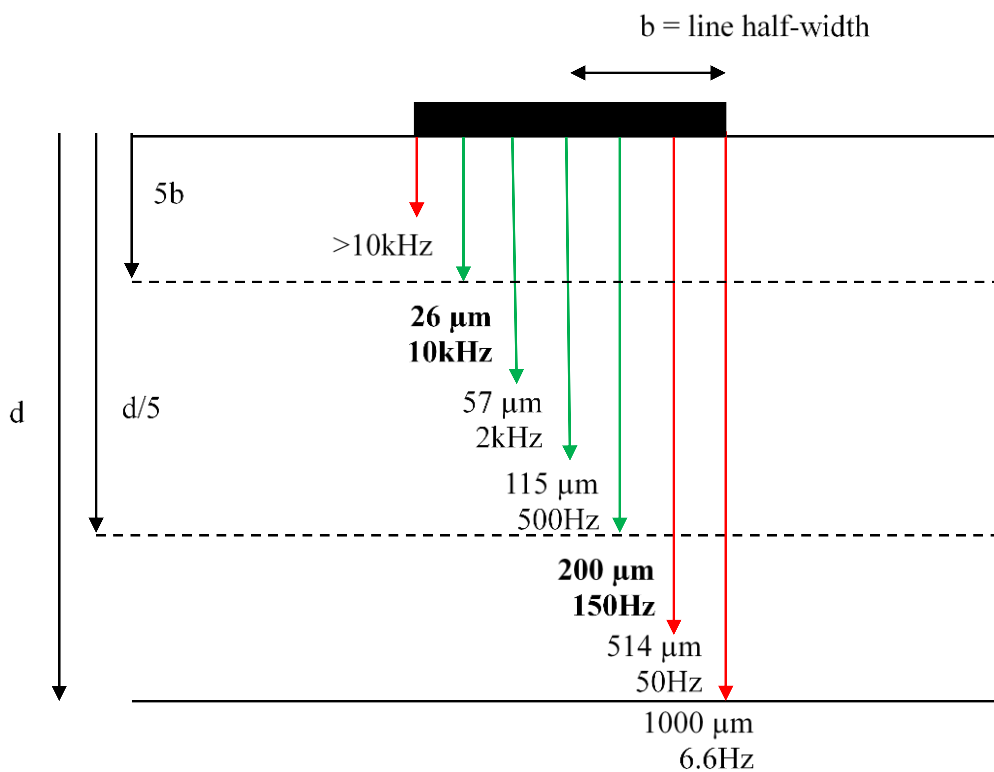

Figure 2.2 *Illustration of the frequency dependence of penetration depth for a sample with thickness d=1mm, heater half-width b=5µm, k = 250 W/mK, C_P = 490 J/kgK and a density of 6150 kg/m^3. Frequencies with penetration depths falling in between the dashed lines can be used to determine thermal conductivity with less than 1% error.*

thickness is d = 1mm, then the maximum allowable penetration depth for less than 1% error is 200µm, corresponding to a minimum frequency of 150Hz.

Line source heater. It is assumed in the slope method that the penetration depth is much larger than the heater width and therefore the heater can be approximated as a line source. In the case where heater penetration depth approaches the heater half width, $\lambda \sim b$, the line source approximation is no longer valid and the heat source is instead planar, invalidating the slope method. Borca-Tasciuc describes a parameter z relating the heater half width, penetration depth, and substrate anisotropy K_{xy} by the equation:[13]

$$z = \frac{b}{\lambda\sqrt{k_{xy}}} \tag{2.9}$$

For an isotropic sample, z is simply a ratio of the heater half width and the penetration depth. It was found that for the line source approximation to be valid within 1% error, $z < 0.2$ or the penetration depth must be 5 times greater than the heater half width. For a typical line heater width of 10µm, the penetration depth would have to be at least 25µm for less than 1% error. In the example illustrated in *Figure 2.2*, this would impose a upper limit on the frequency at 10,000Hz.

Infinitely thin heater with zero heat capacity. The slope method relies on the heat equation developed in section 2.4.1 which also assumes that the heater is a line source, i.e. it is infinitely thin and has no specific heat. However, in actual measurements, this of course is not possible. Due to the typical heater width of 4-10µm and thickness of 200nm, the heater obviously has finite thickness and heat capacity. The effect of this on the measurements is in

limiting the upper frequency limit of the measurements. Borca-Tasciuc has outlined the errors involved with assuming a line source heater at high frequencies.[13]

2.4.4. The differential 3ω method

Discussions thus far on the slope method have been limited to measurements of thermal conductivity on bulk substrates. However, applications involving semiconductors often involve thin films of much smaller thickness than bulk substrates. Due to growth process of nitrides and other semiconductors, many material properties vary with thickness of the sample. As discussed in Chapter 1, the growth of thin films heteroepitaxially on foreign substrates leads to lattice mismatch that causes generation of structural defects. The typical defect found in the nitrides grown heteroepitaxially is dislocations that often penetrate the entire film and terminate at the surface. As film thickness is increased, some dislocations annihilate each other, leading to a less defective lattice. Due to the nature of heat conduction in semiconductors, these threading dislocations decrease the thermal conductivity by scattering phonons. It is therefore important to be able to determine the thermal conductivity of these thin films, which will have different values than for their bulk counterparts. While the focus of this dissertation is on bulk III-nitrides and other wideband semiconductors, there is particular interest in thin films of ternary alloys for HEMT and optical applications. The focus of these ternary alloys is AlGaN layers, and can be found in Chapter 5. To measure the thermal conductivity of these films, a modification of the 3omega method known as the differential technique is used.

2.4.4.1. Fundamentals of the differential method

The principle of the differential technique is fairly simple, however the practical execution has its challenges. A thin film with thickness d_F and thermal conductivity k_F on a substrate with thickness d_S and thermal conductivity k_S can be seen in the schematic drawing in *Figure 2.3.* A heater/thermometer device deposited onto the surface with a width of 2b is

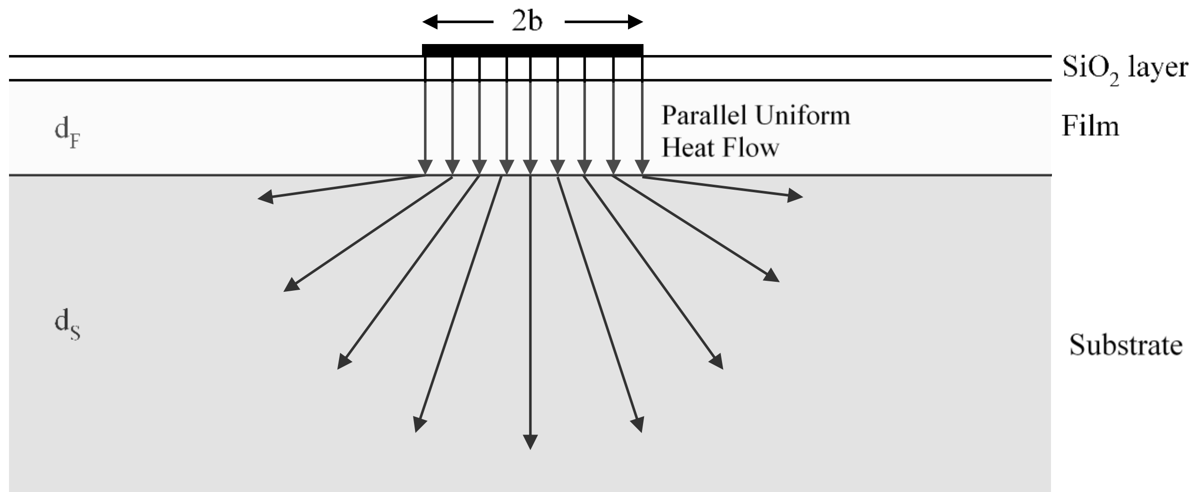

Figure 2.3 *Schematic drawing of the film with thickness d_F on a substrate of thickness d_S to illustrate parallel uniform heat flow of heat waves when 1D heat flow conditions are met for the differential method.*

used for generating thermal waves and measuring temperature fluctuations identical to the slope method. However, due to the limited dimensions of the film on the substrate, some finite thermal boundary resistance exists that disrupts the flow of heat into the substrate. The finite thermal boundary resistance is an important parameter in the differential method, and is what is used to determine the thermal conductivity of the film. If two identical metal

heater/thermometers were placed onto the surface of a bare substrate, and also onto film on an identical substrate, the measured third harmonic voltage $V_{3\omega}$ would be different for each sample. The presence of the thin film creates a disruption of the heat waves and therefore the measured temperature oscillations become a combination of the temperature oscillations in the film and the substrate combined. Written explicitly, the temperature fluctuations for the film on substrate are

$$\Delta T_{F+S} = \Delta T_F + \Delta T_S \tag{2.10}$$

Where ΔT_F is the temperature fluctuations in the film and ΔT_S is the fluctuations in the substrate, which is identical to Equation (2.7) used for the slope method (when using in-phase signal). For the case (boundary conditions discussed in next section) where heat flow is assumed to be one dimensional (1D) through the thin film, the temperature oscillations in the film are[5]

$$\Delta T_F = \frac{P}{K_F}\frac{d_F}{2bl} \tag{2.11}$$

Once the thermal fluctuations in the film are found by Equation (2.16), the thermal conductivity of the film K_F can be solved for since the line dimensions, input power, and film thickness are known.

The samples measured using the differential method in this work, namely AlGaN films on GaN substrates (Chapter 5) can be measured using the 1D differential method, however some modifications are needed to measure the samples outside the boundary conditions. Therefore, the following section describes the implementation of 1D case and the boundary conditions to be fulfilled in order to use it. Discussions on extensions to the

differential method to validate it for 2D heat flow cases, anisotropy, and multilayer stacks have been covered in the literature[4,13] and are not presented here.

2.4.4.2. Measurement procedure

The procedure for the differential measurement using the 1D heat flow case shares many common steps as for the slope method.

Processing of samples. In the differential method, a film on a substrate is measured in order to deduce the thermal conductivity of the film. Similar to the slope method, a metal heater must be deposited onto the surface of the film on substrate. An identical metal heater (identical length, width, thickness, temperature coefficient of resistivity) must be deposited onto a bare substrate that is identical to the substrate that the film was grown on.

Pre-evaluation of boundary conditions. Boundary conditions relating to the penetration depth of the waves are examined in a similar way as for the slope method – penetration depth must be less than the combined film and substrate thickness, but also deep enough to penetrate through film and into substrate. The selected frequency range needs to ensure linear trends for both the film on substrate sample and the bare substrate. Furthermore, several additional boundary conditions must be fulfilled for the differential method, as discussed in the next section.

Measurement. Matching the resistance of the reference resistor with the resistance of the metal heater thermometer. The resistance of the heater R_h and reference are recorded for the heaters on both samples.

Input parameters. The first harmonic voltage $V_{1\omega}$ is set from the RMS input voltage V_{RMS} and recorded along with the input power into the heater $P_h = V_{1\omega}*I_{1\omega}$ for input in the

equation. In the differential calculation, the power P_h for the heater atop the film on substrate and the bare substrate must be identical. If both line dimensions and properties are identical, the powers in the lines are identical. If powers are significantly different in each line at a given RMS input voltage, it is required to redeposit devices to get identical lines.

Data collection. $V_{3\omega}$ is measured as a function of frequency and plotted over a range from 50Hz – 10,000Hz for each samples. $V_{3\omega}$ must be measured at identical frequencies for each sample. Data is only recorded in the linear region, identical to slope method.

Calculation of ΔT_F. Values of $V_{3\omega}$ at a given frequency measured in the substrate are subtracted from $V_{3\omega}$ measured in the film on substrate for the same frequency. This subtraction is conducted for $V_{3\omega}$ at all frequencies and the average is taken; ideally the difference in $V_{3\omega}$ at each frequency should be the same, but measurement error can lead to small changes in the difference over the frequency range and therefore an average is taken. Similar to the slope method, the temperature fluctuations in the film are extracted from the voltage drop in the film $V_{3\omega,F}$ by Equation (2.7).

Differential calculation. With the temperature fluctuations in the film known, the thermal conductivity of the film can be calculated by Equation (2.16). Film thickness and heater dimensions must be known with high accuracy prior to the measurement.

Data adjustment. Since the differential technique assumes 1D heat flow in the film, any heat spreading (2D heat flow) in the film introduces error into the determination of thermal conductivity. Borca-Tasciuc[13] and others have performed calculations and formulated an equation that accounts for heat spreading in the film and adjusts the calculated

thermal conductivity. In the next section, this equation and the boundary conditions involved are introduced.

2.4.4.3. Boundary conditions

All analysis of the differential method discussed thus far has been for the simplified case of 1D heat flow through a film on substrate as seen in *Figure 2.3*. In order to assume 1D heat flow, the boundary conditions must be met based on film to substrate thermal conductivity contrast, line width to film thickness contrast, and anisotropy in the film.

Film to substrate thermal conductivity contrast. In order to obtain 1D heat flow through the film, the film thermal conductivity must be much less than that of the substrate, such that $K_F << K_S$. In the limiting case where $K_S = K_F$, the temperature drop across the film ΔT_F is 0. While this boundary condition does not provide a very quantitative means for how much larger K_F needs to be than K_S, Borca-Tasciuc introduced a parameter C to account for film to substrate thermal conductivity contrast which is given as[13]

$$C = 1 - \frac{K_{Fx} K_{Fy}}{K_S^2} \tag{2.12}$$

Where K_{Fx} is the thermal conductivity of the film in the in-plane (surface, perpendicular to heater line length) direction and K_{Fy} is the thermal conductivity in the cross-plane (perpendicular to surface of film, through film) direction. As can be seen from Equation (2.17), the parameter C accounts for both film to substrate thermal conductivity ratio and for anisotropy in the film. For the case of an isotropic film, Equation (2.17) simply becomes $C = 1 - K_F/K_S$.

Line width to film thickness contrast. The second boundary condition to prevent heat spreading in the film for the 1D case is that the film thickness must be much less than the half width of the line, such that $d_F << b$. This once again only provides a qualitative means to attempt to satisfy the boundary conditions, therefore Borca-Tasciuc introduced another parameter[13]

$$S = \frac{2}{\pi}\int_0^{\infty} \frac{\sin\gamma}{\gamma^3} \frac{\tanh(\gamma\beta_F)}{\beta_F\left[1 + \frac{\sqrt{K_{Fx}K_{Fy}}}{K_S}\tanh(\gamma\beta_F)\right]} d\gamma \tag{2.13}$$

where

$$\beta_F = \sqrt{\frac{K_{Fx}}{K_{Fy}}}\frac{d_F}{b} \tag{2.14}$$

Equation (2.18) accounts for film to substrate thermal conductivity contrast and film thermal conductivity anisotropy, however it is primarily affected by line width to film thickness contrast through β_F given in Equation (2.14).

The factors of C and S are used to adjust the thermal conductivity calculated under the 1D ($K_{F,1D}$) assumption so that the true cross-plane thermal conductivity K_{Fy} can be found by[13]

$$K_{Fy} = K_{F,1D}CS \tag{2.15}$$

For the boundary conditions in the 1D heat flow case to be completely fulfilled, $\beta_F \rightarrow 0$ and $K_{Fx}K_{Fy}/K_S^2 \rightarrow 0$. In this case, CS = 1 and $K_{Fy} = K_{F,1D}$. However, it is never possible to truly prevent heat spreading in the film, as it is not possible to have a substrate with infinite thermal conductivity or infinitely wide line. Therefore, in all practical situations where there

is some finite heat spreading in the field, CS < 1 and the real thermal conductivity is less than calculated by the differential method. In summary, all differential calculations assuming 1D heat flow through a film overestimate the true thermal conductivity and must be adjusted using Equations (2.13)-(2.15).

2.4.5. Sample and device processing for the 3ω method

While the 3 omega technique benefits from being a relatively simple thermal characterization method, the device processing prior to growth can be a lengthy and fragile process. Following the sample growth, it is required that samples have a relatively flat surface, with minimal surface defects and texture. For polished samples this is not an issue, but in some cases the polishing process of the bulk material could induce subsurface damage such as defects that may have the effect of lowering the maximum thermal conductivity value. The use of bulk samples usually involves the selection of the samples with the best surface quality and no surface defects. Other considerations that are discussed in more detail later are the growth of an isolation layer on the surface of conductive samples to separate it from the heater/thermometer and to prevent shorting through the sample. The entire process of device preparation usually goes through the following steps: 1) Cleaning, 2) isolation layer deposition, 3) cleaning, 4) photolithography of device mask, 5) plasma clean, 6) metal heater/thermometer deposition, 7) lift-off, 8) cleaning, 9) indium dot deposition, and 10) optical microscopy measurement/verification.

2.4.5.1. Cleaning

The most crucial aspect to a successful heater device is the thorough attention to the cleanliness of the sample. Cleaning procedures are performed at many stages of the

experiment to ensure strong bonding of the metal device to the surface. Improper cleaning leads to poorly attached devices, which can have non-uniform widths throughout their length, alternate compounds being formed other than pure metal heater material, or complete delamination or cracking during the lift-off procedure. The cleaning procedure includes mechanical, chemical (sonication), and plasma cleaning depending on the stage of the device processing procedure.

Initial cleaning procedure upon receiving the samples from growth includes a removal of any oils by soaking the samples in a bath of trichloroethylene followed by a rinse of 50/50 HCl/Deionized H_2O. After rinsing with deionized water and dried, the samples are sonicated in an acetone bath for 5 minutes. Following this procedure, samples are typically placed in a heated acetone bath right below boiling for 5 minutes and then transferred to a similar methanol bath for 5 minutes. The samples are then dried with N_2 and placed on a hotplate for 5 minutes in order to allow the complete evaporation of cleaning agents.

Prior to isolation layer deposition, samples typically undergo a short 60 second O_2 plasma reactive ion etch (RIE). The O_2 plasma etch is used in multiple stages in processing, most notably after the lithography process and prior to indium dot deposition. The use of the O_2 plasma after the lithography process has proven to provide much better contacts by removing any small surface residue from the areas that the mask etched away. While the O_2 plasma etches everywhere on the surface of the sample, the short etch time ensures that any residue in areas where the photoresist is removed while areas where there is photoresist are only etched at a negligible fraction of the total thickness. The removal of any surface residue creates a very clean surface for the bonding of the metal heater/thermometer to the SiO_2

isolation layer. The final O_2 plasma etch occurs once lift-off has been completed to remove any traces of photoresist from solution, therefore providing the indium dots a clean surface when pressed on to minimize contact resistance.

2.4.5.2. Isolation layer

Samples of GaN that are intentionally and unintentionally doped require the addition of an insulating layer in between the heater and the surface due to their conductive nature. Insulation layers that have been reported in the literature for 3 omega methods on GaN include SiO_2, Si_3N_4, and Al_2O_3.[14] In this work, PECVD was used to grow SiO_2 insulation layers given the proven reliability from previous studies[4] on the electrical isolation of GaN films.

The low thermal conductivities of the insulating layer materials contribute to a thermal barrier resistance in the measurement that needs to be evaluated. Thermal conductivities of the layers are reported around 1.28 W/mK for SiO_2, 1.23 W/mK for Si_3N_4, and 12-40 W/mK for Al_2O_3.[14] A lower thermal conductivity layer in between the heater and the high thermal conductivity sample creates a resistance to the heat flow that changes the magnitude of the resulting third harmonic voltage measured during the experiment. It is necessary when conducting a measurement to evaluate whether this interfacial resistance is negligible to the measurement or whether it needs to be accounted for. Beaudhuin[14] has reported that the interfacial resistance of both SiO2 and Si_3N_4 is 3.10×10^{-8} m^2KW^{-1}. From this interfacial resistance, it is observed that increasing the layer thickness leads to increasing thermal boundary resistance. Mion has presented a thorough investigation of the effect of thermal boundary resistance for thin layers of low thermal conductivity on layers on

substrates of low thermal conductivity.[4] For the bulk GaN samples measured in his work, he found that this thermal boundary resistance simply gives a shift in magnitude of the temperature fluctuations of $\Delta T/P$ and does not change the slope of $\Delta T/P$ vs. $\ln(\omega)$ used to determine thermal conductivity. The presence of the thin thermally resistive SiO_2 layer does not provide a frequency dependent shift in $\Delta T/P$ and therefore does not change the measured thermal conductivity.

Measurements of undoped GaN with film thicknesses ranging from 100nm to 200nm showed no significant change to the value of thermal conductivity for reference samples in our tests. An optimal insulation layer thickness of 150nm was used due to its ability to provide an acceptable minimum level of noise while keeping the layer thickness as low as possible. Due to the reasons listed above, no contribution of the thermal boundary resistance will be included in the determination of thermal conductivity.

2.4.5.3. Photolithography

After the growth of the SiO_2 insulation layer, the heater/thermometer devices needed to be patterned onto the surface. UV photolithography with a negative photoresist AZ5214E was used with a mask to pattern the devices. The mask used included an array of heater/thermometer line widths and lengths as can be seen in *Figure 2.4*. The purpose of including a variety of line widths and thicknesses on the mask is to allow for devices that satisfy the boundary conditions of a wide variety of samples with different material properties. Typical photolithography procedure includes: 1) AZ5214E photoresist was spun onto samples to obtain uniform resist thickness across sample surface, 2) photoresist was pre-baked at 90°C for 2 minutes, 3) the mask in *Figure 2.4* was positioned using an aligner and

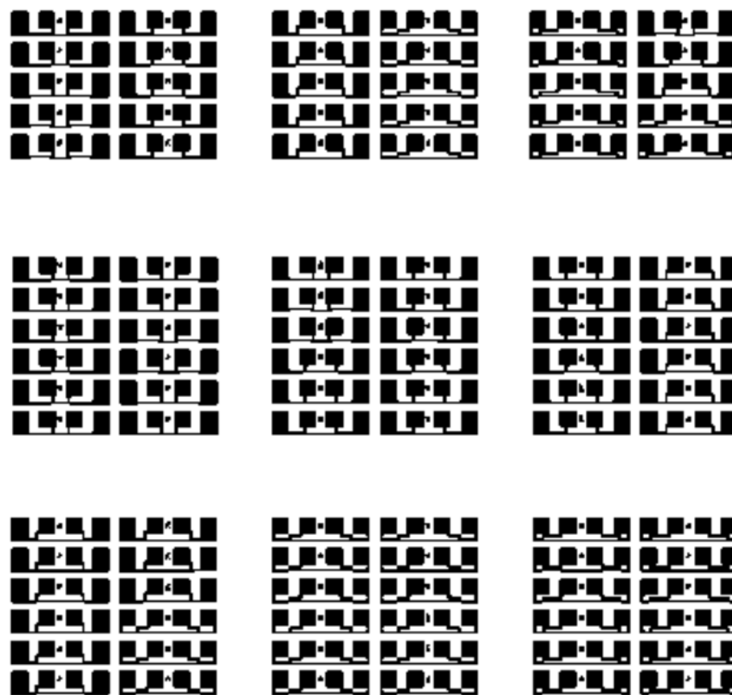

Figure 2.4 *Mask used for patterning of heater/thermometers with varying line lengths and widths for the 3ω method.*

then the samples were exposed for 3 seconds to I-line UV radiation, 4) samples were baked for 90 seconds at 115°C, 5) samples were flood exposed to UV radiation for 90 seconds without mask, 6) and finally photoresist was developed using MF-319 developing solution. Widths of valleys in negative photoresist were measured using optical microscopy prior to metallization to ensure proper development time of the photoresist.

2.4.5.4. Heater/thermometer deposition

Electron beam deposition via an Edwards Auto306 Magnetron Sputterer was used to metallize the devices patterned using photolithography. Devices were attached to a sample

holder that was inserted upside down into the chamber. Typically, the chamber was pumped down to 5 x 10^{-5} Torr prior to starting any deposition to ensure high quality film growth. A buffer layer consisting of 5nm of Ni was deposited prior to the final Au deposition to promote adhesion to the SiO_2 layer. Typical Au thicknesses ranging from 150-200nm were found to provide the best contacts while keeping the heat capacity of the device minimal. Layer thicknesses were tracked using a sensing crystal in the chamber which provided information on when the run was completed. The device specifications are described in the following sections.

Materials for the heater device are selected based on their temperature coefficient of resistivity, cost, and their inertness. Provided that the material is fairly inert and cheap, the most important parameter is the temperature coefficient of resistivity as it will determine the magnitude to of the measured third harmonic voltage. Metals with high temperature coefficients of resistivity provide the largest third harmonic voltage, which is very valuable since the third harmonic voltage is typically 3 orders of magnitude smaller than the first harmonic. The most commonly used metals are Pt and Au, due to their high temperature coefficient of resistivity and their inertness. It has been recently reported by Lama that the use of Molybdenum for the heater material can result in a 22% increase in the voltage signal due to its increased temperature coefficient of resistivity.[15]

2.4.6. Experimental details for the 3ω method

2.4.6.1. Equipment setup

Once the relatively time-consuming process of preparation of the heater/thermometer devices is complete, the measurements on the samples can be conducted. As discussed earlier

in the chapter, a sinusoidal current must be passed across the heater line at a frequency of ω and a voltage at 3ω must be measured to use the slope method. In this work, a built-in function generator as seen in *Figure 2.5* is used to provide a current with variable ω across

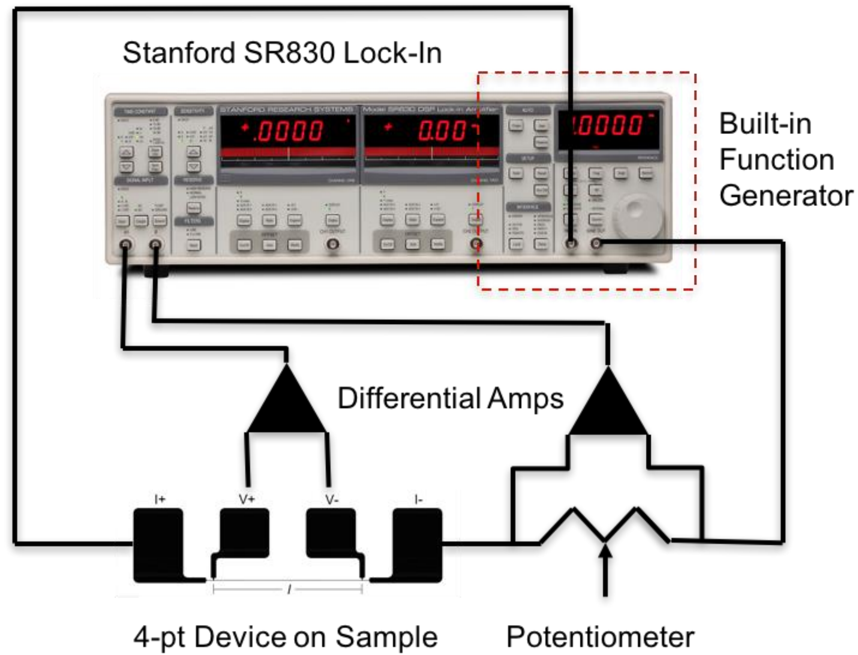

Figure 2.5 *Diagram of experimental setup and circuit used in the 3ω method.*

the I+/- contact pads. In the theoretical discussion earlier in the chapter, thermal conductivity is simply deduced from the $V_{3\omega}$ voltage measured across the V+/- voltage taps. On the lock-in amplifier, the magnitude of the voltage at the third harmonic can be isolated. In practical application however, a special circuit must be used to increase the magnitude of the voltage of this harmonic as it is 3 orders of magnitude smaller than the initial voltage drop at ω. Due to the finite dynamic range of the lock-in amplifier, the $V_{3\omega}$ must be made comparable to the

magnitude of $V_{1\omega}$. The use of a high precision reference potentiometer in series with the heater thermometer allows for the matching of the $V_{1\omega}$ voltage. Due to the precision reference resistor having negligible third harmonic voltage generation, the subtraction of the potentiometer voltage from the line heater/thermometer using differential amplifiers enables the measurement of the third harmonic by the lock-in.

Typically, connection to the samples contact pads are made mechanically using a probe station. Individual spring-loaded probes on micropositioners are connected to I+, I-, V+, and V- leads which go to the measurement circuit. The three-axis micropositioners are used to allow for connection to samples with a wide range of thicknesses and heater/thermometer dimensions. Prior to making contact to the Au contact surface on the samples, indium dots are pressed onto the surface of the contact pads to help provide a rigid connection for the spring loaded probes. The round face of the probes in conjunction with the indium dots ensures that the probe does not puncture the surface of the Au contacts or the insulation layers underneath, which can lead to shorting of the circuit for conductive samples.

2.4.6.2. Measurement calibrations

Prior to any measurements by the slope or differential method, two calibrations must be made in order to verify the proper operation of the equipment and to ensure a correct determination of thermal conductivity.

Calibration of reference sample. One of the first steps in the 3ω procedure is a measurement of a reference sample with known thermal conductivity in order to verify that the equipment is set up properly. Typically, a sample such as sapphire or glass is kept near the measurement equipment and is measured prior to any experiment. Any changes in

thermal conductivity from one measurement to another are likely due to circuitry issues, bad contacts, or temperature instabilities.

Calibration of α_{TCR} The normal measurement procedure is performed on the same heater on the same sample at multiple temperatures and the resistance of the heater/thermometer plotted against temperature to determine dR/dT and therefore α_{TCR}. The precise value of α_{TCR} is then used adjusted in the previous slope method calculations to account for the heater metals true temperature coefficient of resistance. *Figure 2.6* demonstrates a typical calibration of a gold heater/thermometer line over the temperature range of 50K-400K.

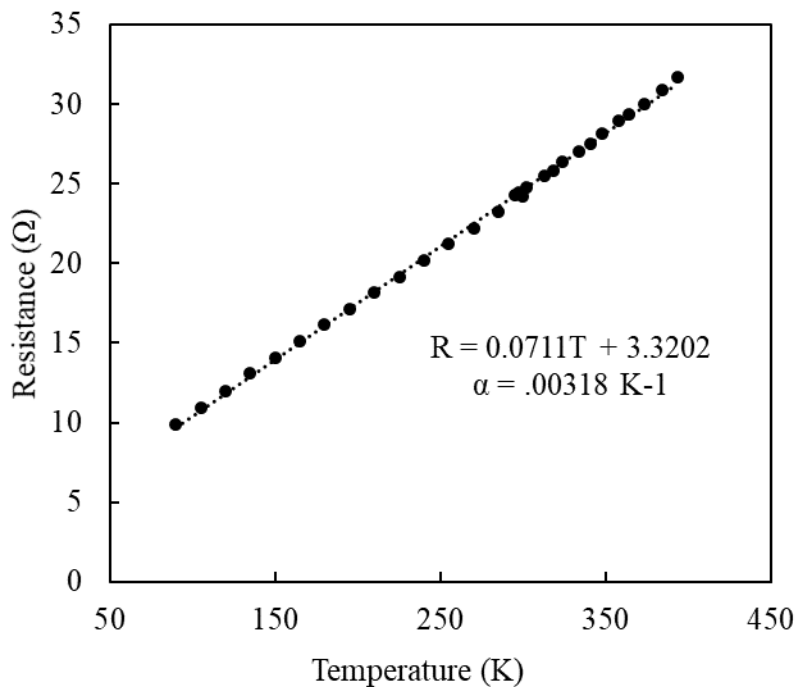

Figure 2.6 *Resistance versus temperature relation for a gold heater/thermometer used to extract α_{TCR}.*

The temperature coefficient of resistance is obtained by dividing the slope dρ/dT by the reference resistivity value for the first temperature in the range used. The gold heater/thermometer device used in this example shows an α_T of 0.00318 K^{-1}, close to the literature values typically ranging from 0.0030 K^{-1} to 0.0034.[4,16] Most devices will have a different temperature coefficient due to differences in impurities and strain on the heater/thermometer from the metallization stage. The calibration of α_T is often reported as the highest source of error in 3omega measurement.[4] Small changes in the α_T value translate to large variations in the slope method calculation. Sources of error when determining α_T include inaccuracies in thermometer use to record sample temperature, unstable or transient temperatures when making calibration, and the temperature range used being too large for a linear α_T measurement. When performing the calibration, the temperature range must be fairly large (above 20°C) in order to get an accurate slope measurement of dρ/dT, but it must be also small enough so that the value of α_T does not change substantially with temperature. The temperature coefficient of resistivity is generally assumed to be linear in most temperature ranges used in experimental measurements. At extreme low or high temperatures, the temperature coefficient of resistance needs to be recalculated over a tighter temperature range of temperatures to account for changes. Metals such as bismuth are unique in that it has a negative temperature coefficient and is very suitable for low-temperature measurements as it retains a temperature coefficient with large magnitude down to a few Kelvin.[17] Finally, the last source of error is related to inaccuracies of the measurement of the sample temperature. Sample temperature must be measured with a thermometer that is in intimate contact with the samples surface such as glued thermocouple or a laser thermometer.

In our experiments, sample temperature was recorded using a Type K thermocouple with +/- 0.5°C error and were verified using a mercury thermometer on the sample. The sample and the thermometers were housed inside an aluminum box to minimize variations due to radiation and air currents.

2.5. Thermal conduction theory in nitrides

2.5.1. Introduction

Chapters 3-6 consist of experimental measurements of thermal conductivity on GaN samples where the effects of film thickness, dislocation density, temperature, impurity concentrations, alloying elements, and/or free electrons are explored. While experimental values are useful for designers in an application based focus, the information gives little information about the physics behind trends. Modeling of experimental data provides the means to understand the physical phenomenon behind the measured trends. The following section covers the model used to simulate the thermal conductivity in some of the studies in the following chapters and a description of the some of the physical phenomenon that affects thermal conductivity in semiconductors.

2.5.2. Modified Callaway model

The common treatment of the thermal conductivity in solids is based on the Callaway's phenomenological formalism where a Debye-like phonon spectrum is assumed and the various phonon scattering processes are accounted for by introducing frequency- and temperature-dependent relaxation times.[18] The Callaway model has been extended and adapted by many researchers[2,19,20] during the years and verified through comparison to experimental data for variety of semiconductor materials, including GaN.[21-23]

The lattice thermal conductivity using the modified Callaway model where the contributions of longitudinal and transverse acoustic phonons are treated separately is given as:[21, 4]

$$k = \sum_s \frac{k_B^4}{6\pi^2 \hbar^3 \upsilon_s} T^3 \left\{ \int_0^{\Theta_D^s/T} \tau_C^s f(x) dx + \left[\int_0^{\Theta_D^s/T} \frac{\tau_C^s}{\tau_N^s} f(x) dx \right]^2 \left[\int_0^{\Theta_D^s/T} \frac{\tau_C^s}{\tau_N^s \tau_R^s} f(x) dx \right]^{-1} \right\} \tag{2.16}$$

where

$$f(x) = \frac{x^4 e^x}{(e^x - 1)^2} \tag{2.17}$$

In Equation (2.16) k_B is the Boltzmann constant, T is the temperature, $\hbar$ is the reduced Planck constant, υ_s is the acoustic phonon velocity, and Θ_D^s is the Debye temperature. For Equation (2.17) the variable of integration x is related to the phonon frequency ω and is defined by $x = \hbar\omega/k_BT$. The summation is over all three acoustic modes in GaN – one longitudinal and two transverse (s = LA, TA1, TA2).

According to the Callaway and Klemens formalism, the combined relaxation rate, τ_C, can be presented by sum: $\frac{1}{\tau_C} = \sum_i 1/\tau_i$, where τ_i is all the relaxation times relevant for the scattering mechanisms that take place in the material system. Scattering processes are accounted for in Equation (2.16) through a combined relaxation time

$$(\tau_C^s)^{-1} = (\tau_N^s)^{-1} + (\tau_R^s)^{-1} \tag{2.18}$$

composed of additive normal (τ_N^s) phonon-phonon and resistive (τ_R^s) scattering processes. Normal phonon-phonon scattering does not directly degrade heat flow, so it is not a resistive process, however it does play an essential role in the phonon distribution and therefore influences all resistive processes. Resistive processes considered in this analysis include Umklapp phonon-phonon τ_U^s, phonon-isotope τ_I^s, phonon-point defect τ_{PD}^s, phonon-dislocation τ_D^s, phonon-boundary τ_B^s, and phonon-free electron τ_{FE}^s scattering so that the resistive scattering rate becomes

$$(\tau_R^s)^{-1} = (\tau_U^s)^{-1} + (\tau_I^s)^{-1} + (\tau_{PD}^s)^{-1} + (\tau_D^s)^{-1} + (\tau_B^s)^{-1} + (\tau_{FE}^s)^{-1} \qquad (2.19)$$

The different scattering mechanisms have different temperature and frequency dependencies, which leads to different weight in the thermal conductivity in different frequency and temperature regions.[19] This in turn result in various approximations and simplified models depending on the specific characteristics of the studied materials, or the respective temperature regions of interest. In this work, the analysis is concentrated in the temperature region above 250K, where all measurements were taken. The modified Callaway model is followed with relaxation times taken in their general forms, however the specifics of crystal structure, phonon spectrum, and defects for GaN are used. In the next section, the details of each scattering process are discussed.

2.5.3. Phonon scattering processes

2.5.3.1. Normal phonon scattering

Normal phonon scattering is known to have a pronounced effect on the phonon distribution. Several groups[21,23,25] reported a significant effect of this scattering at low temperature. At elevated temperatures, the normal phonon-phonon scattering rate is much

smaller than that of the resistive scattering processes, so that $(\tau_N^s)^{-1} \ll (\tau_R^s)^{-1}$, and $\tau_C^s \approx \tau_R^s$. Despite normal phonon-phonon scattering processes not having a large contribution and not directly degrading heat flow, they still have an essential role in phonon distribution and therefore influence all resistive processes. The normal phonon-phonon scattering rate is given by:[21,25]

$$(\tau_N^s)^{-1} = \left(\frac{k_B}{\hbar}\right)^{a+b} \frac{\hbar(\gamma_s)^2 V_o^{(a+b-2)/3}}{M(\nu_s)^{a+b}} x^a T^{a+b} \tag{2.20}$$

where M is the average mass of an atom in the crystal, V_o is the volume per atom, and γ_s is the phonon-mode Grüneisen parameter. The values of a and b depend on the crystal symmetry, the type of phonon mode and the temperature range.[25] In the case of a hexagonal crystals (a, b) = (2, 3) for LA phonons and (a, b) = (1, 4) for TA phonons at low temperatures. At high temperatures (a, b) = (2, 1) for LA phonons and (a, b) = (1, 1) for TA phonons.[25,26]

2.5.3.2. Umklapp scattering

Umklapp scattering is considered to have determining contribution at high temperatures for pure materials. It is the main resistive process in defect-free crystals and leads to an exponential decay of the thermal conductivity at high temperatures. Several models described the Umklapp scattering rates and their dependence on temperature. Based on the model by Slack and Galginaitis,[27] the Umklapp phonon-phonon scattering rate is[21]

$$(\tau_U^s)^{-1} = \frac{(k_B)^2(\gamma_s)^2}{\hbar M(\nu_s)^2\theta_D^s} \exp\left(-\frac{\theta_D^s}{3T}\right) x^2 T^3 \tag{2.21}$$

where M = 42.1684 amu is the averaged atomic mass for natural GaN. The expression of the U-scattering rate is assumed to be identical for all phonon modes. The difference in the contributions of longitudinal and transverse phonons comes only from the mode-dependent material parameters.

2.5.3.3. Phonon-isotope scattering

Phonon-isotope scattering is essentially scattering due to the mass fluctuation in crystals where various isotopes of the constituent chemical elements are present. This scattering is shown to reduce the maximum thermal conductivity (typically occurring at $T \approx 0.05\theta_D$) by 30-50% and to affect even room-temperature values in various undoped and low-doped semiconductors.[21,24] As shown by Klemens[28] the scattering of phonons by a defect with mass different from that of the host atom follows a Rayleigh scattering law, therefore the phonon-isotope scattering rate is given by[21]

$$(\tau_I^s)^{-1} = \left(\frac{k_B}{\hbar}\right)^4 \frac{V_o}{4\pi(v_s)^3} \Gamma_I x^4 T^4 \tag{2.22}$$

Explicitly for GaN the strength of the phonon-isotope scattering Γ_I can be written as[21]

$$\Gamma_I = 2\left[\left(\frac{M_{\mathrm{Ga}}}{M_{\mathrm{Ga}} + M_{\mathrm{N}}}\right)^2 \Gamma(\mathrm{Ga}) + \left(\frac{M_{\mathrm{Ga}}}{M_{\mathrm{Ga}} + M_{\mathrm{N}}}\right)^2 \Gamma(\mathrm{N})\right] \tag{2.23}$$

Here $\Gamma(p)$ is the scattering parameter for a single chemical element (p = Ga, N):

$$\Gamma\,(p) = \sum_i c_i^p \left(\frac{m_i^p - M_p}{M_p}\right)^2 \tag{2.24}$$

and

$$M_p = \sum_i c_i^p m_i^p \tag{2.25}$$

where m_i^p is the atomic mass of the ith isotope and c_i^p is the fractional atomic natural abundance. There are two Ga isotopes – ^{69}Ga and ^{71}Ga with 60.108% and 39.892% abundance, respectively, and two N isotopes – ^{14}N (99.632%) and ^{15}N (0.368%).[29] Using Eqs. (8-10) and the exact atomic mass of isotopes[30, 31] we calculate $\Gamma_I = 2.744\times10^{-4}$.

2.5.3.4. Phonon-point defect scattering

Phonon point defect scattering can be considered as scattering of the phonons by defect (substitutional impurity or vacancy) with a mass different from the mass of the host atom in the crystal lattice. Phonon-point defect scattering can also be due to a change in the force constant of the bonds in the crystal or a strain field around imperfections produced by the size difference of the defect and host atoms. Since point defects disturb the lattice due to mass difference, they are treated similar to isotopes and a Rayleigh scattering law is used. The scattering rate for point defects is given by Klemens as[28]

$$(\tau_{PD}^{s})^{-1} = \left(\frac{k_B}{\hbar}\right)^4 \frac{V_o}{4\pi(\nu_s)^3}\Gamma_{PD}x^4T^4 \tag{2.26}$$

When several substitutional impurities are present in the crystal the strength of the *PD*-scattering Γ_{PD} is given by[20,28]

$$\Gamma_{PD} = \sum_i f_i \left\{\left(\frac{M_i - M}{M}\right)^2 + 2\left[\left(\frac{G_i - G}{G}\right) - 2Q\gamma_s\left(\frac{\Delta R_i}{R}\right)\right]^2\right\} \tag{2.27}$$

where f_i and M_i are the fractional concentration and the atomic mass of the ith impurity, G_i is the average stiffness constant of the nearest-neighbor bonds between the ith impurity and the host atoms, G is the average stiffness constant of the bonds in the host crystal, ΔR_i is the

average local displacement in the host lattice due to the ith impurity, and R is the average nearest-neighbor atomic radius in the host crystal. The displacement ΔR_i is generally defined as the difference between the Pauling ionic radii of the impurity and the host atom. The constant Q equals 4.2 if the nearest-neighbor bonds of the impurity have the same anharmonicity as all other bonds, or $Q = 3.2$ if the anharmonicity of the nearest-neighbor bonds is excluded.[28] The second term in Equation (2.27) is usually neglected because of the lack of data about the change in the stiffness constants in the presence of a substitutional impurity. On the other hand, the Pauling ionic radii are known to depend on the charge state, the electronic spin state, and the coordination number. Moreover, the ionic radii of atoms in a semiconductor crystal differ from the ionic radii of "free" atoms due to the partial or complete covalent character of the bonds [38]. So, the third term in Equation (2.27), which accounts for the phonon scattering by the elastic strain field, is in some way ambiguously defined. To refine the analysis, we set $(G_i - G)/G = -2\gamma_s\,(\Delta R_i/R)$, which reflects the fact that in most semiconductors the elastic constants depend on the atomic volume only[20] and $Q = 4.2$ (i. e. it is assumed that the impurities do not change the anharmonicity of the bonds[28]). Then, to be consistent with the above approximation, the displacement ΔR_i is calculated from the difference between the average bond length in the host crystal and the average bond length in the presence of an impurity for a relaxed lattice. The vacancies are treated in the same way but with $M_i = 0$, $G_i = 0$, and $Q = 3.2$.

2.5.3.5. Phonon-dislocation scattering

Phonon-dislocation scattering needs to account for two main components, namely scattering from the core of the dislocation lines and scattering from the elastic strain field of

the dislocation lines. Including contributions of edge and screw dislocations, the phonon-dislocation scattering rate is[22,28]

$$(\tau_D^S)^{-1} = \eta N_D \left(\frac{k_B}{\hbar}\right)^3 \frac{(V_o)^{4/3}}{(\nu_s)^2} x^3 T^3 + 0.06\eta \left(\frac{k_B}{\hbar}\right) (\gamma_s)^2 \left[N_S {b_S}^2 + N_E {b_E}^2 {P_E}^2\right] xT \quad (2.28)$$

where N_D is the total dislocation density, N_S and N_E are the densities of screw and edge dislocations, η is the weight factor accounting for the mutual orientation of the dislocation line and the temperature gradient, and $b_S = c_o$ and $b_E = a_o\sqrt{2}/3$ are the magnitudes of Burgers vectors for the screw and edge dislocations (a_o and c_o are the lattice constants in a wurtzite crystal), respectively. The parameter P_E depends on both the ratio between the phonon velocities for two polarizations, ν_L/ν_T, and the Poisson ratio.[28] The first and the second terms in Equation (2.28) represent the scattering on the core and the scattering by the elastic field, respectively. Such a treatment of the phonon-dislocation scattering predicts that the thermal conductivity of GaN is independent of the dislocation density for $N_D < 10^{10}$ cm^{-2}.[22] However, the analysis of experimental data for a variety of materials has showed that the Klemens formulation underestimates the phonon-dislocation scattering rates by a factor of 10^2-10^3.[32] In fact, previous data for thick HVPE grown GaN has revealed that the dislocations start to affect the thermal conductivity at $N_D > 10^6$ cm^{-2}.[33] Remarkably, the thermal conductivity dependence on the dislocation density experimentally observed for $N_D > 10^6$ cm^{-2} is very similar to that calculated through Equation (2.38) for $N_D > 10^{10}$ cm^{-2}.[22] Therefore, a dimensionless pre-factor of 1000 is introduced in the right part of Equation

(2.38) in order to match the threshold value of N_D;[34] This does not affect our analysis because the dislocations density in all samples investigated is < 5×10^5 cm^{-2}.

2.5.3.6. Phonon-free electron scattering

Phonon-free electron scattering is often neglected in the computation of thermal conductivity in semiconductors as it usually has a much smaller contribution than other resistive scattering processes. However, for doped semiconductors at elevated temperatures where even in the wide-bandgap materials most of the donors are ionized the role of free electron scattering cannot be neglected. This is even more essential for highly doped samples with high free carrier concentrations. Using an effective mass approximation, the phonon-free electron scattering rate is accounted for by the Ziman[35,36] term and is expressed as

$$(\tau_{FE}^{s})^{-1} = \frac{(E_1)^2(m_e)^2 k_B T}{2\pi\hbar^4 \rho \nu_s}\left[x - \ln\left(\frac{1+\exp(Z+x/2)}{1+\exp(Z-x/2)}\right)\right] \qquad (2.29)$$

and

$$Z = \frac{x^2 k_B T}{8 m_e (\nu_s)^2} + \frac{m_e(\nu_s)^2}{2 k_B T} - \frac{E_F}{k_B T} \qquad (2.30)$$

where E_1 is the deformation potential for electron-acoustic phonon interaction (E_1=8.3x10^{-19} J),[22] m_e is the effective mass of the free carriers, ρ is the mass density, and E_F is the Fermi-level energy measured from the bottom of the conduction band.

2.5.3.7. Phonon-boundary scattering

Phonon-boundary scattering is included in the model following Ziman's approach[35] and a more recent consideration of bulk samples.[37] In the bulk samples, Simon et. al.[37] assumed a diffusive character of the phonon scattering, and the relatively large penetration depth of the heat waves in GaN was taken into account. Realistic sample dimensions

typically used for thermal conductivity measurements of about 1 cm^2 were considered in the model to allow a correct comparison with experimental data. The phonon-boundary-scattering rate is independent of the phonon frequency and leads to T^3 dependence of the thermal conductivity below its maximum at $T \approx 0.05\theta_D$. The B-scattering rate is usually expressed in terms of effective phonon mean path, L_{ph}:[24]

$$(\tau_B^s)^{-1} = \frac{v_s}{L_{ph}} = v_s\left(\frac{1}{1.12\sqrt{ab}} + \frac{1}{d}\right) \tag{2.31}$$

where ab is the cross section of the samples and d is the sample length in the direction of the heat flow.

2.5.4. Summary

For semiconductors with moderate doping levels near room temperature, the primary contribution to the thermal conductivity is via phonon transport in the lattice as transfer of heat by electrons provides a contribution three orders of magnitude smaller. Therefore, to simulate the experimental results, a modified Callaway model is used to theoretically calculate the lattice thermal conductivity and understand the physical phenomenon behind the trends. The modified Callaway model was chosen to model the lattice thermal conductivity due to its proven success for a variety of semiconductor materials and the ability to tailor the calculation for a specific temperature ranges and scattering phenomenon. In the model, both normal and resistive scattering processes were taken into account, where resistive scattering processes provide the main source of the reduction of lattice thermal conductivity in undoped to moderately doped semiconductors above room temperature. Resistive scattering processes accounted for in the model included contributions from

Umklapp, isotope, point defect, dislocation, free electron, and boundary scattering mechanisms. Using the modified Callaway model, contributions from each scattering mechanism can be adjusted to model a variety of types of GaN in a wide range of temperatures.

References

1 Wide Bandgap Semiconductors: Pursuing the Promise, US Department of Energy: Advanced Manufacturing Office (2013).

2 C. M. Bhandari, and D. M. Rowe, Thermal Conduction in Semiconductors, (Wiley, New Delhi u. a, 1988).

3 H. S. Carslaw, and J. C. Jaeger, Conduction of Heat in Solids, 2. ed., reprint. ed. (Clarendon Pr, Oxford, 2011).

4 C. Mion, Investigation of the Thermal Properties of Gallium Nitride using the Three Omega Technique, (2005).

5 D. G. Cahill, M. Katiyar, and J. R. Abelson, Thermal conductivity of a-Si:H thin films, Physical Review B 50, 6077 (1994).

6 C. E. Dames, Thermal Properties of Nanowires and Nanotubes: Modeling and Experiments, (2006).

7 S. L. Shindé, High Thermal Conductivity Materials, (Springer, New York, 2006).

8 S. Li, A Fundamental Introduction of Time Domain Thermoreflectance (TDTR), (2011).

9 A. L. Lytle, Ångström's Method of Measuring Thermal Conductivity, (2000).

10 T. Hashimoto, J. Cao, and A. Takaku, Thermal diffusivity measurements for thin films by the photoacoustic effect, Thermochimica Acta 120, 191 (1987).

11 R. L. Thomas, M. J. Lin, P. K. Kuo, D. Fournier, D. S. Kim, N. Yacoubi, A. C. Boccara, L. D. Favro, S. Zhang, C. B. Reyes, and L. J. Inglehart, Mirage-effect measurement of thermal diffusivity. Part I: experiment, Canadian Journal of Physics 64, 1165 (1986).

12 D. G. Cahill, Thermal conductivity measurement from 30 to 750 K: the 3ω method, Rev. Sci. Inst. 61, 802 (1990).

13 T. Borca-Tasciuc, A. R. Kumar, and G. Chen, Data reduction in 3ω method for thin-film thermal conductivity determination, Review of Scientific Instruments 72, 2139 (2001).

14 M. B. Beaudhuin, and L. Van der Tempel, Thermal Conductivity Measurement of Thin Layers by the 3 Omega Method, (2006).

15 H. Lama, S. Anomitra, and Kasiviswanathan, Choice of Metal Heaters for Measuring Thermal Conductivity using 3ω Method, AIP Conference Proceedings 1312 (2013).

16 Temperature Coefficient of Resistance, www.resistorguide.com.

17 T. Hänninen, Implementing the 3-Omega Technique for Thermal Conductivity Measurements, (2013).

18 J. Callaway, Model for Lattice Thermal Conductivity at Low Temperatures, Physical Review 113, 1046 (1959).

19 M. G. Holland, Analysis of Lattice Thermal Conductivity, Physical Review 132, 2461 (1963).

20 B. Abeles, Lattice Thermal Conductivity of Disordered Semiconductor Alloys at High Temperatures, Physical Review 131, 1906 (1963).

21 D. T. Morelli, J. P. Heremans, and G. A. Slack, Estimation of the isotope effect on the lattice thermal conductivity of group IV and group III-V semiconductors, Physical Review B 66, (2002).

22 J. Zou, D. Kotchetkov, A. A. Balandin, D. I. Florescu, and F. H. Pollak, Thermal conductivity of GaN films: Effects of impurities and dislocations, Journal of Applied Physics 92, 2534 (2002).

23 M. D. Kamatagi, N. S. Sankeshwar, and B. G. Mulimani, Thermal conductivity of GaN, Diamond & Related Materials 16, 98 (2007).

24 M. Asen-Palmer, K. Bartkowski, E. Gmelin, M. Cardona, A. P. Zhernov, A. V. Inyushkin, A. Taldenkov, V. I. Ozhogin, K. M. Itoh, and E. E. Haller, Thermal conductivity of germanium crystals with different isotopic compositions, Physical Review B 56, 9431 (1997).

25 C. Herring, Role of Low-Energy Phonons in Thermal Conduction, Physical Review 95, 954 (1954).

26 R. Berman, C. L. Bounds, and S. J. Rogers, The Effect of Isotopes on Lattice Heat Conduction. II. Solid Helium, Proceedings of the Royal Society of London. Series A. Mathematical and Physical Sciences 289, 66 (1965).

27 G. A. Slack, and S. Galginaitis, Thermal Conductivity and Phonon Scattering by Magnetic Impurities in CdTe, Physical Review 133, (1964).

28 P. G. Klemens, The Scattering of Low-Frequency Lattice Waves by Static Imperfections, Proceedings of the Physical Society. Section A 68, 1113 (1955).

29 K. J. R. Rosman, and P. D. P. Taylor, Isotopic compositions of the elements 1997 (Technical Report), Pure and Applied Chemistry 70, 217 (1998).

30 G. Audi, and A. H. Wapstra, The 1993 atomic mass evaluation(I) Atomic mass table, Nuclear Physics A 565, 1 (1993).

31 G. Audi, and A. H. Wapstra, The 1995 update to the atomic mass evaluation, Nuclear Physics, Section A 595, 409 (1995).

32 R. Berman, Thermal Conduction in Solids, 1. publ. in paperback ed. (Clarendon Pr, Oxford, 1979).

33 C. Mion, J. F. Muth, E. A. Preble, and D. Hanser, Accurate dependence of gallium nitride thermal conductivity on dislocation density, Applied Physics Letters 89, 92123 (2006).

34 T. E. Beechem, A. E. McDonald, E. J. Fuller, A. A. Talin, C. M. Rost, J. Maria, J. T. Gaskins, P. E. Hopkins, and A. A. Allerman, Size dictated thermal conductivity of GaN, Journal of Applied Physics 120, 95104 (2016).

35 J. M. Ziman, The Effect of Free Electrons on Lattice Conduction, Philosophical Magazine 1, 191 (1956).

36 J. M. Ziman, The effect of free electrons on lattice conduction, Philosophical Magazine 2, 292 (1957).

37 R. B. Simon, J. Anaya, and M. Kuball, Thermal conductivity of bulk GaN—Effects of oxygen, magnesium doping, and strain field compensation, Applied Physics Letters 105, 202105 (2014).

3. Thermal conductivity of n-type GaN

This chapter covers both undoped GaN and intentionally doped n-type GaN using Si dopants. Undoped GaN falls into the same category of n-type material due to the fact that residual impurities, such as Si and O, remain unavoidable in the current growth technology and establish its unintentional n-type character. Some results for n-type GaN are published in our chapter in *Handbook of GaN Semiconductor Materials and Devices*[1] and two published works in Journal of Applied Physics[2] and Physica Status Solidi (b).[3] The main focus of the undoped section is a comparison of heteroepitaxial and homoepitaxial GaN, which have differing properties leading to vastly different thermal conductivities. This section is presented first, as it is valuable for comparison to GaN with other dopants, alloying elements, and to other wide-bandgap materials which are presented in the following chapters. While focused on GaN, this chapter also includes a short discussion on the thermal conductivity of bulk AlN, which is a closely related material and necessary for the discussion of the thermal conductivity of AlGaN alloys presented in Chapter 5.

3.1. Introduction

One of the largest drawbacks for using heteroepitaxially grown GaN for power device applications is the low thermal conductivity of most of the typically used foreign substrates. High power and current in devices generates a substantial amount of Joule heating that must be removed to prevent failures associated with operation outside of the devices temperature range. In order to remove the heat generated during operation, the substrate must have thermal conductivity equal to or greater than the material of the device in order to effectively

transfer heat to a heat sink or to be radiated to air. Typical thermal conductivities of foreign substrates used for epitaxial growth such as sapphire (~23 W/mK) and silicon (~110 W/mK) are lower than that of undoped or lightly doped GaN and act as a thermal barrier for heat flow out of the device. The most appropriate substrate for GaN would be an undoped native GaN substrate, which would provide thermal conductivity (>200 W/mK). Foreign substrates such as SiC would provide high thermal conductivity needed for thermal management, however, the need for a buffer, the misfit dislocation generation, and the thermal barrier resistance may negate their benefits.

A thermal conductivity of ~150 $Wm^{-1}K^{-1}$ at room temperature was typically reported for thin GaN epilayers with dislocation densities typically in the range of 10^8-10^9 cm^{-2}, which is relatively lower compared to that of SiC.[4-7] Recent major advances in GaN crystal growth have resulted in significantly improved material properties of GaN substrates.[8-12] Slack *et al.* reported 227 $Wm^{-1}K^{-1}$ for an undoped GaN plate grown by hydride vapor phase epitaxy (HVPE),[8] estimated using a steady-state heat flow method. For low threading dislocation density bulk GaN of 5×10^5 cm^{-2}, Mion *et al.* demonstrated an improvement in the thermal conductivity of HVPE bulk GaN, reaching 230 $Wm^{-1}K^{-1}$ for Fe-doped GaN, determined through the 3ω method.[10] These values are quite close to the value predicted by the first-principles calculation for a natural (not isotope pure) GaN – 242 W/mK.[13] For undoped GaN, Richter *et al.* achieved a thermal conductivity of ~290 $Wm^{-1}K^{-1}$,[11] while Shibata *et al.* reported a GaN thermal conductivity as high as 380 $Wm^{-1}K^{-1}$,[12] both determined using the laser flash method. Both studies are consistent with the theory from Witek, suggesting a maximum GaN intrinsic thermal conductivity of 410 $Wm^{-1}K^{-1}$.[14] Despite the large variation

in the recently reported numbers, most likely related to different ensemble of residual impurities and native point defects as a result of specific backgrounds and sources used in the different growth techniques, the numbers are consistently reported larger than previously thought**.** *Figure 3.1* shows the thermal conductivity of GaN from publications vs. the year

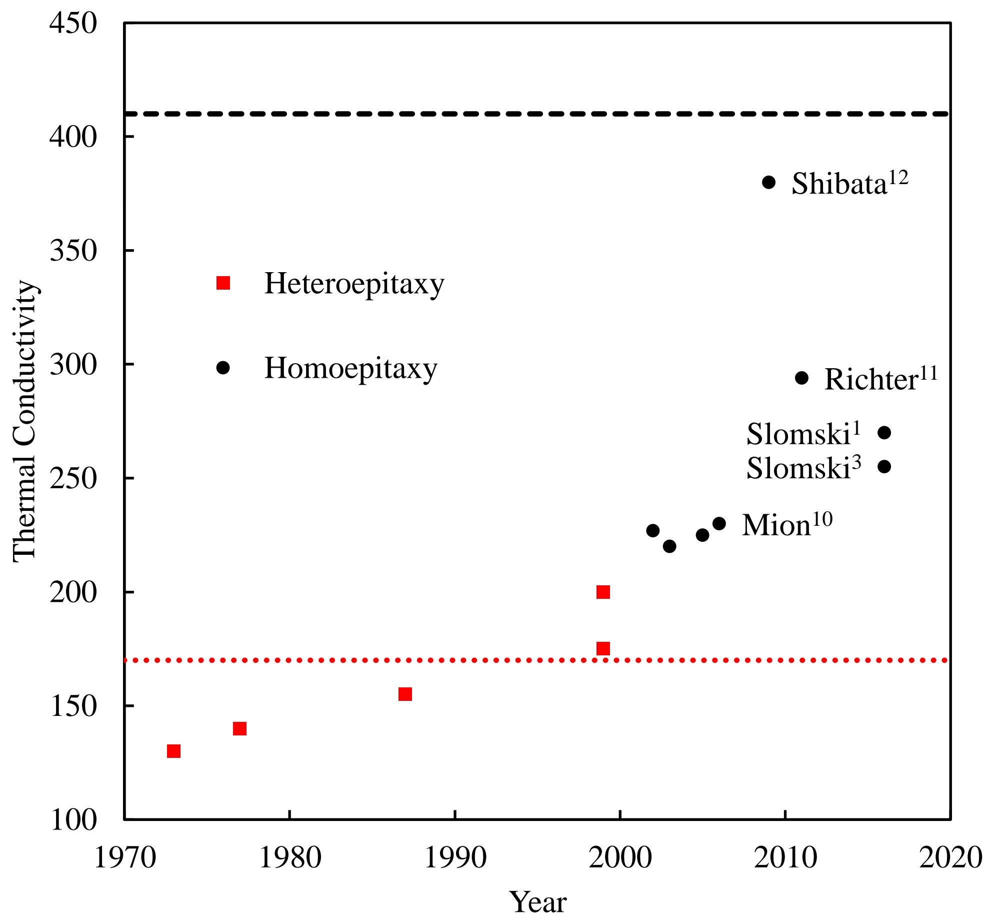

Figure 3.1 *Reported thermal conductivity of heteroeptixial (squares) and homoepitaxial (circles) GaN vs. year of publication. Lower dashed line is theoretical limit of Slack[15] from 1973 and upper dashed line is limit of Witek[14] from 1997.*

of publication. *Figure 3.1* shows the theoretical maximum thermal conductivity as reported in 1973 by Slack[15] and in 1997 by Witek[14]. In 1973, Slack calculated the thermal conductivity without the knowledge of many material parameters of GaN and used a scaling factor to predict values. In the following years, state of the art heteroepitaxial GaN samples seemed to abide by the proposed limit of Slack. In 1999, the theoretical limit from Slack was surpassed by Asnin et al. who grew GaN on sapphire using lateral epitaxial overgrowth.[16] In *Figure 3.1*, the red squares represent GaN grown heteroepitaxially on foreign substrates such as sapphire, while the circles represent samples grown on native GaN substrates. It can be seen that most of the heteroepitaxial samples are below the limit predicted by Slack, which were the only samples he had access too at the time. All bulk samples on the graph fall above the limit of Slack, likely due to much lower dislocation densities and improvements in other material properties.

Following the work of Slack[17], Witek[14] predicted a near theoretical maximum for the intrinsic thermal conductivity of GaN using known values of the Gruneisen parameter and not including the scaling factor used by Slack. Since then, thermal conductivity values have continued to climb towards and approach the new theoretical limit of 410 W/mK. Despite the increasing values of thermal conductivity, there has been a large variation in the reported values since the year 2000. This is likely due to different amounts of dislocations, impurities, vacancies, and other defects stemming from the different growth techniques used by the researchers which have a strong effect on the lattice thermal conductivity in GaN.

The effect of the impurities (unintentional or intentional) on the thermal conductivity of GaN is not well understood. Previous studies on doped GaN have been done on material

with a high dislocation density[6,18] or on specific samples doped with either Fe, or O, or Mg.[10,19,20] There is no systematic study on the effect of a single impurity on the thermal conductivity. Since Si is the main dopant for achieving *n*-type conductivity in GaN and *n*-type GaN substrates are needed for most of group-III nitrides devices, a detailed study of the role of Si doping on the thermal conductivity is highly needed.

In this work, we studied the thermal conductivity of Si-doped, low-dislocation-density bulk GaN grown by HVPE and have compared it to results of undoped n-type bulk GaN. The 3ω method was used to measure the thermal conductivity of a series of samples in a temperature range of 295-470 K. The experimental data is compared to theoretical calculations based on the modified Callaway model introduced in Chapter 2 in order to understand the role of the different phonon scattering mechanisms influencing the thermal conductivity at high temperatures.

3.2. Experimental details

3.2.1. Sample growth and characterization

The samples measured in this section were grown by the growth techniques described in Chapter 1. The bulk GaN samples were grown either by HVPE or by a mixed growth technique of HVPE on ammonothermal seeds and they are compared to heteroepitaxial layers grown by various techniques of other researchers. The AlN sample was grown by a modified HVPE growth.

All of the intentionally doped samples measured were grown using HVPE in a vertical reactor at Kyma Technologies Inc. GaN layers with thickness of ~1 mm were grown on (0001) sapphire from which they were self-separated during cooldown. The lateral

dimensions of the samples used in thermal conductivity measurements ranged from 5×5 mm^2 to 10×10 mm^2.

Silicon doping was achieved using silane (SiH_4) introduced into the reactor with nitrogen (N_2) carrier flow. The Si concentration was controlled by varying the silane flow in a range of 0-250 sccm. All other growth conditions, such as the growth temperature, N_2 carrier flow and III/V ratio, were purposely kept constant. Secondary ion mass spectroscopy (SIMS) measurements were used to determine the total Si concentrations, as well as some of the typical residual impurities in HVPE grown GaN – oxygen, hydrogen and carbon. The Si concentration was found to range from 1×10^{16} cm^{-3} in the undoped sample to 7×10^{18} cm^{-3} in the highest doped sample. Also, the SIMS data revealed that the concentrations of [O] ≈ 2.3×10^{16} cm^{-3}, [H] ≈ 1.5×10^{18} cm^{-3}, and [C] ≈ 7×10^{15} cm^{-3} were unaltered by the varying the Si doping. The free electron concentration, n_e, as determined by conventional Hall effect measurements at room temperature showed a nearly complete donor ionization, i. e. the n_e scales closely with the Si concentration in an agreement with previous studies.[21] The Ga vacancy density was studied by positron annihilation spectroscopy (PAS). In all samples, no vacancy signal was detected which leads to the conclusion that the Ga vacancy density was below 1×10^{15} cm^{-3} (detection limit of the PAS). All samples exhibited a threading dislocation density of < 5×10^{6} cm^{-2} as determined by etch pit density and cathodoluminescence. The data from SIMS, PAS and Hall measurements for all studied samples are summarized in *Table 3.1*.

Table 3.1 *Impurity concentrations, Ga vacancy (V_{Ga}) concentrations, free electron (n_e) concentrations, and the resistivity of samples as determined by SIMS, PAS and Hall measurements.*

SiH4 flow (norm)	Si (cm^{-3})	O (cm^{-3})	H (cm^{-3})	C (cm^{-3})	V_{Ga} (cm^{-3})	n_e (cm^{-3})	Resistivity (Ωm)
0	1.6×10^{16}	2.3×10^{16}	1.5×10^{18}	7×10^{15}	1×10^{15}	1.1×10^{16}	0.74
1	7.3×10^{16}	2.3×10^{16}	1.5×10^{18}	7×10^{15}	1×10^{15}	7.3×10^{16}	0.05
8	1×10^{18}	2.3×10^{16}	1.5×10^{18}	8×10^{15}	1×10^{15}	4×10^{17}	0.015
20	3.5×10^{18}	2.7×10^{16}	1.5×10^{18}	8×10^{15}	1×10^{15}	2×10^{18}	0.011
40	7×10^{18}	2.3×10^{16}	1.5×10^{18}	7×10^{15}	1×10^{15}	6×10^{18}	0.005

3.2.2. 3ω measurement details

Characterization of the thermal conductivity was performed using the 3ω method.[22] In order to verify the boundary conditions, the penetration depth in Equation (2.6) was used along with the material properties for the specific samples in this experiment. For example, an undoped GaN sample with a thermal conductivity of about 200 W/mK, density $\rho = 6150$ kg/m^3 and specific heat $C_P = 490$ J/kgK, has a thermal penetration depth ranges from 325 μm at a frequency of 50 Hz to 36 μm at 4000 Hz. For the conditions of this experiment, it was found that a frequency range of 50-4000 Hz met the boundary conditions which was verified experimentally by the linear relation of the $V_{3\omega}$ vs. ln(ω).

An isolating layer of SiO_2 was then deposited onto the surface at a thickness of 100-150nm. For the samples used in this experiment, namely thick bulk GaN samples, a line with a width of 6μm, length of 3mm, and a thickness of 200nm was found optimal for the slope method. The temperature was varied by the use of a hot plate with a thermally shielded cover

and was measured within +/- 2K using a type-K thermocouple in intimate contact with the sample.

3.3. Results and discussion

3.3.1. Undoped bulk GaN

Figure 3.2(a) shows temperature dependence of thermal conductivity, measured in the temperature range of 300 to 460 K for two bulk GaN samples grown by HVPE on sapphire (provided by Kyma Technology) and on ammonothermal bulk GaN substrates (provided by Unipress) after removing the substrates for both. The two samples have dislocation density in the range of 10^6 cm^{-2} and 10^4 cm^{-2}, and slightly different thermal conductivity of 265 and 279 W/mK at RT, respectively. The latter is a bit surprising, considering that most theoretical models predict no significant effect of the dislocation density below 10^8cm^{-2} on the thermal conductivity, which calls for a more precise analyses of additional factors that may play a role.[6,10] The dependence of temperature is proportional to a power law

$$k(T) = k_o \left(\frac{T_o}{T}\right)^{\alpha} \quad (3.32)$$

with α= 1.40 and 1.38, respectively, for these two representative samples. This slope is close to previously estimated slope of 1.43 and is characteristic of pure adamantine crystals in the temperature range below the Debye temperature.[10]

3.3.2. Bulk AlN

The thermal conductivity of bulk AlN, reported so far, varies greatly, which was attributed to difference in the purity and microstructure of AlN.[4,23] The largest reported thermal conductivity value to date is 340 W/mK at room temperature reported by Rojo et

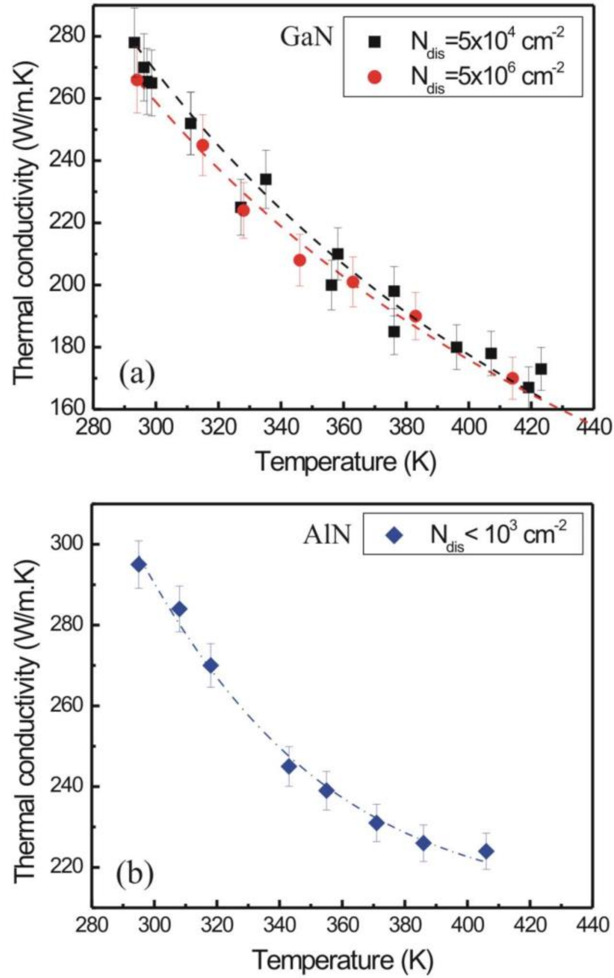

Figure 3.2 *Temperature dependence of thermal conductivity of: (a) free standing GaN grown by HVPE on sapphire with dislocation density of about* 10^6 cm^{-2} *and on ammonothermal bulk GaN with dislocation density of about* 10^4 cm^{-2}*; (b) bulk AlN grown by modified HVPE method with dislocation density* $<10^3$ cm^{-2}.

al.[24] One of the problems caused by unavoidable oxygen impurities was a significant reduction of intrinsic thermal conductivity. The thermal conductivity at room temperature of several samples was analyzed as a function of oxygen concentration, resulting in a trend that extrapolated to 320 W/mK for pure AlN.

We have measured the temperature dependence of thermal conductivity of AlN bulk samples grown by modified HVPE (provided by Nitride Solutions) in temperature region of 300-460 K (*Figure 3.2(b)*). The thermal conductivity at RT was determined have a high value of 295 W/mK, likely attributed to its relatively low dislocation density of ~5×10^{3} cm^{-2} The temperature dependence slope was determined to be 1.11, which is lower than the values of 1.21 estimated by Slack et al.[4] explained by acoustic phonon transport, and is indicative that more complex scattering mechanism are in play. This hypothesis is strengthened by observation of the samples dark reddish brown color, which may possibly be caused by point-defects in the bulk.

3.3.3. Intentionally doped n-type GaN

The addition of Si dopants into GaN for the purpose of increasing the electrical conductivity have the effect of decreasing the thermal conductivity from the maximum values found for the undoped samples in the previous section. All GaN samples were measured at identical conditions, namely, the same dimensions of the 3ω devices and the same frequency range. With increasing Si concentration, the thermal conductivity gradually decreased and for the sample with the highest doping (7×10^{18} cm^{-3}), $k = 210 \pm 6$ W/mK was found. Such a behavior is quite reasonable and can be simply explained by an increased contribution of phonon-point-defect scattering. At elevated temperatures ($T > 295$ K) the thermal conductivity for all samples decreased with increasing temperature, as seen in *Figure 3.3*. However, the rate of the decrease, or the slope of the temperature dependence of k, was different for different Si concentrations, which will be discussed later.

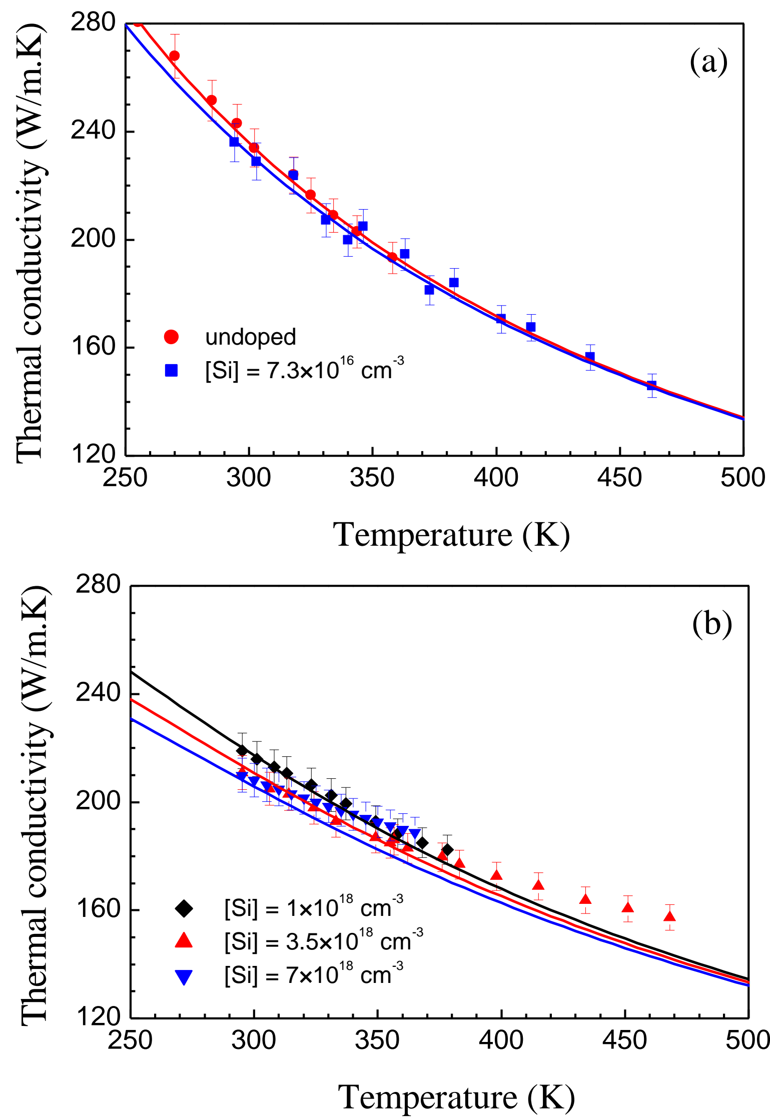

Figure 3.3 *Experimental data (symbols) and theoretical calculations (lines) for the thermal conductivity vs temperature of (a) undoped and low Si doped GaN and (b) highly Si doped GaN (>10^{18} cm^{-3}).*

Usually, to analyze the temperature dependence of the thermal conductivity of solids and to distinguish between the contributions of different phonon scattering processes the experimental data is fitted by the Callaway[25] or Holland[26] models. In doing so, the

coefficients in front of the frequency and temperature dependence in the scattering rate expressions for different scattering processes are used as fitting parameters.[27] For undoped and isotopically pure materials with high crystalline quality, such an approach works very well because only the phonon-phonon scattering contributes to the thermal conductivity and few adjustable parameters are needed, such as the *N*- and *U*-scattering rate coefficients for longitudinal and transverse phonon modes. However, the presence of dopants, free carriers, and dislocations in most of the technologically important semiconductor materials requires all scattering mechanisms to be included in the analysis. Thus, the number of the fitting parameters increases considerably and the fitting procedure becomes more complicated. The Callaway model, with some approximations, has been successfully used to fit thermal conductivity data for various GaN samples.[19, 28-31] However the extracted values for the scattering rate coefficients, which in principle only depend on the material parameters, are quite different.

To analyze our experimental data a slightly different approach was employed. The modified Callaway model (as described in Chapter 2) was applied to fit the temperature dependence of the thermal conductivity, but instead of the numerous scattering rate coefficients only the Grüneisen parameters for longitudinal and transverse phonons, γ_L and γ_T, were used as adjustable parameters. This approach is justified by the fact that all other material parameters in Equations (2.26) – (2.41) are fairly well known for GaN and are summarized in *Table 3.2*.

Table 3.2 *Material parameters of GaN used in the thermal conductivity calculations.*

Material parameter	
Debye temperature, K	$\theta_D^L = 439$ $\theta_D^{T1} = 310$ $\theta_D^{T2} = 310$
Grüneisen parameter	$\gamma_L = 0.80$ $\gamma_T = 0.61$
Acoustic phonon velocity, m/s	$\nu_L = 7644$ $\nu_{T1} = 3992$ $\nu_{T2} = 4326$
Lattice constant, Å	$a_o = 3.1893$ $c_o = 5.1852$
Density, kg/m^3	$\rho = 6150$
Volume per atom, m^3	$V_o = 1.1422\times10^{-29}$
Average atomic mass, amu	$M = 41.8649$
Average atomic radius, Å	$R = 0.9752$
Atomic mass, amu	$M_{Si} = 28.0854$ $M_O = 16.0575$ $M_C = 12.0107$
Average displacement in the host lattice, Å	$\Delta R_{Si} = -0.0826$ $\Delta R_O = +0.0327$ $\Delta R_C = -0.0195$ $\Delta R_{VGa} = +0.1121$
Strength of the phonon-isotope scattering	$\Gamma_I = 2.744\times10^{-4}$
Electron effective mass, m_o	$m_e = 0.23$
Electron-acoustic phonon deformation potential, eV	$E_1 = 9.1$

The mode-dependent Grüneisen parameters represent the anharmonicity of the atomic interactions in the crystal structure and are defined as[32]

$$\gamma_s(q_s) = -\frac{V}{\omega_s(q_s)}\frac{\partial\omega_s(q_s)}{\partial V} \tag{3.33}$$

where ω_s is the phonon frequency, q_s is the phonon wavevector, and V is the volume. Experimentally, the Grüneisen parameters can be obtained from the pressure dependence of the phonon frequencies. Unfortunately, there is no such data for the acoustic phonon modes in GaN. For zinc-blende GaN, *ab initio* lattice-dynamic calculations revealed γ_s values in the range 0.4 – 1.3 for different phonon modes and for some modes negative values were found.[32]Mode-averaged Grüneisen parameters for wurtzite GaN of $\gamma = 0.74$ and $\gamma = 0.85$ have been extracted from the thermal expansion and specific heat measurements.[14,33] Due to the uncertainty in the suggested values we prefer to use the Grüneisen parameters as fitting parameters. The values for γ_L and γ_T listed in *Table 3.2* are those obtained from the best fit of thermal conductivity for the undoped sample. Note that the same Grüneisen parameter is assumed for the T1 and T2 phonon modes. Another parameter which should be carefully chosen for a proper fitting of the thermal conductivity data is the Debye temperature. As pointed out by Morelli *et al*. the calculation of the Debye temperature from the specific heat or from the acoustic phonon velocities results in a significant overestimation.[29] Since the heat is carried by acoustic phonons with frequency up to the maximum frequency at the zone boundary, ω_s^{max}, the correct Debye temperature to be used in Equations (2.26) and (2.31) is given by $\theta_D^s = \hbar\omega_s^{max}/k_B$. The Debye temperatures for the longitudinal and transverse phonons, θ_D^L, θ_D^{T1}, and θ_D^{T2} were calculated from the zone boundary frequencies along Γ-M and Γ-K directions of the Brillouin zone as measured by inelastic x-ray scattering.[34] The phonon velocities were determined from the experimental elastic constants in bulk HVPE grown GaN.[35]

For the phonon-point-defect scattering, substitutional Si and C on Ga sites, substitutional O on N sites, and Ga vacancies were considered. The atomic mass of the impurities (listed in atomic mass units in *Table 3.2*) were estimated with by considering the natural abundance of the corresponding isotopes.[36-38] The average nearest-neighbor atomic radius, R, and the average displacement in the host lattice due to the impurity (vacancy), ΔR_i, were calculated from the average bond length in a relaxed lattice.[39-41] In the treatment of the phonon-dislocation scattering we assumed a random orientation of the dislocation lines with respect to the temperature gradient, such that $\eta = 0.55$, and an equal density of screw and edge dislocations, so $N_S = N_E = N_D/2$.[42] From the elastic constants of GaN, the parameter P_E was estimated to be 1.1.[35] For the phonon-free-electron scattering the Fermi-level energy E_F at each temperature was calculated from the measured free electron concentration by an analytical approximation of the Fermi-Dirac integral.[43] An isotropic electron effective mass of $m_e = 0.23m_o$ was used, where m_o is the free electron mass.[44] The electron-acoustic phonon deformation potential was taken as $E_1 = 9.1$ eV.[45]

To test the model and the fitting procedure we first analyze the thermal conductivity data reported by Slack et al. using the steady-state heat flow method for thermal conductivity measurements of undoped free-standing GaN sample grown by HVPE.[46] The residual impurity concentration (Si and O) and the threading dislocation density in this sample were $\sim 10^{16}$ cm^{-3} and $\sim 10^{6}$ cm^{-2}, respectively. In other words, the sample is similar to our undoped sample. The experimental data and the fitted curves are shown in *Figure 3.4*. Two models with different forms of the normal phonon-phonon scattering rate are applied. In the first model, called the low-temperature (LT) model, $(a, b) = (2, 3)$ for LA phonons and $(a, b) = (1,$

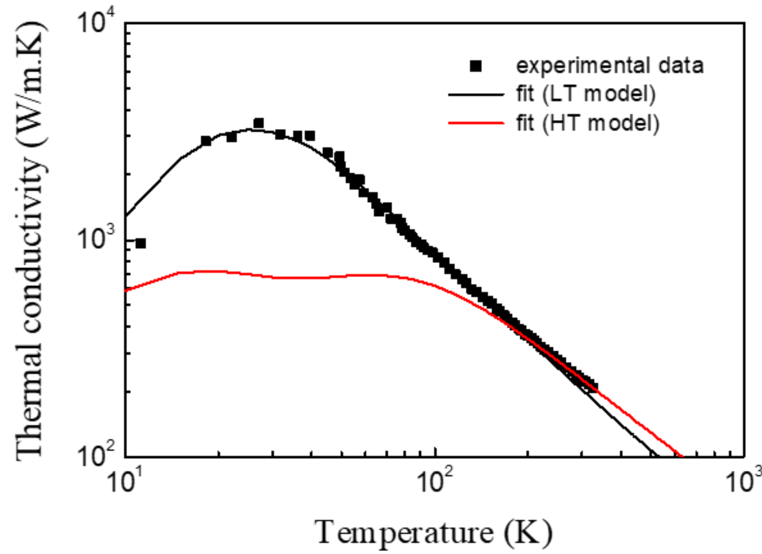

Figure 3.4 *Experimental data (symbols) for the thermal conductivity of an undoped HVPE grown GaN sample from the work of Slack et. al.*[46] *together with the best fit using the LT (black line) and HT (red line) forms for N-scattering rate.*

4) for TA phonons was used in Equation (2.30) for the *N*-scattering rate. In the second model, called the high temperature (HT) model, $(a, b) = (2, 1)$ and $(a, b) = (1, 1)$ were used for LA and TA phonons, respectively. The best fit over the entire temperature range (10-325 K) is obtained by the LT model with Grüneisen parameters $\gamma_L = 0.9$ and $\gamma_T = 0.65$. We note that the same experimental data analyzed by the Callaway model including only *N*-, *U*-, *I*- and *B*-scattering contributions and $\gamma_L = 1.0$ and $\gamma_T = 0.7$ were extracted from the fit.[29] The small difference in the Grüneisen parameters can be attributed to the slightly different phonon velocities used in Ref. 29. As seen in *Figure 3.4*, the LT model underestimates the thermal conductivity at $T > 250$ K. In this temperature region, a more satisfactory fit (using the same Grüneisen parameters) is achieved by the HT model. At lower temperatures,

however, the HT model is obviously inappropriate. These results indicate that for the analysis of thermal conductivity data in our samples, which were measured at temperatures above 295 K, the HT form for the *N*-scattering rate should be used.

The best fit of the experimental data for undoped sample (*Figure 3.3(a)*) yields Grüneisen parameters $\gamma_L = 0.8$ and $\gamma_T = 0.61$. Using these values the temperature dependence of the thermal conductivity for the other four samples is calculated by the model described in Chapter 2. Only the Si concentration (fractional concentration f_{Si} in Equation (2.37)), and the free electron concentration (Fermi-level energy in Equation (2.40)) are varied. *Figure 3.3(a)* shows that the calculated thermal conductivity of the low doped sample (7.3x10^{16} cm^{-3}) matches the experimental data well. The difference between the two curves is quite small which is not surprising given that a small amount of impurities and free carriers are not expected to significantly disturb the phonon propagation. In fact, the best fit of the data for the low doped sample (7.3x10^{16} cm^{-3}) gives the same Grüneisen parameters. For the moderately doped sample (1x10^{18} cm^{-3}), the correspondence between the calculated and measured thermal conductivity is also rather good, as seen in *Figure 3.3(b)*. With increasing doping, however, the simulated curves deviate from the experimental data especially at higher temperatures. For the highest doped sample (7x10^{18} cm^{-3}), the calculations underestimate the measured thermal conductivity in the entire temperature range considered. In order to provide a better match, we attempted to fit the data for the samples with the highest doping (3.5x10^{18} cm^{-3} and 7x10^{18} cm^{-3}) in order to find new Grüneisen parameters. For example, the *k* values measured near the room temperature (290-310 K) for the highest doped (7x10^{18} cm^{-3})can be reproduced by a slight reduction of γ_L or γ_T. Nevertheless, for

both samples it was impossible to reach a satisfactory fit of the experimental temperature dependence. The experimental results clearly show that the higher the doping, the weaker the temperature dependence. In other words, the decrease in *k* with increasing temperature becomes smaller. As seen in *Figure 3.3(b)* the thermal conductivity of the highest doped sample is higher than that in lower doped samples at temperatures above 330 K. The calculations also indicate a change in the temperature dependence with Si concentration, but at each temperature the thermal conductivity is found to decrease monotonically with increasing doping.

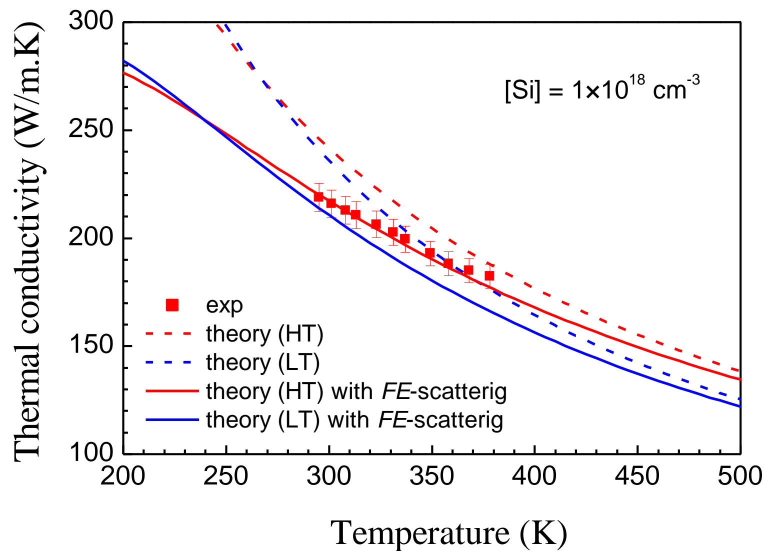

Figure 3.5 *Comparison of the different models for the thermal conductivity of the moderately doped sample ($1x10^{18}$ cm^{-3}). The best match with the experimental data is obtained for the model with the high temperature (HT) form of the N-scattering and the inclusion of the FE-scattering.*

Following the Callaway model, the change in the strength of a particular phonon scattering process cannot entirely explain the change in the behavior of the thermal conductivity with temperature. It is likely that the peculiarity of the temperature dependence is a result of the specific interplay between different scattering processes. In our analysis of the effect of Si doping on the thermal conductivity of GaN, only the rates for *PD*- and *FE*-scattering are varied. We have further studied the role of the *FE*-scattering in more details. *Figure 3.5* shows the experimental data for the moderately doped sample (1×10^{18} cm^{-3}) together with the thermal conductivity calculated with and without accounting for the *FE*-scattering. It is clear that in both cases, the model with the LT form of the *N*-scattering rate fails to reproduce the slope of the temperature dependence of k. The best match with the experimental data is observed when the HT form of the *N*-scattering rate is used and the *FE*-scattering is included. The omission the *FE*-scattering leads to an overestimation of k in the entire temperature region.

The thermal conductivity as a function of the Si doping at different temperatures is presented in *Figure 3.6*. It is again evident that the inclusion of the *FE*-scattering in the model is indispensable for a proper explanation of the experimental data at T = 300-350K. Above 350 K, however, the contribution of the *FE*-scattering seems to decrease as seen by the proximity of the two simulated curves. At higher temperatures, the thermal conductivity is predicted to be independent of Si concentration up to [Si] ~ 1×10^{18} cm^{-3}, while at room temperature k is only independent on Si concentration up to [Si] ~ 5×10^{16} cm^{-3}. The trend of the room temperature thermal conductivity show in *Figure 3.6* is generally consistent with previously reported data for thin Si doped GaN layers residing on sapphire.[6] However, all the

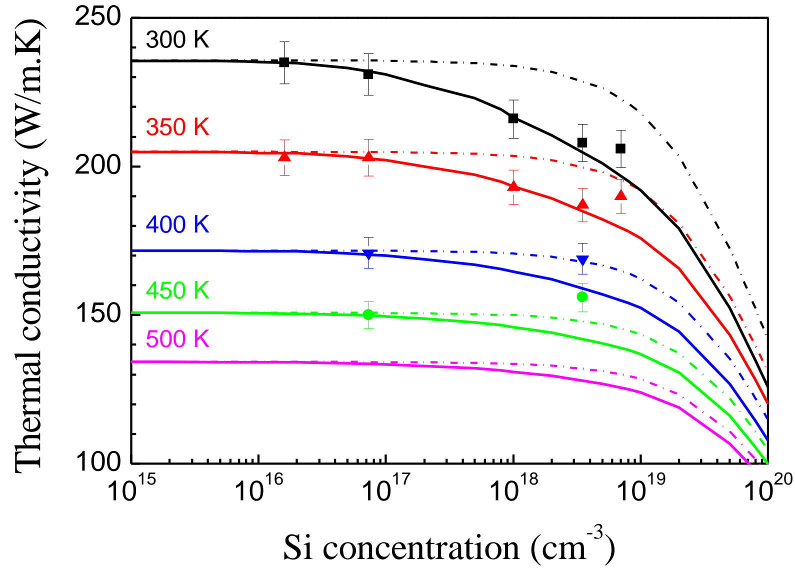

Figure 3.6 *Thermal conductivity of bulk GaN as a function of Si concentration at different temperatures. The experimental values (symbols) and the theoretical dependences calculated with (solid lines) and without (dot-dashed lines) including the FE-scattering are shown.*

values measured here were significantly higher due to the fact that the bulk GaN is of much better quality in terms of the structural defect density as compared to the thin heteroepitaxial GaN layers.

Although we were able to successfully model both the temperature dependence of *k* at low and to moderate doping levels and the Si concentration dependence of *k* at temperatures up to 350 K, the discrepancy at higher temperatures and higher doping remains puzzling. The discrepancy could be attributed to some shortcomings of the Callaway model, such as the simple Debye-like phonon dispersion or the independence of the phonon modes. In that case, however, one would also expect a discrepancy in the model for undoped materials, which is not seen here, nor was in previous studies.[29,30] Since the strength of the *PD*-scattering

increases with increasing Si concentration the thermal conductivity should gradually decrease independent of the temperature. Therefore, it is most likely the *FE*-scattering and its handling in the model are responsible for the deviation between the calculated and the measured thermal conductivity values well above room temperature. Ziman has showed that at higher temperatures the number of electrons available for scattering with phonons decreases due to the requirement for energy and momentum conservation, which means that the contribution of the *FE*-scattering to the thermal conductivity will diminish with increasing temperatures.[47,48] This effect is accounted for in Equations (3.1) and (3.2), but it is likely that the temperature dependence is not covered precisely because of the simplified treatment of the problem.[47] Another plausible explanation for the weaker temperature dependence of thermal conductivity at higher temperatures and doping levers is the role of the free electrons in the heat transport which is not considered in the model. The electronic thermal conductivity was estimated to contribute to the total room temperature thermal conductivity of GaN at free carrier densities above 1×10^{18} cm^{-3}.[49] These estimates have been done for a material with dislocation density > 5×10^{8} cm^{-2}, where a strong electron-dislocation scattering contribution is present. However, in the bulk GaN samples measured here the dislocation density is at least two orders of magnitude lower and one can expect a larger contribution of the electronic thermal conductivity especially above room temperature.

Additional insight into the dominant scattering processes above room temperature can be obtained from a simple power law fit from Equation (3.1). Here k_o is the thermal conductivity at room temperature and T_o = 295 K. This empirical fit could be useful for

thermal management and device design since it predicts the thermal conductivity behavior both at different temperatures and different doping levels, which can be seen in *Figure 3.7*.

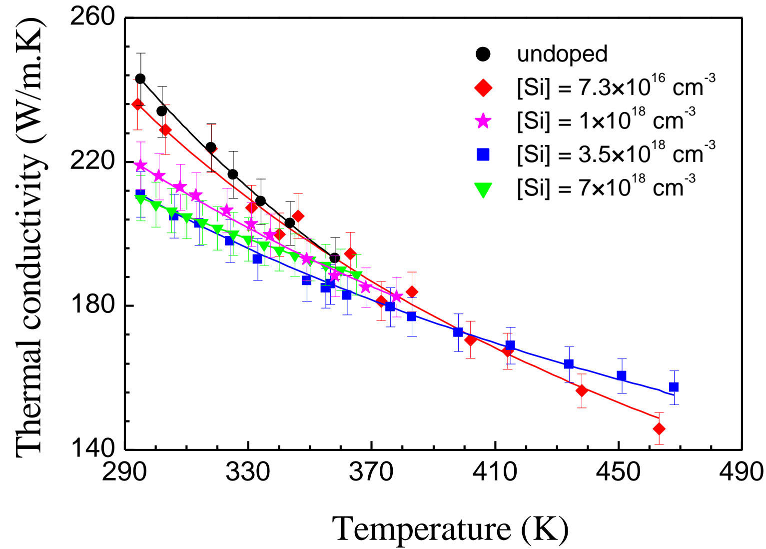

Figure 3.7 *Temperature dependence of the thermal conductivity for all measured samples. The solid lines represent the experimental data fit by Equation 3.1.*

The variation of the slope, α, with the Si concentration is depicted in *Figure 3.8*. It is found that the slope gradually decreases with increasing doping from α = 1.3 for the undoped sample to α = 0.55 for the highest doped sample. The slope found for the undoped sample is consistent with previously reported numbers for high quality HVPE grown GaN – 1.43 and 1.22.[10,29] It is generally assumed that at high temperatures (above the Debye temperature) the thermal conductivity is determined by the Umklapp phonon-phonon scattering and the k is expected to vary as ~ 1/T .[50] At these temperatures, the contribution of all resistive scattering processes related to imperfections (I-, PD-, and D-scattering) is

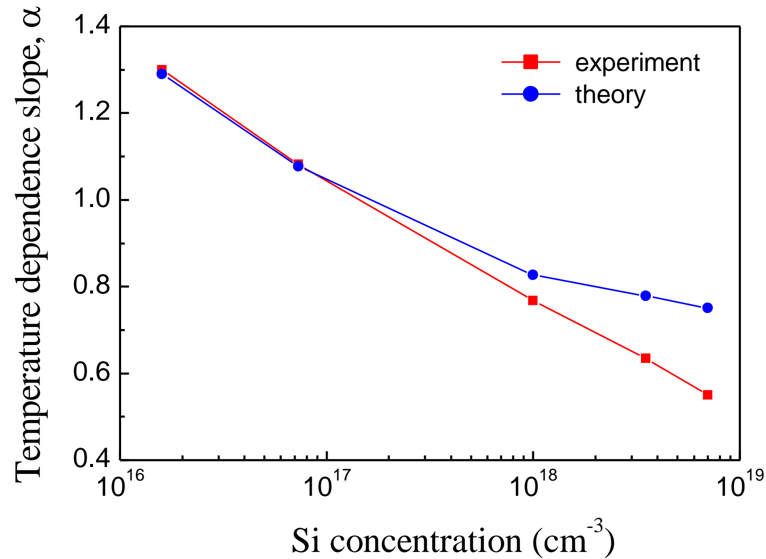

Figure 3.8 *The slope of the temperature dependence in Equation 3.1 of the thermal conductivity as a function of Si concentration.*

independent of the temperature.[50] However, the Debye temperatures of GaN for longitudinal (439 K) and transverse (310 K) acoustic phonons are within the temperature range considered here. Thus, the above simple approximation does not hold. Moreover, as it is evident from *Figures 3.5* and *3.6*, the role of the N-scattering is not negligible. This effect can offer an explanation for the deduced $\alpha > 1$ for undoped GaN. The decrease in the slope with increasing Si concentration suggests an increasing contribution from the PD- and FE-scattering processes. It is worth noting that below the Debye temperature the thermal conductivity related to the PD- and FE-scattering varies as $\sim 1/T$ and $\sim T^2$, respectively.[50] A similar behavior of the temperature dependence slope above room temperature has been observed for the thermal conductivity of n- and p-type 6H SiC.[51] *Figure 3.8* also shows the temperature dependence slope extracted from the calculated thermal conductivity. The

deviation from the values determined from the experimental temperature dependence at high Si concentration can be attributed to the overestimation of the FE-scattering and the neglecting of the electronic thermal conductivity as discussed above.

3.4. Conclusions

The thermal conductivity of n-type GaN, including both unintentionally and intentionally doped samples, was measured using the 3ω method. Two bulk GaN samples grown by HVPE and a mixed ammonothermal growth technique had room temperature thermal conductivities of 265 and 279 W/mK respectivity. The large magnitudes of thermal conductivity were attributed to the low dislocation density in material. Temperature dependence of thermal conductivity measurements determined near ideal values for the power law slopes of 1.38 and 1.40, respectively. These values were compared to that of an AlN sample that had a smaller slope of 1.11, despite having a lower dislocation density of $5x10^3$ cm^{-2}. The low value of slope for the AlN compared to GaN was hypothesized to be caused by other defects causing more complex scattering mechanisms, which is much more difficult to control in AlN at this point.

The thermal conductivity of HVPE grown bulk GaN with varying Si doping concentration was measured in the temperature interval of 295-470 K. It was found that the thermal conductivity decreases with both increasing temperature and increasing Si concentration. The experimental data was analyzed by use of a modified Callaway model which included all relevant phonon scattering mechanisms. From the fit of the experimental data for an undoped sample, Grüneisen parameters for acoustic phonons were extracted and then used for calculation of the thermal conductivity in the doped samples. A very good

correlation between the simulations and the experiment was found for Si concentration up to 1×10^{18} cm^{-3}. It was shown that for a proper explanation of the measured data the phonon-free-electron scattering was necessary to include in the model. At higher doping levels, the model underestimated the thermal conductivity, especially at higher temperatures. The discrepancy was attributed to the electronic thermal conductivity which appears to contribute essentially to the total thermal conductivity in addition to the lattice thermal conductivity especially at higher doping and higher temperatures. The slope of the temperature dependence of the thermal conductivity gradually decreases with the increasing Si doping. It was found that at $T > 350$ K the thermal conductivity in the highest doped sample (7×10^{18} cm^{-3}) was higher than that in lower doped samples. This result could be of particular importance for thermal management of devices grown on *n*-type substrates and operating at high power and elevated temperatures.

References

1 M. Slomski, L. Liu, J. F. Muth, and T. Paskova, Growth Technology for GaN, AlN Bulk Substrates and Templates, in Handbook of GaN Semiconductor Materials and Devices, (in press 2017).

2 P. Paskov, M. Slomski, J. H. Leach, J. F. Muth, and T. Paskova, Effect of Si doping on the thermal conductivity of bulk GaN at elevated temperatures, J. Appl. Phys. (submitted 2017)

3 M. Slomski, P. P. Paskov, J. H. Leach, J. F. Muth, and T. Paskova, Thermal conductivity of bulk GaN grown by HVPE: Effect of Si doping, Physica Status Solidi (B)1600713 (2017).

4 G. A. Slack, Nonmetallic crystals with high thermal conductivity, Journal of Physics and Chemistry of Solids 34, 321 (1973).

5 D. I. Florescu, V. M. Asnin, F. H. Pollak, R. J. Molnar, and C. E. C. Wood, High spatial resolution thermal conductivity and Raman spectroscopy investigation of hydride vapor phase epitaxy grown n-GaN/sapphire (0001): Doping dependence, Journal of Applied Physics 88, 3295 (2000).

6 J. Zou, D. Kotchetkov, A. A. Balandin, D. I. Florescu, and F. H. Pollak, Thermal conductivity of GaN films: Effects of impurities and dislocations, Journal of Applied Physics 92, 2534 (2002).

7 D. Kotchetkov, J. Zou, A. A. Balandin, D. I. Florescu, and F. H. Pollak, Effect of dislocations on thermal conductivity of GaN layers, Applied Physics Letters 79, 4316 (2001).

8 G. A. Slack, L. J. Schowalter, D. Morelli, and J. A. Freitas, Some effects of oxygen impurities on AlN and GaN, Journal of Crystal Growth 246, 287 (2002).

9 T. Paskova, and K. R. Evans, GaN Substrates-Progress, Status, and Prospects, Jstqe 15, 1041 (2009).

10 C. Mion, J. F. Muth, E. A. Preble, and D. Hanser, Accurate dependence of gallium nitride thermal conductivity on dislocation density, Applied Physics Letters 89, 92123 (2006).

11 E. Richter, M. Gründer, B. Schineller, F. Brunner, U. Zeimer, C. Netzel, M. Weyers, and G. Tränkle, GaN boules grown by high rate HVPE, Physica Status Solidi (C) 8, 1450 (2011).

12 H. Nagaoka, K. Shimoyama, H. Shibata, Y. Waseda, and K. Kiyomi, U.S. Patent No. US2009081110A1 (Mar 26, 2009).

13 L. Lindsay, D. A. Broido, and T. L. Reinecke, Thermal conductivity and large isotope effect in GaN from first principles, Physical Review Letters 109, 095901 (2012).

14 A. Witek, Some aspects of thermal conductivity of isotopically pure diamond a comparison with nitrides, Diamond and Related Materials 7, 962 (1997).

15 G. A. Slack, Nonmetallic crystals with high thermal conductivity, Journal of Physics and Chemistry of Solids 34, 321 (1973).

16 V. M. Asnin, F. H. Pollak, J. Ramer, M. Schurman, and I. Ferguson, High spatial resolution thermal conductivity of lateral epitaxial overgrown GaN/sapphire (0001) using a scanning thermal microscope, Applied Physics Letters 75, 1240 (1999).

17 G. A. Slack, R. A. Tanzilli, R. O. Pohl, and J. W. Vandersande, The intrinsic thermal conductivity of AlN, Journal of Physical Chemical Solids 48, 641 (1987).

18 K. Jagannadham, E. A. Berkman, and N. Elmasry, Thermal conductivity of semi-insulating, p -type, and n -type GaN films on sapphire, Journal of Vacuum Science & Technology A 26, 375 (2008).

19 A. Jezowski, O. Churiukova, J. Mucha, T. Suski, I. A. Obukhov, and B. A. Danilchenko, Thermal conductivity of heavily doped bulk crystals GaN:O. Free carriers contribution, Materials Research Express 2, 085902 (2015).

20 R. B. Simon, J. Anaya, and M. Kuball, Thermal conductivity of bulk GaN—Effects of oxygen, magnesium doping, and strain field compensation, Applied Physics Letters 105, 202105 (2014).

21 T. Paskova, E. A. Preble, A. D. Hanser, K. R. Evans, R. Kröger, P. P. Paskov, A. J. Cheng, M. Park, J. A. Grenko, and M. A. L. Johnson, Polar and nonpolar HVPE GaN substrates: impact of doping on the structural, electrical and optical characteristics, Physica Status Solidi (C) 6, (2009).

22 D. G. Cahill, Thermal conductivity measurement from 30 to 750 K: the 3ω method, Rev. Sci. Inst. 61, 802 (1990).

23 W. Li, and N. Mingo, Thermal conductivity of bulk and nanowire InAs, AlN, and BeO polymorphs from first principles, Journal of Applied Physics 114, 183505 (2013).

24 J. C. Rojo, L. J. Schowalter, K. Morgan, D. I. Florescu, F. H. Pollak, B. Ragothamachar, and M. Dudley, Single crystal AlN substrate preparation from bulk crystals, Materials Reseach Symposium Proceedings 680, (2001).

25 J. Callaway, Model for Lattice Thermal Conductivity at Low Temperatures, Physical Review 113, 1046 (1959).

26 M. G. Holland, Analysis of Lattice Thermal Conductivity, Physical Review 132, 2461 (1963).

27 M. Asen-Palmer, K. Bartkowski, E. Gmelin, M. Cardona, A. P. Zhernov, A. V. Inyushkin, A. Taldenkov, V. I. Ozhogin, K. M. Itoh, and E. E. Haller, Thermal conductivity of germanium crystals with different isotopic compositions, Physical Review B 56, 9431 (1997).

28 R. B. Simon, J. Anaya, and M. Kuball, Thermal conductivity of bulk GaN—Effects of oxygen, magnesium doping, and strain field compensation, Applied Physics Letters 105, 202105 (2014).

29 D. T. Morelli, J. P. Heremans, and G. A. Slack, Estimation of the isotope effect on the lattice thermal conductivity of group IV and group III-V semiconductors, Physical Review B 66, (2002).

30 M. D. Kamatagi, N. S. Sankeshwar, and B. G. Mulimani, Thermal conductivity of GaN, Diamond & Related Materials 16, 98 (2007).

31 A. AlShaikhi, S. Barman, and G. P. Srivastava, Theory of the lattice thermal conductivity in bulk and films of GaN, Physical Review B 81, (2010).

32 M. Lopuszynski, and J. A. Majewski, Ab initio calculations of third-order elastic constants and related properties for selected semiconductors, Physical Review B 76, 04502 (2007).

33 H. Iwanaga, A. Kunishige, and S. Takeuchi, Anisotropic thermal expansion in wurtzite-type crystals, Journal of Materials Science 35, 2451 (2000).

34 T. Ruf, J. Serrano, M. Cardona, P. Pavone, M. Pabst, M. Krisch, M. D'Astuto, T. Suski, I. Grzegory, and M. Leszczynski, Phonon dispersion curves in wurtzite-structure GaN determined by inelastic x-ray scattering, Physical Review Letters 86, 906 (2001).

35 M. Hirao, H. Ogi, and N. Nakamura, Elastic, anelastic, and piezoelectric coefficients of GaN, Journal of Applied Physics 111, (2012).

36 K. J. R. Rosman, and P. D. P. Taylor, Isotopic compositions of the elements 1997 (Technical Report), Pure and Applied Chemistry 70, 217 (1998).

37 G. Audi, and A. H. Wapstra, The 1993 atomic mass evaluation, Nuclear Physics, Section A 565, 1 (1993).

38 G. Audi, and A. H. Wapstra, The 1995 update to the atomic mass evaluation, Nuclear Physics, Section A 595, 409 (1995).

39 C. Van de Walle, Effects of impurities on the lattice parameters of GaN, Physical Review B 68, 165209 (2003).

40 J. Lyons, C. Van de Walle, and A. Janotti, Carbon impurities and the yellow luminescence in GaN, Applied Physics Letters 97, (2010).

41 J. Neugebauer, and Van de Walle, Chris G, Gallium vacancies and the yellow luminescence in GaN, Applied Physics Letters 69, 503 (1996).

42 P. G. Klemens, The Scattering of Low-Frequency Lattice Waves by Static Imperfections, Proceedings of the Physical Society. Section A 68, 1113 (1955).

43 V. C. Aguilera-Navarro, G. A. Estévez, and A. Kostecki, A note on the Fermi–Dirac integral function, Journal of Applied Physics 63, 2848 (1988).

44 M. Feneberg, K. Lange, C. Lidig, M. Wieneke, H. Witte, J. Bläsing, A. Dadgar, A. Krost, and R. Goldhahn, Anisotropy of effective electron masses in highly doped nonpolar GaN, Applied Physics Letters 103, 232104 (2013).

45 W. Knap, E. Borovitskaya, M. S. Shur, L. Hsu, W. Walukiewicz, E. Frayssinet, P. Lorenzini, N. Grandjean, C. Skierbiszewski, P. Prystawko, M. Leszczynski, and I. Grzegory, Acoustic phonon scattering of two-dimensional electrons in GaN/AlGaN heterostructures, Applied Physics Letters 80, 1228 (2002).

46 G. A. Slack, L. J. Schowalter, D. Morelli, and J. A. Freitas, Some effects of oxygen impurities on AlN and GaN, Journal of Crystal Growth 246, 287 (2002).

47 J. M. Ziman, The Effect of Free Electrons on Lattice Conduction, Philosophical Magazine 1, 191 (1956).

48 J. M. Ziman, The effect of free electrons on lattice conduction, Philosophical Magazine 2, 292 (1957).

49 W. Liu, and A. Balandin, Thermal conduction in Al x Ga 1 − x N alloys and thin films, Journal of Applied Physics 97, (2005).

50 P. G. Klemens, Thermal Conductivity and Lattice Vibrational Modes, 1 (1958).

51 E. A. Burgemeister, W. von Muench, and E. Pettenpaul, Thermal conductivity and electrical properties of 6H silicon carbide, Journal of Applied Physics 50, 5790 (1979).

4. Thermal conductivity of semi-insulating GaN

The effect of Fe-doping on the thermal conductivity of bulk GaN is examined by use of the 3ω method in order evaluate how the modulation of the electrical resistivity affects the thermal properties. Semi-insulating material was obtained by intentionally introducing Fe dopants into HVPE grown bulk GaN at concentrations ranging from 1.5×10^{16} - 1.8×10^{18} cm^{-3}. At room temperature, the thermal conductivity was found to decrease from a maximum of 240 W/mK for the unintentionally doped sample to 194 W/mK for the sample with the highest Fe concentration. Elevated temperature thermal conductivity measurements from 295-375 K revealed a decrease in thermal conductivity with increasing temperature that was described by a simple power law. The slope of the power law was found to quickly deviate from the ideal $T^{-1.5}$ dependence with moderate Fe concentration, which was explained by increased phonon-impurity scattering.

4.1. Introduction

The unintentional intrinsic *n*-type character of GaN has been shown to be advantageous for many applications, however many other applications require GaN to be electrically insulating. High electron mobility transistors (HEMTs) and other lateral conduction devices require semi-insulating material beneath the device structure to allow for sharp current pinch-off and to confine the current into the 2D electron gas layer.[1-3] A recent HEMT device demonstrated a breakdown voltage of 800 V by introducing carbon to the GaN layer.[3] Similarly, vertical structures use semi-insulating material to confine current flow. AlGaN/GaN current aperture vertical electron transistors have been demonstrated with

maximum source-drain current densities of 750 mA/mm.[4] For these devices, a semi-insulating layer of Mg-doped GaN was necessary to form the current aperture in the device. Semi-insulating bulk GaN also shows benefits for high-frequency applications, as conductive GaN has been shown to limit the frequency that devices are able to operate.[5] While many nitride based devices have been proven operational even in presence of high dislocation density, high-power nitride devices would benefit when higher quality material with lower dislocation density is used. Device structures grown on native nitride substrates have been repeatedly reported to possess much higher crystalline quality and dislocation density lower by several orders of magnitude as compared to device structures grown on foreign substrates with large mismatch such as SiC and sapphire. Hydride Phase Vapor Epitaxy (HVPE) is currently one of the primary methods used for growing bulk GaN substrates, owing to the high crystalline quality obtained, growth rate, cost, and ease of introducing dopants.[6,7] Typically, undoped GaN grown by HVPE has unintentional *n*-type conductivity due to residual O and Si impurities which act as donors; we will therefore refer to undoped GaN as unintentionally doped. These O and Si impurities are introduced to the lattice from the quartz tubing or the precursor gases. To obtain semi-insulating material, the donors in unintentionally doped GaN need to be compensated. The *n*-type dopants are often compensated by using deep acceptors such as Fe[5,8,9] or Mg[4].

While the electrical transport and impurity charge state of Fe impurities in GaN has been extensively evaluated and reported in the literature,[10-12] its impact on the thermal conductivity has not been studied in detail. Since these semi-insulating layers are found in devices for high-power applications, self-heating from large currents becomes a factor and

thermal management in the device needs to be taken into consideration. One of the greater advantages of GaN is its relatively large thermal conductivity compared to classical semiconductors. Theoretical predictions by Witek show the maximum thermal conductivity for pure unintentionally doped GaN to be 410 W/mK.[13] The first reports on the thermal conductivity of unintentionally doped GaN grown on non-native substrates such as sapphire were found to be much lower, in the range of 110-170 W/mK.[14,15] The latter is not surprising, considering GaN layers grown on non-native substrates typically have dislocation densities in the 10^{9}-10^{10} cm^{-3} range; which has been shown to limit the max thermal conductivity by a large contribution of phonon-dislocation scattering. Later, Mion et al. found that lowering the dislocation density greatly improves the thermal conductivity of GaN for dislocation densities down to 10^{6} cm^{-3}.[16] In our recent work on the thermal conductivity of Si-doped HVPE GaN, we found a thermal conductivity of 245 W/mK for an unintentionally doped sample with dislocation density of 5×10^{6} cm^{-2}.[17] For another unintentionally doped GaN sample grown by HVPE on an ammonothermal seed with dislocation density of ~5×10^{4} cm^{-3}, we measured thermal conductivity as high as 270 W/mK.[7]

In the literature, there are few reports on the effect of semi-insulating dopants on the thermal conductivity of bulk GaN. In a recent work by Simon et al., ammonothermal GaN samples with O doping and semi-insulating samples with Mg-O compensated doping were examined.[18] A comparative analysis of the O-doped sample, an unintentionally doped sample, and the semi-insulating sample revealed the highest thermal conductivity of 230 W/mK in the semi insulating material despite having larger impurity concentration than other samples. The only study of the thermal conductivity of Fe-doped bulk GaN grown by HVPE

reported thermal conductivity of 230 W/mK for a sample with dislocation density of 5×10^{6} cm^{-3}.[16]

To the best of our knowledge, there are no reports on the variation of dopant concentration on the thermal conductivity of GaN at elevated temperatures for any semi-insulating dopant. In this work, we present a systematic study of the effect of Fe doping on thermal conductivity for dopant concentration varying in the rage of 1.5×10^{16} - 1.8×10^{18} cm^{-3}. We also present temperature dependence of thermal conductivity at elevated temperatures obtained by the 3ω method.

4.2. Experimental details

4.2.1. Sample growth

The GaN samples studied here were grown in a vertical HVPE reactor at Kyma Technologies, Inc. The layers were grown at substrate temperatures of approximately 1000°C on (0001) sapphire and were self-separated from the substrate during cool-down. The GaN growth rate of the layers was 150 μm/h. Doping was ensured by introducing Bis-(cyclopentadienyl) iron (Cp_2Fe) source with a N_2 carrier gas, varying the Fe flow in the range of (20 - 500) sccm. While the typical dimensions of the thick layers vary in wide range, up to 2-inch wafers were obtained. The samples selected for our study had lateral dimensions of around 5mm × 10mm due to sample holder restrictions for the temperature dependence measurements. All samples in this study were as-grown material with thickness about 1mm.

4.2.2. Sample characterization

High-resolution x-ray diffraction (HR-XRD) and reciprocal space mapping were used for determining the values for the rocking curve full widths at half maximum (FWHM). The

FWHM of both the symmetric (002) and the asymmetric (105) reflections were determined to be as low as 110-160 arcsec for all Fe doped samples, indicating high crystalline quality, small curvature and low-defect density independent of the doping level. The dislocation density was determined to be in the range of 5×10^{5} - 5×10^{6} cm^{-2} by using either transmission electron microscopy (TEM) or etch pit density (EPD) for representative samples.

The impurity concentrations of all the samples were determined by secondary ion mass spectroscopy (SIMS) measurements. A representative SIMS profile in near surface region (4 µm depth) of the unintentionally doped sample is shown in *Figure 4.1*. The SIMS

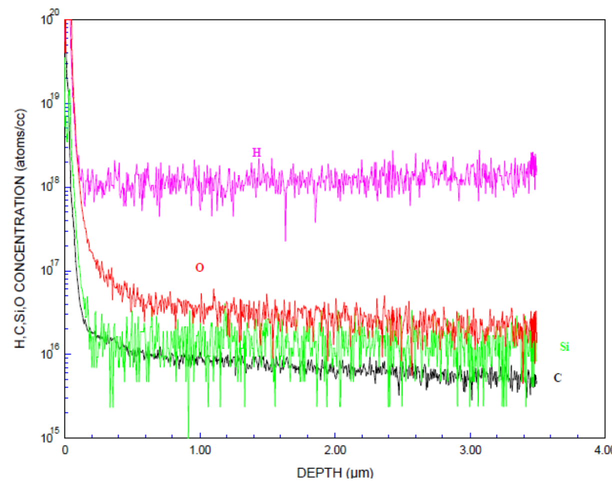

Figure 4.1 *SIMS profile of the undoped sample showing concentrations of H (purple line), O (red line), Si (green line), and C (black line).*

data revealed residual O, Si and H impurities with typical concentrations of [O] ≈ 3×10^{16} cm^{-3}, [Si] ≈ 1.5×10^{16} cm^{-3} and [H] ≈ 1×10^{18} cm^{-3} in all the samples. The Fe concentration was found in the range 1.6×10^{15} – 3.5×10^{18} cm^{-3} for Fe flows from 0 to 500 sccm, as seen in

Figure 4.2. A good consistency of the Fe concentration with the SIMS and electron paramagnetic resonance (EPR) measurements can be seen.

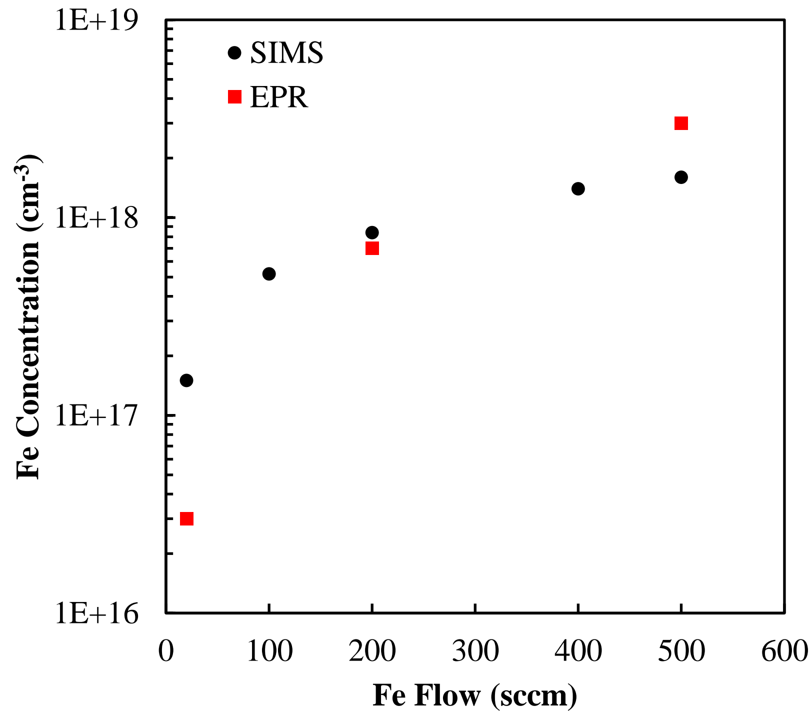

Figure 4.2 *Fe concentration as determined by SIMS (black circles) and EPR (red squares) for a given Fe flow rate in HVPE growth.*

4.2.3. 3ω measurement details

Thermal conductivity was measured using the 3ω method as described by Cahill.[19] In the 3ω method, a thin metal heater line is deposited onto the surface which is used as both a heat source and a thermometer for thermal analysis. The dimensions for the heater/thermometer lines used in this experiment were a width of 6μm, a length of 3 mm, and thickness of 200 nm. The metal for the heater/thermometer was chosen to be Au due to its

high temperature coefficient of resistivity and inert behavior. Indium dots were used in between the gold pads and the spring-loaded pins in order to make rigid connections to the equipment. An SiO_2 insulation layer with thickness of 200 nm was grown via plasma enhanced chemical vapor deposition (PECVD) to isolate the metal heater/thermometer from underlying material. The purpose of the SiO_2 layer was two-fold: (i) to provide constant electrical isolation over the wide range of Fe doping concentrations which have large, yet finite resistivity, and (ii) to allow direct comparison to the unintentionally sample which required an isolation layer. All 3ω technique measurements in this study relied on the slope method, which relates the slope of the third harmonic voltage $V_{3\omega}$ vs the logarithm of angular frequency to the thermal conductivity. In order to obtain this slope, $V_{3\omega}$ is recorded while scanning over an input frequency range. The frequency range that can be used is directly related to the properties and dimensions of both the sample being measured and the heater/thermometer device. A valid frequency range gives thermal penetration depths that meet the boundary conditions of the slope method.[19,20] Due to the relatively large thickness (~1mm) of the samples measured, the third harmonic voltage was measured at a low frequency range of 50-800Hz. The linear relation of the third harmonic voltage and the logarithm of angular frequency for the Fe doped sample with concentration of 8.4×10^{17} cm^{-3} can be seen in *Figure 4.3* over the temperature range used in this study. The temperature was varied by the use of a hot plate with a thermally shielded cover and was measured using a thermocouple in intimate contact with the sample. Measurements of thermal conductivity were made from 295-375 K, the typical temperature range experienced by the Fe-doped material in high power applications were self-heating is a challenge. *Figure 4.3* also shows

that the slope method is valid in the frequency range selected for all temperatures measured in this study.

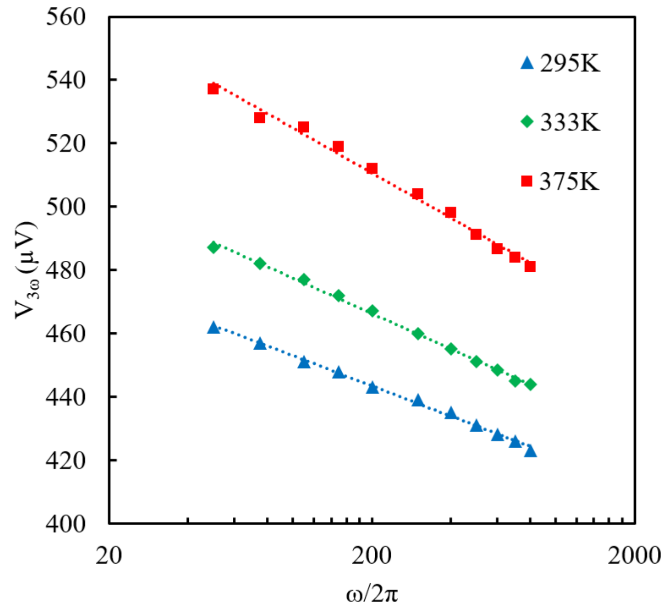

Figure 4.3 *Semi-log plot of $V_{3\omega}$ vs. $\omega/2\pi$ used to determine thermal conductivity in the temperature range of 295-375K.*

4.3. Results and discussion

The thermal conductivity was first determined at room temperature to evaluate the effect of Fe doping concentration. A comparison of the room temperature thermal conductivity of an undoped sample and four Fe doped samples with concentrations ranging from 1.5×10^{16} to 1.8×10^{18} cm^{-3} can be seen in *Figure 4.4*. The highest thermal conductivity was obtained for the unintentionally doped sample and was found to be K = 240 ± 5 W/mK. It can be seen that increasing the Fe concentration leads to a decrease in the thermal conductivity. Reduction to thermal conductivity at increasing temperatures is likely due to

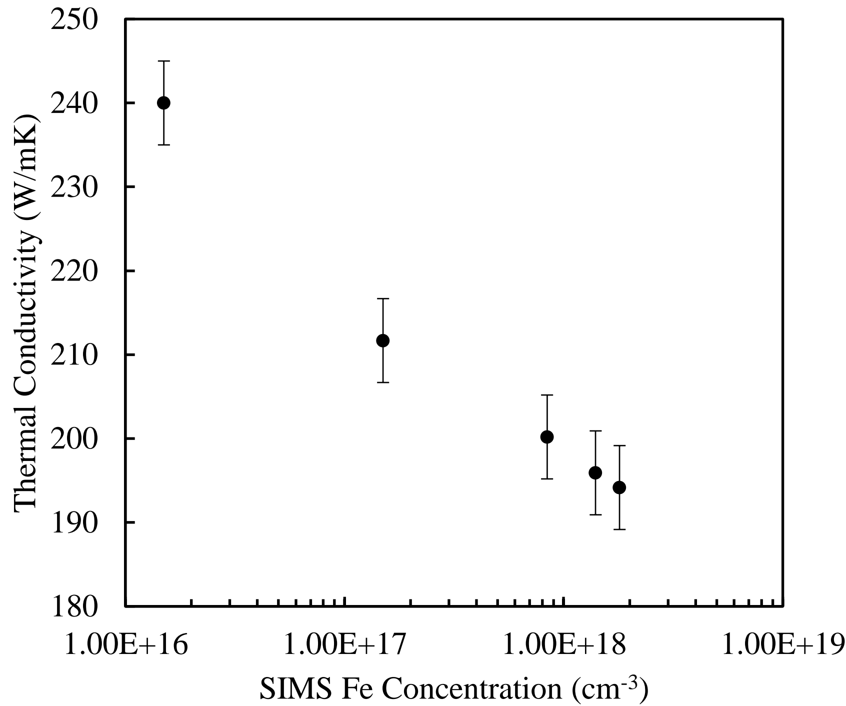

Figure 4.4 *Room temperature thermal conductivity vs. Fe concentration (as determined by SIMS) with +/-5W/mK experimental error.*

Umklapp phonon-phonon and phonon-impurity scattering. A large decrease in the thermal conductivity is seen with moderate (~$1x10^{17}$ cm^{-3}) additions of Fe dopants, and the reduction tapers off with a further increase in Fe concentration. While the strong reduction in the thermal conductivity with moderate additions of Fe dopants is not desirable from the application point of view, it is beneficial that the variation of additional impurities in order to modulate the electrical resistivity does not significantly deteriorate the relatively high thermal conductivity of semi-insulating GaN substrates.

Comparing the effect of Fe doping to the effect of Si doping on the thermal conductivity of GaN substrates, which we present separately,[17] it appears that the Fe impurity

has a noticeably less pronounced effect. The reduction in thermal conductivity for Si doping vs. Fe for otherwise similar samples (meaning similar dislocation and point defect density) can be explained by the Si impurities larger contribution to the phonon-impurity scattering, as well as an additional contribution from phonon-free electron scattering. In our previous work, it was found that the phonon-free-electron scattering played a significant role in the reduction of thermal conductivity at higher Si concentrations.[17] Due to the semi-insulating nature of these Fe doped samples, it is obvious that no phonon-free-electron scattering contribution is present to reduce the thermal conductivity.

A larger reduction in thermal conductivity occurs over all doping concentrations as the temperature increases. Above the room temperature the temperature dependence of the thermal conductivity can be fit with a power law fitting given by Equation (3.1). The slope of the fitting equation, α, determines the reduction in thermal conductivity with temperature. The value of α for unintentionally doped sample was 0.94; this value deviates from the value of 1.5 expected for high quality adamantine crystals above their Debye temperature. This undoped sample was chosen as a reference for the Fe-doped samples in this experiment as it was grown in the same reactor at the same thickness and dislocation density. The α value of 0.94 is lower than other undoped samples of higher crystalline quality measured in our work which showed a temperature dependence of thermal conductivity of 1.3.[17] As the Fe impurity concentration increased, the value of α was reduced to 0.69, 0.55, 0.55, and 0.54 for an Fe concentration of 1.5×10^{17} cm^{-3}, 8.4×10^{17} cm^{-3}, 1.4×10^{18} cm^{-3}, and 1.8×10^{18} cm^{-3}, respectively. It can be seen from the values of α that the temperature dependence quickly decreases with even small additions (1.5×10^{17} cm^{-3}) of Fe dopants. Increasing the Fe

concentration to above ~1x10^{18} cm^{-3} reduces the temperature dependence of thermal conductivity to a value that plateaus around 0.55 regardless of concentration. The temperature dependence of thermal conductivity with the corresponding power law fit can be seen in *Figure 4.5* for all doping concentrations. Over all Fe concentrations, it can be seen that the thermal conductivity decreases with increasing temperature. Extrapolation of the data shows that the thermal conductivity at all doping concentrations likely trends toward a common thermal conductivity value at higher temperatures independent of Fe concentration.

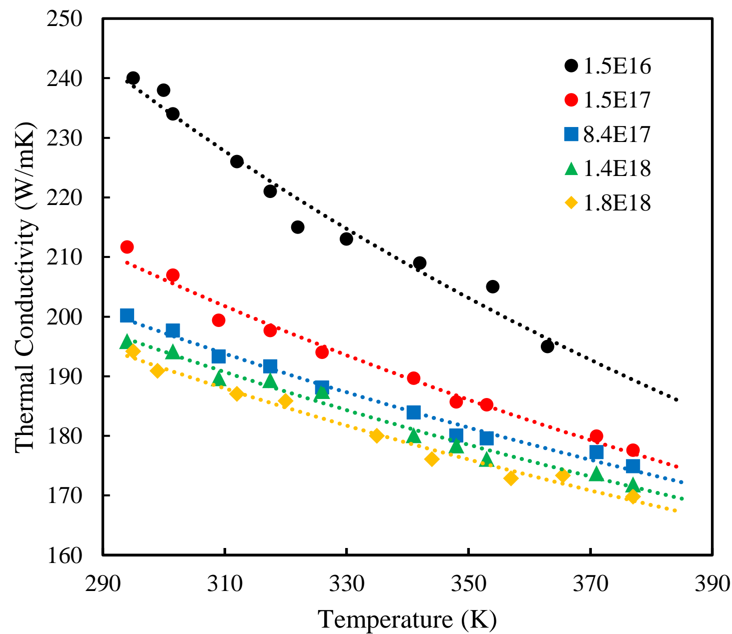

Figure 4.5 *Experimentally determined (points) temperature dependence of thermal conductivity for all Fe doping concentrations with power law fit (lines).*

In our previous publication on the effect of Si impurities on the thermal conductivity of *n*-type GaN, we used a modified Callaway model to describe temperature dependence.[17] A rigorous derivation of the modified Callaway model can be found in our previous

publication[21] and will not be presented here. In the modified Callaway model, scattering contributions from both normal and resistive processes are taken into account. For the resistive processes, contributions from Umklapp phonon-phonon, phonon-isotope, phonon-impurity, phonon-dislocation, phonon-boundary, and phonon-free-electron scattering processes are included. For the case of the Fe doped semi-insulating samples compared to the Si-doped samples, everything in the model is similar other than the difference in mass and ionic radius of Fe and Si in the phonon-impurity contribution, the isotopes in the phonon-isotope contribution, and the lack of a phonon-free-electron contribution due to the samples semi-insulating nature. The absence of any phonon-free-electron scattering will provide a significant difference at elevated temperatures, as we found that free electrons in the Si doped samples caused significant scattering and therefore reduction in thermal conductivity. The difference between the two dopants can be illustrated by the value of α at a common doping concentration of $\sim 1\times10^{18}$ cm^{-3}. The value of α for the Si doped sample was 0.78 compared to 0.55 for the Fe doped sample. At the highest Si doping concentration ($7\text{x}10^{18}$ cm^{-3}) a value for α of 0.55 was found, which is shows that increasing the Si concentration leads to α values approaching those for similar Fe doped samples. It is expected that the quality (in terms of dislocation density) of the Si doped samples is slightly higher than that of the Fe doped samples measured in this work given the larger room temperature thermal conductivity at all dopant concentrations. Due to the higher room temperature thermal conductivity of the Si samples, the reduction with increasing temperature is larger with increased Si impurities because of increased impurity and free electron scattering. For the Fe

doped samples, the possibly lower crystalline quality and lack of phonon-free electron scattering led to a smaller reduction of thermal conductivity with temperature.

4.4. Conclusions

Semi-insulating material was created by growing GaN by HVPE and introducing Fe at various flow rates to modulate the resistivity. The effect of the Fe impurities on the thermal conductivity of the material was analyzed using the 3ω slope method. At room temperature, the Fe doping was found to reduce the thermal conductivity from 240 W/mK for the undoped sample to 194 W/mK for the sample with the highest doping. The reduction of thermal conductivity with increasing Fe concentration was attributed to increased phonon-impurity scattering. The reduction of thermal conductivity with Fe impurity concentration was compared to that of Si *n*-type impurities and was found to have less of an effect on the reduction of thermal conductivity due to no phonon-free electron contribution. The reduction in thermal conductivity at elevated temperatures was also examined and fit by a simple power law equation, where the power was found to range from 0.94 for the unintentionally doped sample to 0.55 for the samples with Fe impurity concentration greater than 8.0×10^{17} cm^{-3}. The further increase of Fe impurities at concentrations greater than 8.0×10^{17} cm^{-3} was shown to not significantly change the temperature dependence of thermal conductivity.

References

1 S. M. Hubbard, G. Zhao, D. Pavlidis, W. Sutton, and E. Cho, High-resistivity GaN buffer templates and their optimization for GaN-based HFETs, Journal of Crystal Growth 284, 297 (2005).

2 Hongbo Yu, M. Kemal Ozturk, S. Ozcelik, and E. Ozbay, A study of semi-insulating GaN grown on AlN buffer/sapphire substrate by metalorganic chemical vapor deposition, Journal of Crystal Growth 293, 273 (2006).

3 I. Shin, D. Kim, D. Lee, Y. Koh, M. K. Song, S. C. Shin, Y. Park, and E. Yoon, A new growth method of semi-insulating GaN layer for HEMT structure by eliminating degenerate layer at GaN/sapphire interface, 15, 11 (2015).

4 I. Ben-Yaacov, Y. Seck, U. K. Mishra, and S. P. DenBaars, AlGaN/GaN current aperture vertical electron transistors with regrown channels, Journal of Applied Physics 95, 2073 (2004).

5 R. P. Vaudo, X. Xu, A. Salant, J. Malcarne, and G. R. Brandes, Characteristics of semi-insulating, Fe-doped GaN substrates, Physica Status Solidi (a) 200, 18 (2003).

6 F. Lipski, Semi-Insulating GaN by Fe-Doping in Hydride Vapor Phase Epitaxy using a Solid Iron Source, Institute of Optoelectronics, Ulm University 63 (2010).

7 M. Slomski, L. Liu, J. F. Muth, and T. Paskova, Growth Technology for GaN, AlN Bulk Substrates and Templates, in Handbook of GaN Semiconductor Materials and Devices, (in press 2017).

8 J. A. Freitas, J. G. Tischler, J. -. Kim, Y. Kumagai, and A. Koukitu, Properties of Fe-doped semi-insulating GaN substrates for high-frequency device fabrication, Journal of Crystal Growth 305, 403 (2007).

9 S. Heikman, S. Keller, S. P. DenBaars, and U. K. Mishra, Growth of Fe doped semi-insulating GaN by metalorganic chemical vapor deposition, Applied Physics Letters 81, 439 (2002).

10 T. K. Uždavinys, S. Marcinkevičius, J. H. Leach, K. R. Evans, and D. C. Look, Photoexcited carrier trapping and recombination at Fe centers in GaN, Journal of Applied Physics 119, 215706 (2016).

11 R. Heitz, P. Maxim, L. Eckey, P. Thurian, A. Hoffmann, I. Broser Institut fu¨r Festko¨rperphysik, Technische Universita¨t Berlin, 10623 Berlin, and Germany, Excited States of Fe in GaN, 55, (1997).

12 E. Malguth, A. Hoffmann, and M. R. Phillips, Fe in III–V and II–VI semiconductors, Phys. Stat. Solidi B 245, (2008).

13 A. Witek, Some aspects of thermal conductivity of isotopically pure diamond a comparison with nitrides, Diamond and Related Materials 7, 962 (1997).

14 E. K. Sichel, J. I. Pankove, Thermal conductivity of GaN 25-360K, Journal of Physics and Chemistry of Solids 38, 330 (1977).

15 C. Luo, H. Marchand, D. R. Clarke, and S. P. DenBaars, Thermal conductivity of lateral epitaxial overgrown GaN films, Applied Physics Letters 75, 4151 (1999).

16 C. Mion, J. F. Muth, E. A. Preble, and D. Hanser, Accurate dependence of gallium nitride thermal conductivity on dislocation density, Applied Physics Letters 89, 92123 (2006).

17 M. Slomski, P. P. Paskov, J. H. Leach, J. F. Muth, and T. Paskova, Thermal conductivity of bulk GaN grown by HVPE: Effect of Si doping, Physica Status Solidi (B)1600713 (2017).

18 R. B. Simon, J. Anaya, and M. Kuball, Thermal conductivity of bulk GaN—Effects of oxygen, magnesium doping, and strain field compensation, Applied Physics Letters 105, 202105 (2014).

19 D. G. Cahill, Thermal conductivity measurement from 30 to 750 K: the 3ω method, Rev. Sci. Inst. 61, 802 (1990).

20 T. Borca-Tasciuc, A. R. Kumar, and G. Chen, Data reduction in 3ω method for thin-film thermal conductivity determination, Review of Scientific Instruments 72, 2139 (2001).

21 P. Paskov, M. Slomski, J. H. Leach, J. F. Muth, and T. Paskova, Effect of Si doping on the thermal conductivity of bulk GaN at elevated temperatures, J. Appl. Phys. (submitted 2017).

5. Thermal conductivity of ternary III-nitride alloys

The thermal conductivity of HVPE AlGaN films grown on GaN substrates was measured using the differential 3ω technique. Effects of alloy composition at constant thickness, thickness at constant alloy composition, and the addition of buffer layers on the thermal conductivity was explored. Results on thermal conductivity vs. Al concentration at a film thickness of ~1μm showed a strong reduction in thermal conductivity with small additions of alloy elements, which was explained by increased phonon scattering for Ga and Al mass differences. It was found that increasing the film thickness from ~1 - 25μm for $Al_{.13}Ga_{.87}N$ and $Al_{.24}Ga_{.76}N$ films resulted in a logarithmic increase approaching the bulk limit predicted in the literature of ~42W/mK and ~30W/mK, respectively. In order to determine if the effect of increasing phonon-dislocation scattering could be diminished for low film thicknesses, the effect of gradient and low temperature buffer layers on thermal conductivity was explored. For ~10μm $Al_{.24}Ga_{.76}N$ films, both buffer layers gave a ~6% increase in thermal conductivity, with the benefit predicted to be greater for thinner films.

5.1. Introduction

Over the last decade, the nitrides have seen increasing use in applications that were once controlled by only Si and other classical semiconductors. Today, electronic devices including field effect transistors (FETs) and Shottky barrier diodes (SBDs) based on nitrides are currently commercially available, competing or overperforming in some instances devices based on Si, and SiC. High electron mobility transistor (HEMT) based on AlGaN/GaN heterostructures have shown room-temperature mobilities of 2250 cm^2/Vs[1], and

current densities exceeding 1 mA/mm.[2,3] The large amount of power controlled in HEMTs and other high power devices often leads to self-heating in the device. The self-heating decreases the efficiency by reducing the current and possibly even causing device failure by thermal runaway. While modifying the electrical properties are necessary for these applications, the effect on the thermal characteristics cannot be overlooked.

Few reports on the thermal conductivity of the nitrides exist in the literature, and fewer exist for nitride alloys. The first measurement of the thermal conductivity of AlGaN alloys was performed by Daly et. al. for AlGaN films grown on sapphire by organometallic vapor deposition.[4] Measurements on films with alloy concentrations of $Al_{.18}Ga_{.82}N$ and $Al_{.44}Ga_{.56}N$ showed reductions in the GaN/AlN mean thermal conductivity (K = 171 W/mK) by factors of ~12 and ~27, respectively.[4] The large reduction in the thermal conductivity was attributed to scattering of phonons by mass-disorder as well as to the high dislocation density of 10^9-10^{10} cm^{-3} in the films. Previous studies of thermal conductivity were performed by Liu and Balandin for AlGaN films grown by HVPE on sapphire substrates using the 3ω method, and a strong reduction in thermal conductivity was found in materials with small additions (x = 0.0 - 0.1 and x = 0.9 – 1.0 in $Al_xGa_{(1-x)}N$) of alloy elements.[5] Calculations by the virtual crystal model agreed with experimental data and showed minimum room temperature thermal conductivity of 22 W/mK at an alloy fraction of x = 0.6. Ma et. al. reported similar calculations of the effect of alloy concentration on thermal conductivity using a first-principles calculation combined with the virtual crystal method.[6] Notably, they found that the addition of 1% of alloying decreases the room temperature thermal conductivity of pure GaN by up to 60%. The effects of film thickness were also reported and it was shown that size

effects persisted to a few hundreds of nanometers, with the thermal conductivity reduced to half of the bulk value in 100nm thick films.

Of the few existing publications in the literature on the thermal conductivity of AlGaN alloys, all have focused on AlGaN thin films with thickness less than 1 micrometer grown heteroepitaxially on foreign substrates. While it is common for GaN and therefore also AlGaN to be grown on substrates such as sapphire, Si, or SiC, this heteroepitaxial growth produces thin films with less than ideal properties due to the structural defects caused by the large lattice and thermal expansion coefficient mismatch. Heteroepitaxial GaN films typically exhibit dislocations densities in the range of $10^9 – 10^{10}$ cm^{-3}, which tends to decrease with increasing film thickness.[7] Such high dislocation density has been shown to play a strong role in the materials thermal properties.[8] More specifically, GaN films grown heteroepitaxially typically exhibit dislocation density in the range of $10^8 – 10^{10}$ cm^{-3} and thermal conductivities ranging from 130 to 170W/mK,[9, 10] while bulk GaN with dislocation density in the range of $10^4 – 10^6$ cm^{-3} has been shown to have thermal conductivities in the range of 240 - 270 W/mK.[11,12] Given the significant improvement in the thermal conductivity for bulk GaN and its potential application as substrate for AlGaN/GaN power devices, it is therefore valuable to know the thermal properties of AlGaN alloys grown on native high quality GaN substrates.

In this work we perform a systematic study of AlGaN films on GaN substrate with variable composition. Furthermore, aiming to explore the effect of materials quality and more specifically the effect of dislocation density on thermal conductivity, we study the thermal

conductivity of AlGaN layers with different thickness and different buffers, which are known to influence noticeably the defects.

5.2. Experimental methods

5.2.1. Sample characteristics

All of the AlGaN films studied were grown on bulk c-plane GaN by hydride vapor phase epitaxy (HVPE) at Kyma Technologies, Inc. The bulk GaN substrates used for growth had a thickness of about 400 μm and dislocation density ~5 x 10^6 cm^{-2}. The Al and Ga were introduced as a metal source in the HVPE reactor and the flow rate was adjusted to achieve the desired alloy composition and film thickness was varied by adjusting growth time.

Table 5.1 *Sample properties for the 4 sets of samples measured in this work.*

Set	Sample	Buffer	Al %	Thickness (mm)	N_{screw} (cm^{-2})	N_{edge} (cm^{-2})
1	A1	No	13	0.7	3.0x10^8	4.0x10^7
	A1	No	24	0.74	2.8x10^8	1.5x10^8
	A3	No	72	2.3	1.55x10^9	1.1x10^{10}
	A4	No	96	1.3	2.0x10^9	2.1x10^{10}
2	B1	No	13	0.7	3.0x10^8	4.0x10^7
	B2	No	15	12.3	2.8x10^8	2.7x10^7
	B3	No	15	22	1.1x10^8	1.5x10^7
3	C1	No	24	0.74	2.8x10^8	1.5x10^8
	C2	No	23	5.30	-	-
	C3	No	25	12.5	2.8x10^8	2.7x10^7
	C3	No	25	24.5	9.5x10^7	2.2x10^7
4	D1	No	25	12.5	2.8x10^8	2.7x10^7
	D2	LT – buffer	23	10	1.6x10^8	1.3x10^7
	D3	Gradient buffer	23	10	7.7x10^7	1.9x10^7

The samples studied are broken into four groups: 1) AlGaN layers with varying alloy concentration at a constant thickness ~1-2 μm aiming to examine the effect of alloy concentration and to compare to similar results in the literature of AlGaN grown on sapphire (Set 1 in *Table 5.1*), 2) AlGaN layers with varying film thickness at a constant alloy concentration of x = ~15% (Set 2 in *Table 5.1*)**,** 3) AlGaN layers with varying film thickness at a constant alloy concentration of x = ~25% (Set 3 in *Table 5.1*)**,** and 4) AlGaN layers grown on GaN by using AlN buffer and AlGaN buffer with composition gradients between the GaN substrate and the AlGaN layer with a constant alloy concentration of x = ~25% (Set 4 in *Table 5.1*), aiming to reveal the effect of layer quality on thermal conductivity.

5.2.2. Crystalline quality

Structural characterization was carried out with a Philips X'Pert Materials Research Diffractometer with $K_{\alpha 1}$ (λ=1.54Å) radiation source operating at 40 kV and 45 mA. High resolution X-ray diffraction (HRXRD) rocking curves of the symmetric 002 and skew-symmetric 101, 102, 103, 302 reflections were recorded in double axis geometry, with a four-bounce Ge [220] monochromator on the incident beam side and an open detector.

The HRXRD was used to evaluate the defect density in the AlGaN layers, aiming to distinguish the different types of dislocation and their variation with changing the composition, the thickness or the buffer type. A precise approach to estimate dislocation density was proposed by Srikant.[13] The density of dislocations was estimated from X-ray diffraction rocking curves measured at different inclination angles and the extrapolated curve allowed an estimation of the tilt at no inclination and at 90 degrees. The full width at half maximum (FWHM) of X-ray rocking curves are related to dislocation density via the well

known formulas, $N_{screw} = \beta^2_{tilt}/4.35b_c^2$ and $N_{edge} = b^2_{twist}/4.35b_a^2$, where $N_{screw/edge}$ refers to the density of screw dislocations when using β_{tilt} and b_c in the equation and refers to the edge dislocation density when using β_{twist} and b_a in the equation; β_{tilt}, β_{twist} are the tilt and twist spreads; b_c, b_a are the Burgers vectors of c- and a-type threading dislocations, respectively, for any given composition. The FWHMs of the rocking curves of 002, 103, 102 and 302 reflections were determined after peak deconvolution of all the spectra.

5.2.3. 3ω measurement details

The thermal conductivity of AlGaN alloys grown on GaN was measured using the differential 3omega technique outlined by Cahill.[14] The slope method of the 3ω was applied to measure the thermal conductivity of the bulk GaN substrate. To measure the AlGaN films, an extension of the 3ω method known as the differential technique was employed. The differential technique relies on the concept that a thin film on the surface of a substrates acts as a layer with a finite thermal boundary resistance. Similar to the slope method, a line heater/thermometer is deposited onto the surface of the thin film on substrate and the same technique described is carried out to find the thermal fluctuations in the thin film on substrate, ΔT_{F+S}. Next, another heater/thermometer line with identical dimensions as the first is deposited on to a bare substrate with identical properties to the one in which the thin film was grown on. The same measurement technique is carried out on the bare substrate to get the thermal fluctuations in the substrate, ΔT_S. The nomenclature of the differential method stems from the fact that the temperature fluctuations in the bare substrate are subtracted from those of the film on substrate to obtain the thermal fluctuations in the film by

$$\Delta T_{F+S} - \Delta T_S = \Delta T_{F,1D} \tag{5.34}$$

The thermal conductivity of the thin film KF,1D can then be calculated by

$$K_{F,1D} = \left(\frac{\Delta T_F}{P}\right)^{-1} \frac{d_F}{lw} \tag{5.35}$$

where dF is the film thickness, and l and w are the length and width of the metal heater/thermometer line, respectively. The subscript of 1D denotes that this equation is derived based on boundary conditions that assume one-dimensional heat flow in the film, which is discussed in the next paragraph. Equation (5.35) shows that the precise dimensions of both the film and the heater/thermometer line are necessary and any small errors in the measurements can lead to large errors in the determination of $K_{F,1D}$. The dimensions of the heater line were measured post deposition using optical microscopy and profilometery. For the differential measurement, it is critical that the dimensions of the heater/thermometer line on the bare substrate and the thin film on substrate are identical. It is also important that the power across the lines be identical, which is the case if the line dimensions are the same. Film thickness was determined via ellipsometery with high precision.

The extraction of the thermal conductivity of the film in Equation (5.35) requires that boundary conditions be met based on the film thickness d_F, line half-width b, film thermal conductivity anisotropy, and the ratio of film to substrate thermal conductivity K_F/K_S. Given that Equation (5.34) assumes 1D heat flow through the film, it is necessary that $K_F << K_S$ and that $b >> d_F$. Films with large thicknesses and/or films with small contrast in thermal conductivity with the substrate violate the 1D heat flow assumption due to non-negligible heat spreading effects in the film. Borca-Tasciuc et. al. have formulated an equation that

allows for the compensation of such heat spreading effect and allows for the measurement of samples that would normally not meet boundary conditions.[15] In their work, a parameter C relating the film to substrate thermal conductivity contrast and a parameter S describing the heat spreading in the film are used to compensate the calculated thermal conductivity in the 1D assumption in order to find the true film thermal conductivity K_F by

$$K_F = K_{F,1D}CS \tag{5.36}$$

The equations for C and S in Equations (2.22) and (2.23) include effects from film anisotropy, however due to the relatively small difference between the c-plane and a-plane thermal conductivity in GaN, the equations have been simplified to the isotropic case such that

$$C = 1 - \frac{K_F}{K_S} \tag{5.37}$$

$$S = \frac{2}{\pi}\int_0^\infty \frac{\sin\lambda}{\lambda^3}\frac{\tanh(\lambda\beta_F)}{\beta_F\left[1 + (\frac{K_F}{K_S})\tanh(\lambda\beta_F)\right]}d\lambda \tag{5.38}$$

where

$$\beta_F = \frac{d_F}{b} \tag{5.39}$$

In this work, the AlGaN on GaN layers with varying alloy concentrations and film thicknesses create situations where the boundary conditions are not met and the calculated differential thermal conductivity needs to be compensated for heat spreading in the film. The boundary condition that $K_F << K_S$ is violated in situations where the AlGaN film has thermal conductivity approaching the values for the pure material; specifically at $Al_xGa_{(1-x)}N$ ratios of x = 0 – 0.1 and x = 0.9 – 1.0. As K_F approaches K_S, the calculated thermal conductivity in the

1D case overestimates the true film thermal conductivity and C decreases to adjust for the overestimation. The other boundary condition, $d_F << b$, is violated for very thick AlGaN layers unless very wide metal lines are patterned and deposited onto the surface. While it is possible to deposit such lines, it is not experimentally feasible as wide lines tend to decrease the current density and therefore the thermal fluctuation magnitude; and thus can decrease the signal to noise ratio to unacceptable levels when measuring relatively high thermal conductivity samples with the 3omega method.

5.3. Results and discussion

The thermal conductivity of $Al_xGa_{(1-x)}N$ films with x fractions of 0.13, 0.24, 0.72, 0.96 can be seen in *Figure 5.1*. The endpoints of the alloy range included a bulk GaN sample grown by HVPE with thermal conductivity of 240W/mK and a bulk AlN sample grown by modified HVPE growth with thermal conductivity of 295 W/mK. It is noted that the use of bulk samples for the pure compounds shifts the endpoints of the figure higher than if heteroepitaxial thin films of pure material were measured. One can see that the addition of small amounts of alloying elements quickly reduces the high values of thermal conductivity seen in the pure compounds. For the two samples with the lowest alloy concentration, $Al_{.13}Ga_{.87}N$ and $Al_{.24}Ga_{.76}N$, the data is very close to thermal conductivity of AlGaN layers on saphhire reported by Daly.[4] Samples were chosen with similar thicknesses as close to 1µm as possible for means of comparison, however the actual thickness is listed above the data points. Prior to adjustment of the thermal conductivity data calculated by the 1D approximation with Equation (5.3), values were in good agreement by the results found by Liu.[5] A 10µm line width (b = 5µm) was used to measure the thermal conductivity of the

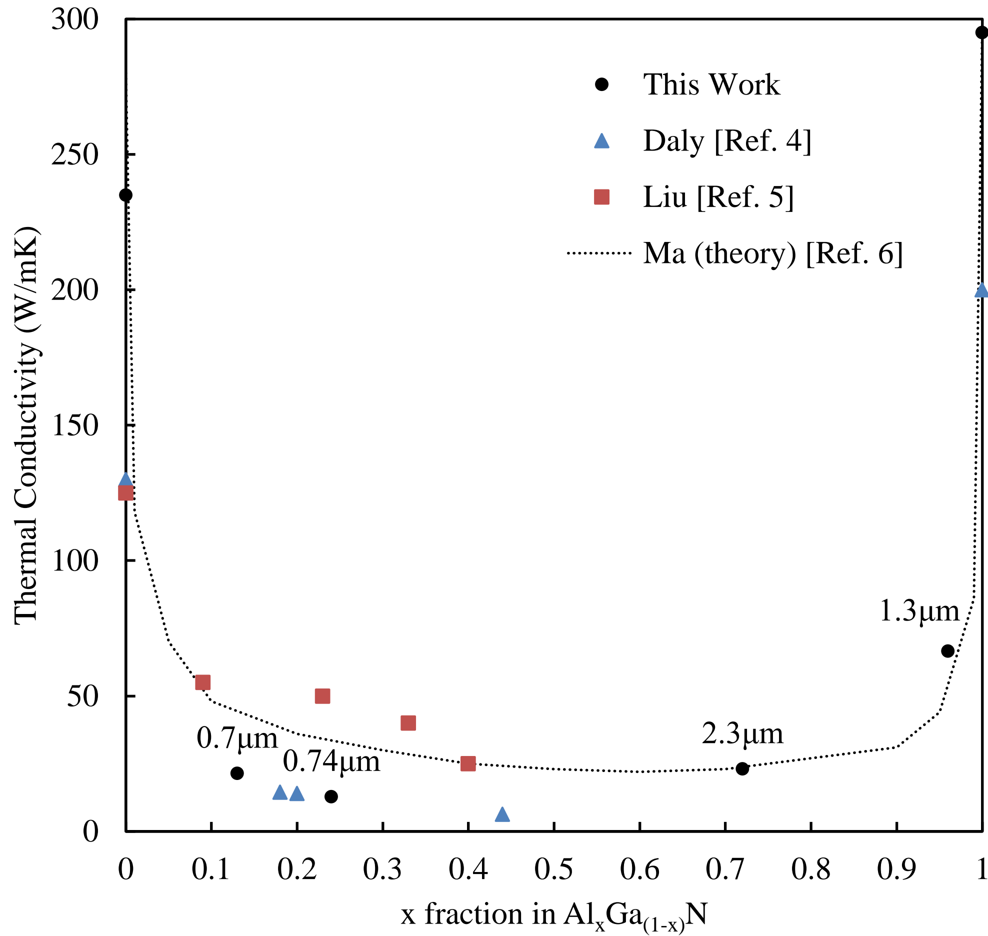

Figure 5.1 *Thermal conductivity vs. Al fraction of ~1µm $Al_xGa_{(1-x)}N$ measured in this work (black circles) with exact film thicknesses listed. Values are compared to those obtained by experimental results of Daly[4] (blue triangles) and Liu[6] (red squares) as well as to a calculated bulk limit from Ma[6] (dashed line).*

$Al_{.13}Ga_{.87}N$ and $Al_{.24}Ga_{.76}N$ samples, which does not fully satisfy the boundary condition that $\beta_F \rightarrow 0$ since $\beta_F = 0.14$. At this value of β_F, the true film thermal conductivity K_F can only be $0.95K_{F,1D}$ at best, however the reduction from the 1D case is actually higher due to the other boundary condition that $K_F << K_S$. Since the $Al_{.13}Ga_{.87}N$ film is close to pure GaN, its thermal conductivity is higher than that of the alloys near the middle of the alloy range. As

the film alloy concentration $x \rightarrow 0$, $K_F \rightarrow K_{GaN}$ and C in Equation (5.37) reduces $K_{F,1D}$ more significantly. The consequence of this data adjustment is that the reduction in the thermal conductivity with the addition of alloying elements is even stronger than previously reported estimations using the 3ω method. Theoretically calculated AlGaN thermal conductivity dependence of composition by Ma et. al. showed that the addition of 1% Al to GaN causes a 58% decrease in thermal conductivity from that of the pure material.[6] The strong reduction has been explained as a large increase in phonon scattering due to the mass difference of the Al and Ga atoms. Additions of 1% Al atoms introduces a significant number of irregularity to the lattice which decreases the mean free path of phonons. The dashed line in *Figure 5.1* are the calculated thermal conductivities of bulk c-plane AlGaN from the work of Ma et. al. Our experimental data is in good agreement with the theoretical curve, especially at concentrations of $Al_{.72}Ga_{.28}N$ and $Al_{.96}Ga_{.04}N$. For the $Al_{.13}Ga_{.87}N$ and $Al_{.24}Ga_{.76}N$ samples, the theoretical curve gives values higher than the experimental results in this work. One possible explanation for this is that the pure GaN material used in this work had a thermal conductivity of 240 W/mK, as measured for our bulk substrates, while Ma used a value of 279 W/mK in the calculation. The use of a higher thermal conductivity of pure GaN, while having equivalent values for pure AlN, has the effect of skewing theoretical curve upwards at $x < 0.5$. It must also be noted that the theoretical curve was calculated for bulk AlGaN material while the samples measured in this work range from 0.7 – 2.3μm. A theoretical curve for 200nm thick AlGaN films was calculated by Ma for the a-plane, however no c-plane results were included. The results for the 200nm a-plane films showed a reduction in thermal conductivity from the bulk values for all alloy concentrations. In their work, they

found the thermal conductivity of 100nm thick films to be half of the bulk value, so it is likely that our results would fall in line with a theoretical curve calculated with a 1μm film thickness.

It must be noted that both the differential 3ω calculation and the data correction used in this work have been simplified to assume that the film has isotropic thermal conductivity. Results from theoretical calculation of Ma et. al. show that the anisotropy ratio can be at maximum 20% between a-plane and c-plane thermal conductivity for the alloy compounds. For pure compounds, anisotropy was found to have much less of an effect, with the largest anisotropy being in the range of $x = 0.1 – 0.9$. Given that the anisotropy is only fairly large in this intermediate alloy range where the magnitudes of thermal conductivity are low, we neglected anisotropy effects in the measurement and calculation of thermal conductivity.

Furthermore, in order to explore the effect of layer quality and defect density on the thermal conductivity of AlGaN films on GaN we studied samples with different thickness and employing two types of buffers. Measurements were performed on samples with thickness 0.7μm, 12.3μm, and 22μm at $x = 0.15$ Al fraction and thickness 0.74μm, 5.30μm, 12.5μm, and 24.5μm at $x = 0.25$ Al fraction. All literature reports thus far have focused on thin (<1μm) films and no systematic study on the effect of thickness and crystal quality has been performed. The calculated dislocation density values for both edge and screw type of dislocations are shown in *Table 5.1* for all sets of samples. Analyzing the data in *Table 5.1,* for sets 2 and 3 one can see that the that the dislocation density decreases for composition 15% (set 2) and 25% (set 3), though the decrease is relatively moderate for the thickness used but is in agreement with all the reports on thickness dependencies of dislocation density in

nitride layers. One can also see that dislocation density of the edge dislocation is more affected by increasing the thickness than the screw dislocation, which remain higher than the edge dislocation density practically in all the samples studied. Nevertheless, it is clear that there is an improvement of the defect density with increasing thickness in both sets.

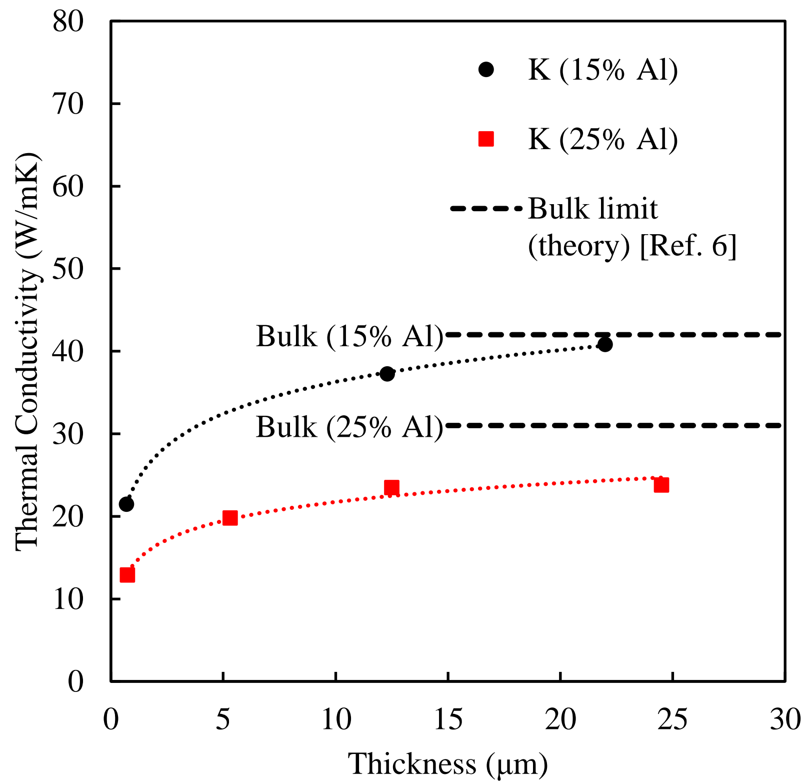

Figure 5.2 *Measured Thermal conductivity vs. AlGaN film thickness for Al concentrations of 15% (black circles) and 25% (red squares) with logarithmic fit (dashed lines). Horizontal lines represent the bulk limit for each Al% as calculated by Ma in Ref. 6.*

Figure 5.2 displays thickness dependences of the thermal conductivity of AlGaN layers with composition of $x = 0.15$ and $x = 0.25$ Al fraction. For both Al compositions, one can see a logarithmic trend of the thermal conductivity versus the layer thickness. From a

physical point of view, this trend makes sense, as decreasing the thickness so that $d_F \rightarrow 0$ results in $K_F \rightarrow 0$. The reduction in thermal conductivity with decreasing film thickness is explained by both an increase in phonon-boundary scattering and the higher dislocation density of the films. It has been calculated that the mean free path of phonons in GaN ranges from 10nm to 10μm,[6] therefore decreasing the films thickness past the 10μm starts to suppress the contribution of some of the phonons in heat conduction. While our experimental data is fit well by a logarithmic trend line, it is expected that the thermal conductivity will not continue to increase as d_F increases, but rather it approaches the limit of the bulk material. *Figure 5.2* includes the limit of the bulk materials thermal conductivity as calculated by Ma et. al. for x = 0.15 and x = 0.25.[6] It is clear from *Figure 5.2* that as the thickness of the films increase, the thermal conductivity approaches the calculated value for the bulk material of ~30 W/mK for x = 0.15 and ~42 W/mK for x = 0.25.

The reduction of thermal conductivity with thickness of AlGaN films compared to its pure compounds is an obvious downfall when designing devices that require large current densities such as HEMTs. As discussed in the last paragraph, the reduction was explained by an increase in phonon boundary and phonon-dislocation scattering. While phonon-boundary scattering is an intrinsic phenomenon that cannot be mitigated, the phonon-dislocation scattering can be reduced through the growth optimization of higher quality films. One obvious solution as seen in *Figure 5.2* is to grow thicker films, however some applications require thinner films and therefore a different approach must be used to lessen the dislocation density. One option is the use of low-temperature buffer layers or composition gradient buffers in between the GaN substrate and AlGaN film. Two AlGaN films with thicknesses of

~10μm and Al compositions of x ~ 0.25 grown with different buffer layer techniques were measured and compared to an AlGaN film with the same thickness and composition without a buffer (*Table 5.1*). From a structural quality and defect density point of view, one can see that inserting the buffers led to some defect density reduction, though it was not substantial. The thermal conductivity of the layer without buffer was determined to be 23.5 W/mK. The addition of a low-temperature buffer layer increased the thermal conductivity to 24.7 W/mK while the sample with the addition of a gradient buffer yielded 25.1 W/mK. For these 10μm thick films, the buffers give a modest ~6% increase in the thermal conductivity, however in thinner films it may be possible to see up to an ~11% increase. Given that AlGaN films are typically used in applications where self-heating is an issue, the increase in thermal conductivity given by the inclusion of a buffer layer seems to be a valuable alternative.

5.4. Conclusions

The differential 3ω technique was employed to measure the thermal conductivity of AlGaN thin films grown by HVPE on GaN substrates and the effects of alloy composition, material quality were explored. Adjustments to the differential data calculated by the 1D model were made to account for unsatisfied boundary conditions by using an equation by Borca-Tasciuc. The effect of alloy composition was studied by measuring the thermal conductivity of a set of AlGaN thin films with a thickness of ~1-2 μm. It was found that the addition of alloying elements quickly decreased the thermal conductivity of the pure constituent GaN and AlN compounds due to mass difference scattering of phonons. Experimental data at low Al compositions agreed well with results from Daly et. al, however results were lower than predicted by virtual crystal calculations by Ma et. al. It is

hypothesized that this occurred due to calculations by Ma being performed for bulk material while measurements were on samples of thickness 0.7-2.3μm. This hypothesis was strengthened by examining the effect of increasing film thickness on the thermal conductivity of samples with x = 0.15 and x = 0.25 alloy concentration. Results on both alloy concentrations showed that increasing the film thickness and decreasing the dislocation density yielded a logarithmic increase in thermal conductivity approaching the bulk limit calculated by Ma of ~42W/mK for x = 0.15 and ~30W/mK for x = 0.25. The reduction in thermal conductivity with decreasing film thickness was explained by an increase in phonon-boundary and phonon-dislocation scattering. Attempts at decreasing the phonon-dislocation scattering were examined by measuring the thermal conductivity of samples with a gradient buffer layer and a low-temperature buffer layers. The addition of the low-temperature buffer layer and gradient buffer layer yielded improved thermal conductivities of 24.6 and 25.1 W/mK, respectively, when compared to a similar sample without a buffer layer.

References

1 J. Chen, I. Persson, D. Nilsson, C. Hsu, J. Palisaitis, U. Forsberg, P. O. Å Persson, and E. Janzén, Room-temperature mobility above 2200 cm2/V·s of two-dimensional electron gas in a sharp-interface AlGaN/GaN heterostructure, Appl. Phys. Lett. 106, 251601 (2015).

2 A. Chini, R. Coffie, G. Meneghesso, E. Zanoni, D. Buttari, S. Heikman, S. Keller, and U. K. Mishra, 2.1 A⁄mm current density AlGaN⁄GaN HEMT, Electronics Letters 39, 625 (2003).

3 N. G. Weimann, M. J. Manfra, S. Chakraborty, and D. M. Tennant, Submicron AlGaN/GaN HEMTs with very high drain current density grown by plasma-assisted MBE on 6H-SiC, Led 23, 691 (2002).

4 B. C. Daly, H. J. Maris, A. V. Nurmikko, M. Kuball, and J. Han, Optical pump-and-probe measurement of the thermal conductivity of nitride thin films, Journal of Applied Physics 92, 3820 (2002).

5 W. Liu, and A. Balandin, Thermal conduction in Al x Ga 1 − x N alloys and thin films, Journal of Applied Physics 97, (2005).

6 J. Ma, W. Li, and X. Luo, Intrinsic thermal conductivities and size effect of alloys of wurtzite AlN, GaN, and InN from first-principles, Journal of Applied Physics 119, 125702 (2016).

7 T. Paskova, D. A. Hanser, and K. R. Evans, GaN Substrates for III-Nitride Devices, Jproc 98, 1324 (2010).

8 C. Mion, J. F. Muth, E. A. Preble, and D. Hanser, Accurate dependence of gallium nitride thermal conductivity on dislocation density, Applied Physics Letters 89, 92123 (2006).

9 E. K. Sichel, J. I. Pankove, Thermal conductivity of GaN 25-360K, Journal of Physics and Chemistry of Solids 38, 330 (1977).

10 G. A. Slack, L. J. Schowalter, D. Morelli, and J. A. Freitas, Some effects of oxygen impurities on AlN and GaN, Journal of Crystal Growth 246, 287 (2002).

11 E. Richter, M. Gründer, B. Schineller, F. Brunner, U. Zeimer, C. Netzel, M. Weyers, and G. Tränkle, GaN boules grown by high rate HVPE, Physica Status Solidi (C) 8, 1450 (2011).

12 M. Slomski, L. Liu, J. F. Muth, and T. Paskova, Growth Technology for GaN, AlN Bulk Substrates and Templates, in Handbook of GaN Semiconductor Materials and Devices, (in press 2017).

13 V. Srikant, J. S. Speck, and D. R. Clarke, Mosaic structure in epitaxial thin films having large lattice mismatch, Journal of Applied Physics 82, 4286 (1997).

14 D. G. Cahill, M. Katiyar, and J. R. Abelson, Thermal conductivity of a-Si:H thin films, Physical Review B 50, 6077 (1994).

15 T. Borca-Tasciuc, A. R. Kumar, and G. Chen, Data reduction in 3ω method for thin-film thermal conductivity determination, Review of Scientific Instruments 72, 2139 (2001).

6. Thermal conductivity of other wide bandgap semiconductors: β-Ga_2O_3

The thermal conductivity of undoped, Sn-doped and Fe-doped β-Ga_2O_3 bulk crystals was measured by the 3ω technique in the temperature range of 295-405 K. A unique approach for extracting the thermal conductivity along the lateral and transverse heat flow directions was used in order to determine the thermal conductivity along different crystallographic directions. The data analysis at room temperature confirmed the expected anisotropy of the thermal conductivity of β-Ga_2O_3, revealing the highest value of ~ 29 W/mK in the [010] direction. The thermal conductivity of the Sn-doped and Fe-doped β-Ga_2O_3 samples was found to be lower than that of the undoped samples due to the enhanced phonon-impurity scattering contribution, which reduces the thermal conductivity. This tendency was maintained for the thermal conductivity at elevated temperatures. The thermal conductivity in all sample decreased with increasing temperature but the slope of the temperature dependence was found to depend on both the doping and the crystallographic orientation.

6.1. Introduction

In the last years, β-Ga_2O_3 has emerged as a promising new wide bandgap semiconductor for power device applications.[1] Due to its superior material properties – large bandgap (4.9 eV), high breakdown field (8 MV/cm^{-1}) and low on-state resistance, β-Ga_2O_3 is now regarded as an potential alternative to SiC and GaN.[2] For β-Ga_2O_3-based devices used in high-voltage switching applications, e. g. metal-oxide-semiconductor field-effect transistors (MOSFET) and Schottky barrier diodes (SBDs) the high breakdown field may reduce the complexity of field plate design and reduce field related reliability issues observed in other

materials. Another important advantage of β-Ga_2O_3 is that native substrates of a relatively low cost can be fabricated in large volumes from bulk single crystals synthesized by melt-growth techniques such as Czochralski,[3] Bridgman,[4] floating-zone (FZ),[5] and edge-defined film-fed growth (EFG).[6] β-Ga_2O_3 based SBDs[7-9] and MOSFET[2, 10-13] with exciting performance characteristics on native substrates have been demonstrated by several groups. A SBD with Si doped β-Ga_2O_3 drift layer grown by halide vapor phase epitaxy (HVPE) on Sn doped bulk substrate has showed a near-unity ideal factor and a reverse breakdown voltage of 500 V.[9] For a two-finger MOSFET grown by metal-organic vapor phase epitaxy (MOVPE) on a semi-insulating Mg doped substrate a gate-to-drain electric field of 3.8 MV/cm was achieved, which is higher than bulk SiC and GaN theoretical limits.[11] Fin-channel field-effect transistor (FinFET) and depletion mode MOSFET with a breakdown voltage over 600 V and 750 V, respectively, were also demonstrated.[12,13]

Ultimately the performance of power electronic devices is limited by thermal considerations and understanding the thermal properties above room temperature is important. The junction temperatures for silicon based power electronics are typically designed for 150 ^{o}C. Commercial silicon carbide devices are being sold with a maximum junction temperature of 200 ^{o}C with the limitation being the choice of contacts and surrounding packaging although the theoretical junction temperatures could be much higher. The thermal conductivity GaN bulk crystals had been underestimated in the literature until experimental measurements were made which revealed a very strong dependence on the defect concentration.[14]

With β-Ga_2O_3, we are fortunate to have bulk crystals to study, but the thermal properties of β-Ga_2O_3 are still not well understood. Due to the low symmetry of the monoclinic crystal structure of β-Ga_2O_3 a high anisotropy of all material parameters is expected. As for the thermal conductivity, the anisotropy is a result of the difference in the sound velocities, the Grüneisen parameters (i. e. phonon anharmonicity), and the Debye temperature in different crystallographic directions. There are few reports on experimentally measured thermal conductivity in bulk of β-Ga_2O_3 crystals.[3,15-18] A thermal conductivity of 21 W/mK along [010] direction in Czochralski grown β-Ga_2O_3 and of 13 W/mK along [100] direction in FZ grown β-Ga_2O_3 was measured by laser flash method.[3,18] A detail study of the anisotropy of the thermal conductivity in Sn doped β-Ga_2O_3 was performed on EFG grown crystals by time domain thermoleflectance (TDTR).[16] The thermal conductivity in four crystal orientation [001], [100], [010], and [-201] was measured in the temperature range of 80-495 K. The lowest thermal conductivity value at room temperature was found along for [100] direction (10.9 W/mK) while the highest value was measured along [010] direction (27 W/mK). The thermal conductivity along [100] direction in undoped and Mg doped Czochralski grown β-Ga_2O_3 crystals was studied by 3ω method grown by Czochralski grown method.[17] In both samples the room temperature value of 13 W/mK was obtained. A maximum thermal conductivity of 530 W/mK was measured at 25 K. Recently, 2ω method was applied to measure the thermal conductivity along [100], [010], and [001] of the same type Mg doped samples and room temperature values of 11 W/mK, 29 W/mK and 21 W/mK, respectively, were obtained.[18] The first principles calculations of the thermal conductivity of

β-Ga_2O_3 have predicted room temperature values very close to the experimental ones, namely 16 W/mK, 21.5 W/mK and 21 W/mK, along [100], [010], and [001], respectively.[19]

In this work, we use 3ω method to study the thermal conductivity anisotropy in undoped, *n*-type Sn doped and semi-insulating Fe doped bulk β-Ga_2O_3 grown by EFG. For the semi-insulating β-Ga_2O_3, Fe-doped material was used due to access to samples, however, we are interested in measuring and comparing Fe dopants to Mg dopants at a later date. Samples with different surface orientations are used and a specific direction-oriented pattern of 3ω devices are applied in order to extract the thermal conductivity in multiple crystallographic directions of an anisotropic β-Ga_2O_3 crystal. To the best of our knowledge, this is the first study of the effect of different dopants and the heat flow directions on the thermal conductivity of β-Ga_2O_3.

6.2. Experimental details

6.2.1. Sample growth and characterization

The samples used in this work were grown by EFG by Tamura Corp.[6] Undoped, Sn doped and Fe doped samples with (010) and (-201) surfaces were examined. The electron concentration was ~ 3×10^{17} cm^{-3} in the undoped (due to residual impurities) samples and ~ 3.5×10^{18} cm^{-3} in Sn doped samples. The Fe doped samples were semi-insulating with a resistivity > 10^{10} Ω.cm. The in-plane crystallographic orientation needed for the alignment of the heater/sensor devices for thermal conductivity measurements is defined by the supplier and confirmed by X-ray diffraction (XRD) measurements. Samples orientations used in this study are summarized in *Table 6.1*.

Table 6.1 *Growth face, orientation of heater/thermometer device, and respective heat flow directions for the samples measured in this work.*

Dopant type	Growth face	Transverse heat flow	Device orientation	Lateral heat flow
undoped	(-201)	⊥(-201)	[010]	[102]
undoped	(-201)	⊥(-201)	[102]	[010]
undoped	(010)	[010]	⊥[102]	[102]
undoped	(010)	[010]	[102]	⊥[102]
Sn	(-201)	⊥(-201)	[102]	[010]
Sn	(-201)	⊥(-201)	[010]	[102]
Sn	(010)	[010]	[102]	⊥[102]
Fe	(010)	[010]	⊥[102]	[102]
Fe	(010)	[010]	[102]	⊥[102]

6.2.2. 3ω measurement details

The method used for characterizing the thermal conductivity in this study is known as the slope method of the 3ω technique. In the 3ω method, a thin metal heater/sensor device is deposited onto the surface of the sample using photolithography and electron-beam deposition. An AC current with an input frequency ω is passed across the heater/sensor and a voltage at 3ω, $V_{3\omega}$, is measured across voltage taps at a specified distance along the line. Details of the measurement procedure and how the thermal conductivity is extracted from $V_{3\omega}$ has been discussed in detail elsewhere and is not included in this work.[20] In our previous work,[21] the specific details about the deposition of the metal heater/sensor 3ω devices and equipment used have been described. The measurements are done in the temperature interval 295-405 K. The use of the slope method of the 3ω technique over these temperatures is validated by observed linear dependence of $V_{3\omega}$ vs. ln(ω/2π) for the entire frequency range

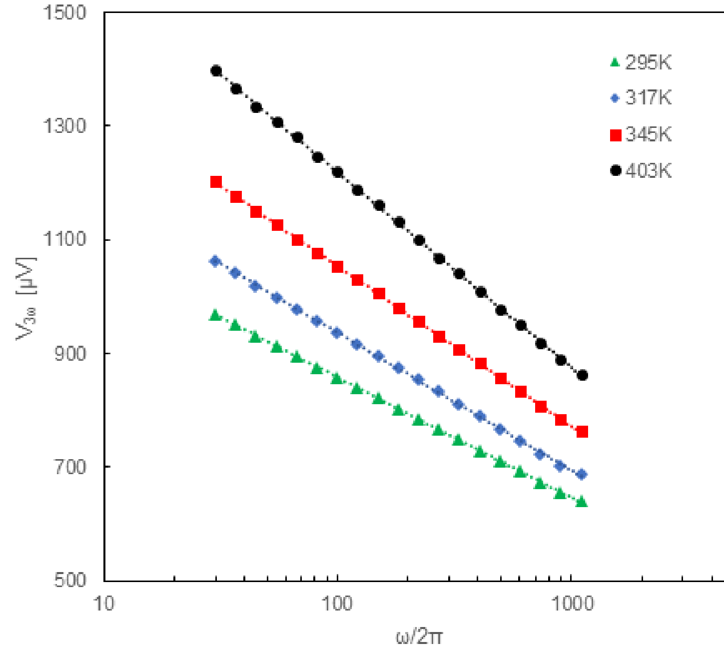

Figure 6.1 *Linear dependence of $V_{3\omega}$ vs. $\omega/2\pi$ (semi-log) for an undoped sample in the temperature range measured in this work.*

used (50-1000 Hz) (*Figure 6.1*). The existence of the linear dependence in *Figure 6.1* illustrates that the thermal waves are contained in a region within the sample that satisfies the boundary conditions of the slope method. The distance that the thermal waves penetrate into the sample is given by Equation (2.6). Given that k, ρ, and C_P are all material constants, the penetration depth of the thermal waves is solely determined by the angular frequency of the current across the line. The boundary conditions outlined by Borca-Tasciuc[22] for less than 1% error in the determination of thermal conductivity in the slope method state that $2.5w < \lambda < 5d$, where w is the width of the heater/thermometer line and d is the thickness of the sample. Given that the thermal conductivity and therefore the penetration depth in the sample

varies with temperature, *Figure 6.1* illustrates that the boundary conditions are met for all temperatures studied in this work.

The challenge of this experiment has to do with the fact that the sample is highly anisotropic and that the 3ω method relies on cylindrical heat flow rather than unidirectional heat flow. For any thermal conductivity characterization technique, it is necessary to have a heat source and a thermometer. Some techniques rely on generating heat at one side of a sample and then measuring the temperature change at a fixed point along the sample – these techniques would be considered unidirectional since heat flow occurs only along one crystalline axis. The slope method relies on heat flow radiating cylindrically from the heater/sensor line, making the 3ω technique a two-dimensional thermal characterization technique. For anisotropic samples this presents challenges. *Figure 6.2(a)* shows a cross-sectional view of a sample with the heater/sensor used for the 3ω measurement aligned along z direction perpendicular to the x-y cross sections of the sample. The cylinder in *Figure 6.2(a)* denotes the region that heat flows away from the heater source on the surface and where periodic temperature fluctuations can be measured. A material with a high thermal conductivity is able to disperse heat effectively from the source, leading to smaller temperature fluctuations ΔT recorded by the sensor. Since heat is dispersed in all directions cylindrically within the sample, the 3ω measurement is a function of heat flow of all directions within the cylinder. k_x and k_y denote the thermal conductivity in the lateral and transverse directions, respectively. *Figure 6.2(b)* provides an example of a heater/sensor aligned in the ⊥[102] direction of the (010) plane of β-Ga_2O_3. In this example, the direction perpendicular to the line on the surface is [102] and the direction perpendicular to the face of

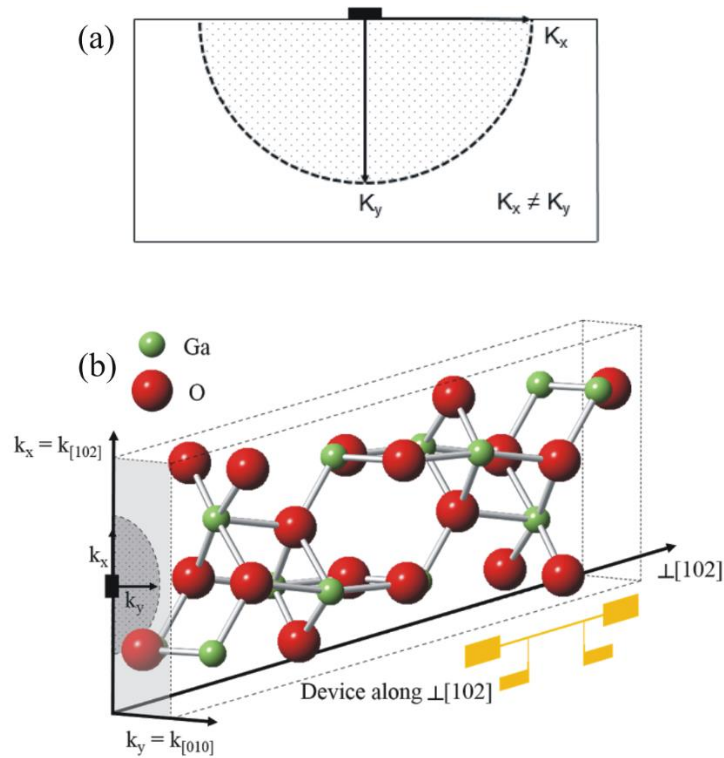

Figure 6.2 *(a) A cross-section view of sample with heater/sensor on the surface. The semi-circle represents the directions of heat flow radiating from heater line (black rectangle) and k_x and k_y denote the thermal conductivity in the lateral (x) and transverse (y) directions. (b) Monoclinic unit cell of β-Ga_2O_3 with an example of a heater/thermometer oriented in the ⊥[102] direction on the (010) face. In this example, the lateral thermal conductivity is measured in the $k_x = k_{[102]}$ direction and the transverse thermal conductivity is measured in the $k_y = k_{[010]}$ direction.*

the sample is [010]. For this representative example, the thermal flow is distributed along xy plane, and the extracted thermal conductivity components are $k_x = k_{[102]}$ and $k_y = k_{[010]}$. Due to the anisotropy β-Ga_2O_3 has different material properties in each crystallographic direction and k_x and k_y will not be equivalent. The monoclinic unit cell, seen in *Figure 6.2(b)*, clearly illustrates the low symmetry and high anisotropy involved with measurements on β-Ga_2O_3. Thus, the slope method measurements will yield a value that is some function of lateral and transverse thermal conductivity. As mentioned earlier, it is therefore important to denote

what the lateral and transverse directions of the samples are in order to know what directions are being measured in a slope method calculation. The transverse heat flow direction is known by finding the perpendicular to the face of the sample that is being measured. For the lateral direction, orientation is selected by depositing the heater device at some known angle with respect to the scribe mark which denotes a known crystallographic direction along the surface of the sample as determined by XRD.

For the purpose of this experiment, the lateral orientations are set by depositing the heater/sensor either parallel or perpendicular to the scribe mark in order to give the lateral and transverse heat flow directions. *Table 6.1* shows that for each dopant type, a specific lateral and transverse heat flow direction is defined by the device orientation and growth direction, respectively. For the undoped sample and the Sn doped sample, it can be seen that there are for unique heat flow directions between the lateral and transverse directions: [010], [102], ⊥[102], and ⊥(-201). The notations ⊥[102] and ⊥(-201) is used to denote directions perpendicular to the [102] crystallographic direction and to (-201) surface, respectively. For the Fe doped sample set only three unique orientations can be determined – [010], [102], and ⊥[102]. In this study the thermal conductivity in each of these directions is determined for all samples. However, first the thermal conductivity values in the lateral and transverse directions must be extracted from the measured thermal conductivity.

6.2.3. Data analysis

As discussed previously, a slope method measurement on an anisotropic sample will yield a measured thermal conductivity that is some function of the lateral and transverse thermal conductivity. By depositing the heater/sensor line device along z direction (parallel

to a known crystallographic orientation) on the sample surface as shown in *Figure 6.2*, the measured thermal conductivity could be presented as a function of the thermal conductivity along x and y directions (or along the respective predetermined crystallographic directions).

A function relating the measured thermal conductivity to thermal conductivity in the lateral and transverse directions was determined by Ramu and Bowers to be[23]

$$k_{meas} = k_x \left(\frac{\eta + 1}{2}\right)\left(1 - \frac{(\eta - 1)^2}{4\eta(\eta + 1)}\right) \tag{6.40}$$

where k_{meas} is the measured thermal conductivity using the slope method and $\eta = k_x/k_y$ is the anisotropy ratio. As was shown by Ramu and Bowers[23] for anisotropy ratios $0.6 < \eta < 1.7$ the last term in Equation (6.40) can be neglected and then the thermal conductivities k_x and k_y can be determined with error less than 5%. However, the thermal conductivity anisotropy of β-Ga_2O_3 is not known and such an approximations appears cannot be used.

In order to extract the thermal conductivity of the lateral and transverse solutions from the measured thermal conductivity, the experiment was designed in order to form a solvable system of equations. For each dopant type the measured thermal conductivity was used to extract the lateral and transverse thermal conductivity. A single measurement on a sample would yield an equation that is unable to be solved due to the lateral and transverse thermal conductivities being unknown. For example, for the undoped sample with a (-201) growth face and [010] device orientation, the measurements yield a value that is equivalent to a function with unknowns $k_x = k_{[102]}$ and $k_y = k_{\perp(-201)}$. As seen in *Table 6.1*, there are four measurements that need to be performed for the undoped sample set, yielding four values for the measured thermal conductivity. However, some of the directions that compose the lateral

and transverse heat flow directions are common and therefore a system of four equations with four unknowns have to be solved. The system of equations used for the undoped sample set is:

$$k_{meas,1} = k_{[102]}\left(\frac{\eta_1+1}{2}\right)\left(1-\frac{(\eta_1-1)^2}{4\eta_1(\eta_1+1)}\right), \qquad \eta_1 = \frac{k_{\perp(-201)}}{k_{[102]}} \tag{6.2a}$$

$$k_{meas,2} = k_{[010]}\left(\frac{\eta_2+1}{2}\right)\left(1-\frac{(\eta_2-1)^2}{4\eta_2(\eta_2+1)}\right), \qquad \eta_2 = \frac{k_{\perp(-201)}}{k_{[010]}} \tag{6.2b}$$

$$k_{meas,3} = k_{[102]}\left(\frac{\eta_3+1}{2}\right)\left(1-\frac{(\eta_3-1)^2}{4\eta_3(\eta_3+1)}\right), \qquad \eta_3 = \frac{k_{[010]}}{k_{[102]}} \tag{6.2c}$$

$$k_{meas,4} = k_{\perp[102]}\left(\frac{\eta_4+1}{2}\right)\left(1-\frac{(\eta_4-1)^2}{4\eta_4(\eta_4+1)}\right), \qquad \eta_4 = \frac{k_{[010]}}{k_{\perp[102]}} \tag{6.2d}$$

This same procedure is conducted for the Sn doped sample set, however, a slightly different approach needs to be taken for the Fe-doped sample set as the system of equations contains only two equations with three unknowns due to the lack of sample with (-201) surface. In order to solve the system of equations in the case of Fe doped samples, the values of the thermal anisotropy obtained for UID sample set were used. Such an approximation is justified by the fact that the doping was found to have a negligible effect on the thermal conductivity anisotropy. For example, the values of $\eta_3 = k_{[010]}/k_{[102]}$ for the undoped sample set and the Sn doped sample set were found to be 1.59 and 1.60, respectively. Then for the Fe doped sample set analysis is reduced to solving of two equations with two unknowns.

6.3. Results and discussion

6.3.1. Room temperature thermal conductivity

The extracted values of the room temperature thermal conductivity for undoped, Sn-doped and Fe doped samples can be seen in *Table 6.2*. It can be seen that the highest thermal conductivity for all samples was found in the [010] direction to be $k_{[010]}$ ~ 29 W/mK. This result is consistent with previously reported data by Guo et al.[16] for similar samples from Tamura Corp. and measured by TDTR which relies on unidirectional heat flow. The similarities in the results improve confidence in the thermal conductivity value for the [010] orientation but also proves the viability of the method used in this study.

Table 6.2 *Room temperature (ambient air at 292+/-2 W/mK) thermal conductivity for different orientations and dopants in β-Ga_2O_3.*

Dopant type	$k_{[010]}$	$k_{[102]}$	$k_{\perp[102]}$	$k_{\perp(-201)}$
undoped	29.21	18.39	16.12	17.02
Sn	29.13	18.21	15.67	16.32
Fe	29.06	18.30	15.30	-

Results for the room-temperature thermal conductivity clearly demonstrate the anisotropic nature of β-Ga_2O_3. Thermal conductivity varies nearly 50% from the direction of highest thermal conductivity, [010], to the direction of lowest thermal conductivity, ⊥[102]. Assuming that the acoustic phonons dominate the thermal transport the variation of thermal conductivity will imply a difference in sound velocity and phonon anharmonicity in different crystallographic directions. However, the larger value of thermal conductivity in the [010]

direction has been suggested to be caused by the contribution of optical phonons in addition to the acoustic phonons. Santia et al.[19] found that the optical phonons contribute about 44% to the room temperature thermal conductivity for the [010] direction which is due to the lack of an optical phonon gap in the dispersion for modes propagating along [010]. The largest drawback for β-Ga_2O_3 for high power applications is clearly that the magnitude of the thermal conductivity is relatively low in comparison to other wide bandgap semiconductor materials. In the [010] direction, where the thermal conductivity is the highest, the magnitude is still less than that of α-Al_2O_3 (sapphire) which has a thermal conductivity of ~ 35 W/mK.[24] This property presents serious limitations to a material that is has potential to be used for high-power applications where self-generation of heat is a concern. Comparing to GaN, which competes for many of the same applications as β-Ga_2O_3, the thermal conductivity is an order of magnitude lower at room temperature.[21]

6.3.2. Thermal conductivity at elevated temperatures

The large breakdown voltage of β-Ga_2O_3 allows very efficient operation due to the lower on-state resistance as compared to that of GaN or SiC. However, the β-Ga_2O_3 devices will also suffer from self-generated heat simply due to the large amount of power flowing through the bulk Naturally, this heat in the bulk results in raising the temperature of the device (up to 100ºC), which can significantly affect the material properties and the device performance. Therefore, a detailed knowledge of thermal properties in the entire temperature range of operation is required for proper device design and thermal management.

We have measured the thermal conductivity of all samples in temperature range 295-405 K. The procedure for conducting the elevated temperature measurements consisted of the

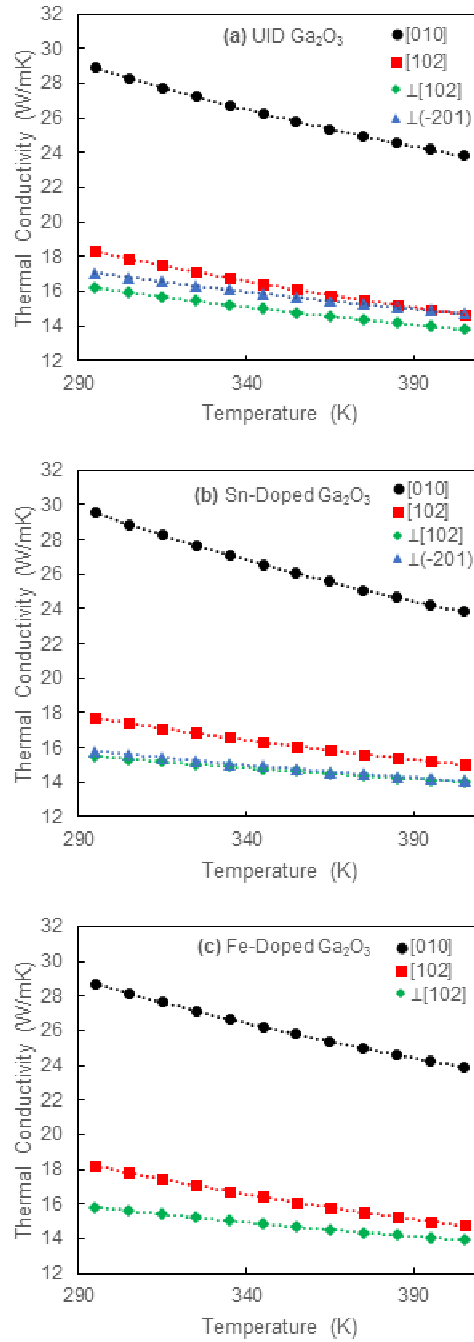

Figure 6.3 *Temperature dependence of the thermal conductivity for different orientations of undoped (a), Sn-doped (b) and Fe-doped (c) Ga_2O_3. Measurement uncertainity is 5%.*

same method used for the room temperature measurements: each sample was measured using the 3ω technique and then the lateral and transverse solutions were solved using a system of equations. At elevated temperatures, all samples were measured at common temperatures and then the same extraction technique was used at each temperature. Once the values of thermal conductivity were extracted for each orientation at each temperature, the thermal conductivity vs temperature was plotted to evaluate orientation dependence or dopant dependence. The temperature dependence of the thermal conductivity for the undoped, Sn and Fe doped samples is shown in *Figure 6.3*. It is seen that the thermal conductivity is reduced with increasing temperature for all orientations and dopants, which is common for semiconductors and insulators. The thermal conductivity decrease is mainly due to the domination of the Umklapp phonon-phonon scattering at elevated temperatures. *Figure 6.3* clearly illustrates how the thermal conductivity in the [010] direction is significantly higher than in the other three measured orientations at all temperatures.

While the comparison of the orientation dependence of the thermal conductivity vs temperature does not change much with each dopant type, it is noticeable that the slope of the temperature dependences does. The temperature dependence of thermal conductivity is often described by a simple power law for semiconductors given by Equation (3.1). The value of α is often used to compare the temperature dependence of thermal conductivity for semiconductors and can be used to evaluate the purity of the crystal. The values of α extracted from the fit for the various orientations and dopants are summarized in *Table 6.3*. A comparative analysis reveals that α is sensitive to both the direction and the doping. Although the data for α seems a bit scattered and it is difficult to draw very solid trends on the effect of

Table 6.3 *Values of the power slope, α, of the thermal conductivity temperature dependence of undoped and doped β-Ga_2O_2 in different crystallographic orientations.*

Dopant type	$\alpha_{[010]}$	$\alpha_{[102]}$	$\alpha_{\perp[102]}$	$\alpha_{\perp(-201)}$
undoped	0.611	0.697	0.506	0.471
Sn	0.679	0.523	0.316	0.366
Fe	0.579	0.665	0.408	-

and orientation, some overall trends can be seen. On average, the value of α is highest for the undoped sample in all orientations.

In pure semiconductors and insulators the Umklapp phonon-phonon scattering is the dominant scattering mechanism at high temperatures (close to the Debye temperature, θ_D) and a temperature dependence of the thermal conductivity with slope α ~ 1 is expected.[25] The Debye temperature of β-Ga_2O_3 is not exactly known. The density functional theory calculations have predicted θ_D = 872 K,[26] while θ_D = 738 K have been estimated from the heat capacity measurements.[16] In both cases, however, the θ_D is determined including all phonon modes (acoustic and optical), although it is not clear how much the optical phonon scattering contributes to the lattice thermal conductivity.[19] In addition, due to the low crystal symmetry of β-Ga_2O_3 there is a reach phonon mode structure with a very complex dispersion[19, 27] and the Umklapp three-phonon scattering which mainly determine the thermal conductivity at high temperatures could be very complicated. Nevertheless, the first principles calculations of the thermal conductivity of a pure β-Ga_2O_3 have predicted a slope of the thermal conductivity temperature dependence (at $T > 200$ K) ranging from 1.13 to 1.39 depending on the crystallographic orientation,[19] close to the expected α ~ 1.

Our experimental data shows that for all samples the slope of the temperature dependence of thermal conductivity (in 295-405 K range) is less than 1 (see *Table 6.3*). (Note that the sample temperature in measurements was far below the suggested value for Debye temperature.) This finding can be explained with a large contribution of both the point-defect-phonon scattering and the free-carrier-phonon scattering. A similar behavior have been observed in Si doped GaN where the slope decreased with increasing doping and/or free electron concentration.[21] A common point defect in β-Ga_2O_3 is the oxygen vacancy which presents at a high concentration independent of the growth method used.[28] Also, even in undoped material there are residual Si (Si_{Ga}) and interstitial (H_i) or substitutional (H_O) hydrogen which lead to *n*-type conductivity.[29] In Fe doped samples additional acceptors are introduced to compensate the residual donors. We have to mentioned that the thermal conductivity measurements by TDTR on similar Sn doped samples from *Tamura Corp.* have revealed a temperature dependence slope α = 1.12-1.28 for a temperature range of 200-495 K.[16] The reason for the discrepancy with our results is not is not clear yet, but we should mentioned that the TDTR technique relies on unidirectional heat flow.

From *Table 6.3* it is also observed that the temperature dependence of thermal conductivity depends on the heat flow direction. On average, the value of α is higher in the [010] direction where the highest room temperature thermal conductivity is obtained. The dependence of α on the heat flow direction suggests that the material properties in each direction are changing to different extend leading to a different temperature dependence.

6.3.3. Effect of doping

From *Table 6.2* it is clear that the thermal conductivity does not change significantly with the doping. The highest thermal conductivities are found in the undoped samples for all directions which is expected due to the relative purity of the material. The intentional doping reduces the thermal conductivity due to the increased phonon-point-defect scattering. However, the reduction due to the Sn and Fe impurities can be seen to be very small, less than 5% for all orientations measured, which is the same as the 5% measurement uncertainty at elevated temperatures. As can be seen by the results in *Table 6.2*, the thermal conductivity for the Sn-doped samples is slightly higher than that of the Fe-doped samples. This small increase in the thermal conductivity of the Sn-doped samples may be due to an electronic contribution to the thermal conductivity. However, it is likely that any contribution of electrons to thermal conductivity will be small for moderate Sn doping levels at this temperature range. The effect of impurities on the thermal conductivity for each orientation are shown in *Figure 6.4*. Our results are consistent with previously reported trend for β-Ga_2O_3 with different dopant reported by Handwerg et al.[17] In particular, the Mg doped β-Ga_2O_3 showed similar thermal conductivity as undoped samples within the measurement uncertainty.

The intentional doping can be seen to further reduce the value of α, with the Sn doped and Fe doped samples having slightly lower values on average compared to the undoped samples. The Sn doping increases the contribution of both the phonon-point-defect scattering and the phonon-free-electron scattering and then decreases the thermal conductivity. The contribution of phonon-free-electron scattering in the Sn doped samples on average lowers

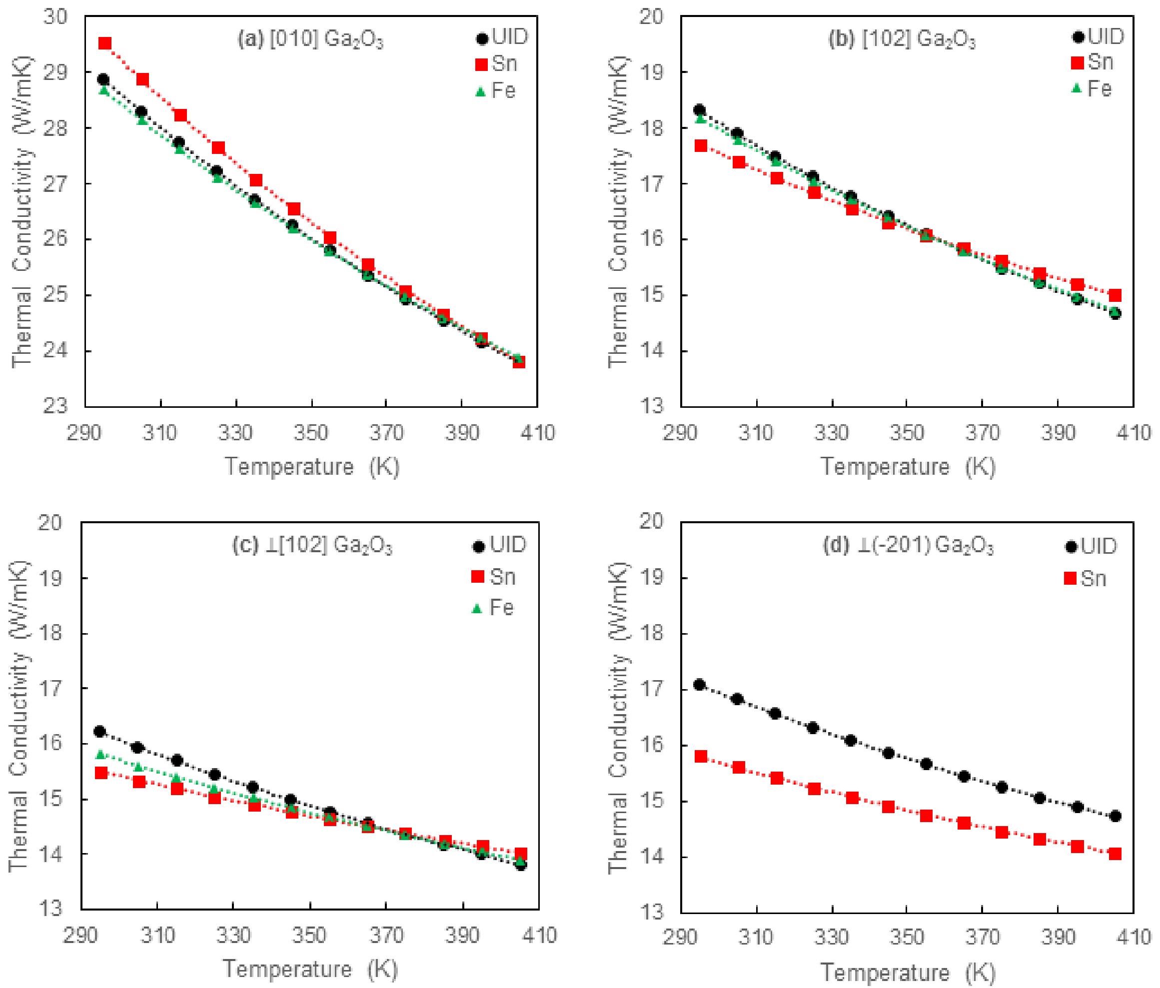

Figure 6.4 *Effect of Sn and Fe doping on the thermal conductivity temperature dependence for the [010] (a), [102] (b), ⊥[102] (c) and ⊥(-201) (d) directions. (Note the different scales of the y-axis.) Measurement uncertainty of 5%.*

the value of α compared to the Fe doped samples, since the Fe doped set only have contributions from phonon-point-defect scattering. Trends in the temperature dependence of thermal conductivity are most easily illustrated by comparing the effect of dopants on thermal conductivity vs. temperature for each direction, as seen in *Figure 6.4*. For each

direction, it can be seen that the Sn and Fe doping changes the temperature dependence of thermal conductivity. For every orientation other than the ⊥(-201) direction, the dopants slightly affect the value of α. This property of β-Ga_2O_3 is overall beneficial for the design of thermal management – having the thermal conductivity not decrease significantly with temperature for all dopants means that layered structures will have similar thermal management properties for *n*-type and semi-insulating layers over the entire range of operation.

6.4. Conclusions

The thermal conductivity of β-Ga_2O_3 bulk crystals was measured using the 3ω technique in order to explore the effects of anisotropy and intentional Sn and Fe doping. A unique approach to extracting the thermal conductivity of the lateral and transverse heat flow directions was used in order to solve the issue of the two-dimensional heat flow of the 3ω method in the crystal with anisotropic properties. Results for the thermal conductivity at room temperature clearly illustrated the highly anisotropic behavior of β-Ga_2O_3, with the difference between the directions of highest and lowest thermal conductivity being ~50%. The room temperature thermal conductivity was found to be highest (~ 29 W/mK) in the [010] direction for all dopants. The Sn and Fe doping does not significantly decrease the thermal conductivity for each orientation. The minor reduction in the thermal conductivity with dopants is a significant property, as the modulation of electrical properties does not significantly vary the thermal properties. In order to evaluate the performance of β-Ga_2O_3 at typical operation temperatures, measurements of the thermal conductivity were taken in the temperature range of 295-405 K. With increasing temperature the thermal conductivity was

found to decrease mainly due to the increased phonon-phonon scattering. A simple power law was used to describe the reduction of thermal conductivity and the slope was found to be in the range of 0.4-0.7 for all the dopants and orientations. The value of the slope was highest for the undoped samples, indicative of their relative purity compared to the Sn and Fe doped samples. The reduction of the slope in doped samples was attributed to the increased contribution of the phonon-point-defect scattering. Overall, the temperature dependence of the thermal conductivity was not found to significantly change with doping, which is a beneficial property for the design of devices.

The thermal conductivity of β-Ga_2O_3 as measured here (and in previous reports) is significantly lower than that in other wide bandgap semiconductors, e. g. SiC and GaN, and it is likely to be the limiting factor for the use of this material in high power applications. However, it is still not clear if this low thermal conductivity is due to the fundamental limitations or due to the quality of the material available so far. Therefore, more detailed studies of the thermal properties of β-Ga_2O_3 are highly desirable.

References

1 S. I. Stepanov, V. I. Nikolaev, V. E. Bougrov, and A. E. Romanov, Gallium Oxide: Properties and Applications - A Review, Rev. Adv. Mater. Sci 44, 63 (2016).

2 M. Higashiwaki, K. Sasaki, A. Kuramata, T. Masui, and S. Yamakoshi, Gallium oxide (Ga2O3) metal-semiconductor field-effect transistors on single-crystal β-Ga2O3 (010) substrates, Appl. Phys. Lett. 100, 13504 (2012).

3 Z. Galazka, K. Irmscher, R. Uecker, B. Rainier, M. Pietsch, A. Kwasniewski, M. Nauman, T. Schulz, R. Schewski, D. Klimm, and M. Bickermann, On the bulk β-Ga2O3 single crystals grown by the Czochralski method, J. Cryst. Growth 404, 184 (2014).

4 K. Hoshikawa, E. Ohba, T. Kobayashi, J. Yanagisawa, C. Miyagawa, and Y. Nakamura, Growth of β-Ga2O3 single crystals using vertical Bridgman method in ambient air, Journal of Crystal Growth 447, 36 (2016).

5 E. G. Villora, K. Shimamura, Y. Yoshikawa, A. Kazuo, and N. Ichinose, Large-size β-Ga2O3 single crystals and wafers, Journal of Crystal Growth 270, 420 (2004).

6 A. Kuramata, K. Koshi, S. Watanabe, Y. Yamaoka, T. Masui, and S. Yamakoshi, High-quality β-Ga2O3 single crystals grown by edge-defined film-fed growth, Japanese Journal of Applied Physics 55, 1202 (2016).

7 K. Sasaki, M. Higashiwaki, A. Kuramata, T. Masui, and S. Yamakoshi, Ga2O3 Schottky Barrier Diodes Fabricated by Using Single-Crystal B-Ga2O3 (010) Substrates, Led 34, 493 (2013).

8 T. Oishi, Y. Koga, K. Harada, and M. Kasu, High-mobility β-Ga2O3 (-201) single crystals grown by edge-defined film-fed growth method and their Schottky barrier diodes with Ni contact, Applied Physics Express 8, 031101 (2015).

9 M. Higashiwaki, K. Konishi, K. Sasaki, K. Goto, K. Nomura, Q. T. Thieu, R. Togashi, H. Murakami, Y. Kumagai, B. Monemar, A. Koukitu, A. Kuramata, and S. Yamakoshi, Temperature-dependent capacitance–voltage and current–voltage characteristics of Pt/Ga2O3 (001) Schottky barrier diodes fabricated on n —Ga2O3 drift layers grown by halide vapor phase epitaxy, Applied Physics Letters 108, 133503 (2016).

10 M. Higashiwaki, K. Sasaki, T. Kamimura, M. Hoi Wong, D. Krishnamurthy, A. Kuramata, T. Masui, and S. Yamakoshi, Depletion-mode Ga2O3 metal-oxide-semiconductor field-effect transistors on β-Ga2O3 (010) substrates and temperature dependence of their device characteristics, Appl. Phys. Lett. 103, 123511 (2013).

11 A. J. Green, K. D. Chabak, E. R. Heller, R. C. Fitch, M. Baldini, A. Fiedler, K. Irmscher, G. Wagner, Z. Galazka, S. E. Tetlak, A. Crespo, K. Leedy, and G. H. Jessen, 3.8-MV/cm Breakdown Strength of MOVPE-Grown Sn-Doped \beta -Ga2O3 MOSFETs, Led 37, 902 (2016).

12 K. D. Chabak, N. Moser, A. J. Green, D. E. Walker, S. E. Tetlak, E. Heller, A. Crespo, R. Fitch, J. P. McCandless, K. Leedy, M. Baldini, G. Wagner, Z. Galazka, X. Li, and G. Jessen, Enhancement-mode Ga2O3 wrap-gate fin field-effect transistors on native (100) β-Ga2O3 substrate with high breakdown voltage, Appl. Phys. Lett. 109, 213501 (2016).

13 M. H. Wong, K. Sasaki, A. Kuramata, S. Yamakoshi, and M. Higashiwaki, Field-Plated Ga2O3 MOSFETs With a Breakdown Voltage of Over 750 V, IEEE Electron Device Lett. 37, 212 (2016).

14 C. Mion, J. F. Muth, E. A. Preble, and D. Hanser, Accurate dependence of gallium nitride thermal conductivity on dislocation density, Applied Physics Letters 89, 92123 (2006).

15 E. G. Víllora, K. Shimamura, Y. Yoshikawa, T. Ujiie, and K. Aoki, Electrical conductivity and carrier concentration control in β-Ga2O3 by Si doping, Appl. Phys. Lett. 92, 202120 (2008).

16 Z. Guo, A. Verma, X. Wu, F. Sun, A. Hickman, T. Masui, A. Kuramata, M. Higashiwaki, D. Jena, and T. Luo, Anisotropic thermal conductivity in single crystal β-gallium oxide, Appl. Phys. Lett. 106, 111909 (2015).

17 M. Handwerg, R. Mitdank, Z. Galazka, and S. F. Fischer, Temperature-dependent thermal conductivity in Mg-doped and undoped \beta-\mathrm{Ga_2O_3} bulk-crystals, (2014).

18 M. Handwerg, R. Mitdank, Z. Galazka, and S. F. Fischer, Temperature-dependent thermal conductivity and diffusivity of a Mg-doped insulating \beta-\mathrm{Ga_2O_3} single crystal along [100], [010] and [001], (2015).

19 M. D. Santia, N. Tandon, and J. D. Albrecht, Anisotropic intrinsic lattice thermal conductivity in B-Ga2O3 from first principles, Appl. Phys. Lett. 107, 1 (2015).

20 D. G. Cahill, Thermal conductivity measurement from 30 to 750 K: the 3ω method, Rev. Sci. Inst. 61, 802 (1990).

21 M. Slomski, L. Liu, J. F. Muth, and T. Paskova, Growth Technology for GaN, AlN Bulk Substrates and Templates, in Handbook of GaN Semiconductor Materials and Devices, (in press 2017).

22 T. Borca-Tasciuc, A. R. Kumar, and G. Chen, Data reduction in 3ω method for thin-film thermal conductivity determination, Review of Scientific Instruments 72, 2139 (2001).

23 A. T. Ramu, and J. E. Bowers, Analysis of the "3-Omega" method for substrates and thick films of anisotropic thermal conductivity, J. Appl. Phys. 112, 43516 (2012).

24 A. Sarua, Hangfeng Ji, K. P. Hilton, D. J. Wallis, M. J. Uren, T. Martin, and M. Kuball, Thermal Boundary Resistance Between GaN and Substrate in AlGaN/GaN Electronic Devices, Ted 54, 3152 (2007).

25 J. M. Ziman, Electrons and Phonons, (Oxford University Press, Oxford, 2001).

26 H. He, M. A. Blanco, and R. Pandey, Electronic and thermodynamic properties of B-Ga2O3, Appl. Phys. Lett. 88, 1 (2006).

27 B. Liu, M. Gu, and X. Liu, Lattice dynamical, dielectric, and thermodynamic properties of β-Ga2O3 from first principles, Applied Physics Letters 91, 172102 (2007).

28 L. Dong, R. Jia, B. Xin, B. Peng, and Y. Zhang, Effects of oxygen vacancies on the structural and optical properties of β-Ga2O3, Scientific Reports 7, 40160 (2017).

29 J. B. Varley, J. R. Weber, A. Janotti, and Van de Walle, C. G, Oxygen vacancies and donor impurities in β-Ga2O3, Applied Physics Letters 97, 142106 (2010).